Modeling, Simulating and Quantification of Optical Images of Ultrasound Contrast Bubbles

By

Habtamu Abraham

In partial fulfillment of the requirements for the degree of master science in Biomedical Engineering

Center of Biomedical Engineering

Addis Ababa Institute of Technology

Addis Ababa University

Advisor: Dawit Assefa Haile (PhD)

Co-Advisor: Michiel Postema (PhD)

Addis Ababa, Ethiopia, July 7, 2017

Declaration

I, the undersigned, declare that this thesis and the work presented in it are my own and has been generated by me as the result of my own original research.
I confirm that:

- This work was done wholly or mainly while in candidature for a research degree at this University;
- Where any part of this thesis has previously been submitted for a degree or any other qualification at this University or any other institution, this has been clearly stated;
- Where I have quoted from the work of others, the source is always given. With the exception of such quotations, this thesis is entirely my own work;
- I have acknowledged all main sources of help;
- This work or any part of this work has not been published before submission;

Name: _____

Signature: _____

Date: _____

This MSc. thesis has been submitted for examination with my approval as an advisor.

_____

Dawit Assefa Haile (PhD.)

Certificate of examination

Addis Ababa University

School of Graduate Studies

This is to certify that the thesis prepared by Habtamu Abraham entitled: *Effective Measurement of Optical Images of Ultrasound Contrast Bubbles using Image Processing* submitted in partial fulfillment of the requirements for the degree of Master of Science in Biomedical Engineering (Bioinstrumentation and Imaging) complies with the regulations of the University and meets the accepted standards with respect to originality and quality.

Signed by the examining committee

Examiner:_____ Signature:_____ Date:_____

Examiner:_____ Signature:_____ Date:_____

Examiner:_____ Signature:_____ Date:_____

Examiner:_____ Signature:_____ Date:_____

_____

Chief of department or Graduate program coordinator

Abstract

Effective Measurement of Optical Images of Ultrasound Contrast Bubbles using image Processing

Habtamu Abraham*, *Addis Ababa University, 2017

Microbubble based ultrasound contrast agents are being used in clinical settings to enhance backscattered ultrasound signal from blood pool during perfusion and blood flow measurements. Often individual bubbles are characterized optically by recording their vibrations with a fast framing camera and direct quantitative information on their dynamic behavior can be derived. Nonetheless, when a three-dimensional object, stack of infinitely thin two-dimensional layers, is imaged through a microscope, the image formed onto the charge coupled device element consists of contributions from all layers. If a bubble is larger than the depth of focus, the part of the bubble above the focal plane influences the image formation and therefore the bubble size measured. Thus, this thesis presents a methodology to compute two-dimensional image formation from three-dimensional objects, hollow spheres and find under which circumstances the optical image formation leads to a significant deviation in measurement of the actual size. Two-dimension image formations of the three-dimensional object was computed by convolving the slices of an artificial object, hollow spheres with the respective weighted point spread function and summing all convolved slices. Finally, image processing was applied the optical image formed to quantify the object size and a systematic error was observed for objects in focus with radius $\leq 1.65\mu$m. Also it was concluded that even though a three-dimensional object is in focus, there is discrepancy of up to 0.66% in size measurement. In addition, size measurement of an object for the same shift above the focus and below the focus could differ by up to 3.6%. Moreover, defocusing up to 90% could result up to 64.7 mean percentage error. The results reveal that defocusing above 25% severely deviates size measurements. This thesis hopes to offer a standard for quantification of optical images of three-dimensional objects, and in the future actual size of an object could be measured from its defocused optical images.

Acknowledgment

First and foremost, praises and thanks to the God, the Almighty to whom I owe my very existence, for the strengths and His blessing in completing this thesis.

I am greatly thankful to my supervisor Dawit Assefa (PhD.), for his unreserved support, professional guidance, constant encouragement from the commencement of the study and moral support in many ways during the research period.

I am also greatly indebted to Michiel Postema (PhD.), of Institute of Fundamental Technological Research, Polish Academy of Sciences, for his valuable ideas, recommendations and directions to accomplish the study and for providing raw data of bubble microscope images.

I am also grateful to Masreshaw Demelash (PhD.), post graduate coordinator, for all his encouragement and helpful comments on my document.

I would like to express my sincere thanks to Birhanu Assefa (MSc.), for the useful scientific discussions, and friendly conversations.

Finally I owe my deepest gratitude to my parents, for their love, support, and understanding.

Table of Contents

List of Figures

List of Tables

List of Abbreviations

ADC	**A**nalog-to-**D**igital **C**onversion
A-mode	**A**mplitude-mode
B-mode	**B**rightness-mode
CAP	**C**ontrast **A**gent **P**articles
CCD	**C**harge-**C**oupled **D**evice
CEUS	**C**ontrast **E**nhanced **U**ltrasound **S**ound
DOF	**D**epth **O**f **F**ocus
EM	**E**lectro **M**agnetic
FDA	**F**ood and **D**rug **A**dministration
4D	**F**our**D**imensional
GE	**G**eneral **E**lectric
IV	**I**ntra**V**ascular
LSI	**L**inear **S**hift-**I**nvariant
MI	**M**echanical **I**ndex
M-mode	**M**otion-mode
NA	**N**umerical **A**perture
1D	**O**ne-**D**imensional
PSF	**P**oint **S**pread **F**unction
RGB	**R**ed **G**reen-**B**lue
2D	**T**wo-**D**imensional
3D	**T**hree-**D**imensional
TGC	**T**ime **G**ain **C**ompensation
US	**U**ltra **S**ound

List of Symbols

Symbol	Description	Unit
Chapter 2		
u	speed of sound	$\mathrm{m\,s^{-1}}$
f_i	incident sound frequency	$\mathrm{s^{-1}}$
f_r	reflected sound frequency	$\mathrm{s^{-1}}$
ν	frequency	$\mathrm{s^{-1}}$
θ	lateral angle	
Chapter 3		
MI	mechanical index	
P_N	peak negative pressure	$\mathrm{kg\,m^{-1}\,s^{-2}}$
m	mass	kg
$\dot{x}$	first time derivative of x	$\mathrm{m\,s^{-1}}$
$\ddot{x}$	second time derivative of x	$\mathrm{m\,s^{-2}}$
s	stiffness	$\mathrm{kg\,s^{-2}}$
P_0	ambient pressure	$\mathrm{kg\,m^{-1}\,s^{-2}}$
R_0	quasi-equilibrium radius	$\mathrm{kg\,s^{-2}}$
P_v	vapour pressure	$\mathrm{kg\,m^{-1}\,s^{-2}}$
Chapter 4		
f	geometric focal length	m
d_f	distance of object	m
d_i	distance of image	m
n	refractive index	
D	aperture diameter	m
NA	numerical aperture	
NA_{obj}	numerical aperture of objective	
NA_{cond}	numerical aperture of condenser	
α	acceptance angle	
Δz	depth of focus	m
E	electric field	$\mathrm{kg\,m\,s^{-3}\,A^{-1}}$
$\vec{E}$	electric field vector	$\mathrm{kg\,m\,s^{-3}\,A^{-1}}$
B	magnetic field	$\mathrm{kg\,s^{-2}\,A^{-1}}$
$\vec{B}$	magnetic field vector	$\mathrm{kg\,s^{-2}\,A^{-1}}$
μ_0	permeability of free space	$\mathrm{m\,kg\,s^{-2}\,A^{-2}}$
ε_0	permittivity of free space	$\mathrm{m^{-3}\,kg^{-1}\,s^{4}\,A^{2}}$
ψ	wavefunction	

Symbol	Description	Unit
c	speed of Light	$\mathrm{m\,s^{-1}}$
c'	speed of light through a medium	$\mathrm{m\,s^{-1}}$
Q	location of point light source	m
P	location of diffraction point	m
U	diffracted field	
r_0	radius of spherical wave-front	m
Σ	aperture plane	
ξ	ξ-coordinate	
η	η-coordinate	
ρ	radial distance from center of aperture plane	m
ϕ	ϕ-coordinate	
Φ	Φ-coordinate	
J_1	first-order Bessel function	
I	irradiance	$\mathrm{kg\,s^{-3}}$
r	radial distance from center of image plane	m
Chapter 5		
o	object function	
i	image function	
PSF	point spread/filter function	
h	filter function	
$f(x,y)$	input function of $x,\ y$	
$g(x,y)$	output function of $x,\ y$	
T	thresholding value	
$A_{N\times M}$	$N \times M$ on pixel area	
Chapter 6		
w	weighting function	
P_w	pixel width	m
P_h	pixel height	m
P_a	pixel area	$\mathrm{m^2}$
A_b	area of bubble	$\mathrm{m^2}$
r_b	radius of bubble	m

CHAPTER 1

Introduction

1.1 Background

Medical ultrasound imaging is based on backscattered echoes of sound from a body with different tissue structures [1]. Clinically detecting blood flow and perfusion are of great interest but, because blood reflects ultrasound poorly it is technically challenging. [2]. Thus, ultrasound contrast agent is introduced in the blood to increase the scattering properties from the blood pool enabling imaging of capillary networks [3, 4]. It is a liquid containing small gas-filled encapsulated microbubbles [5]. These microbubbles scatter ultrasound efficiently than a solid particle of the same size, at up to 9 orders of magnitude [6]. Consequently, they enhance contrast-to-tissue ratio.

These days, many researchers focus much of their attention in developing sophisticated ultrasound contrast imaging techniques exploiting bubble-specific signatures [7]. Hence, the studies are fixated on quantitative description of the behavior of microbubbles in an ultrasound field. Several studies have been performed in the past on bubble populations with known size distributions to determine the shell properties of the bubbles [7–9]. However, studying bubble populations does not consider the effect of bubble-bubble interactions and it only measures the average response of all bubbles [7]. To overcome these limitations, the response of individual microbubble is studied, instead of bulk response of a majority of bubbles [7].

Individual response of a microbubble is characterized using two methods, acoustical and optical, or combination of the two [6, 10]. Several in vitro studies have demonstrated that single bubble responses can be measured acoustically [11–13]. Although, it is possible to characterize individual bubbles acoustically it is experimentally challenging [7,14]. In addition, it does not provide direct measurement of the microbubbles size [7]. On the other hand, optical methods have been proposed [15–17] to overcome the difficulties associated with

acoustical characterization. Optical characterization is done by recording movies of bubble response to ultrasound field using high frame rate camera operating up to 25 million frames per second [18]. From these optical images the dimension of bubbles is directly measured [14]. It enables in-depth investigation on individual bubble response to ultrasound excitation and direct measurement of the bubble radius, which, unlike the acoustical response, is not subject to distortion and in principle does not require difficult calibration [2, 14].

Though, optical visualization is costly and limited by resolving power of the optical system [7]. Over the past years, numerous authors have shown that high-speed optical recordings provide quantitative information on the dynamic behavior of single microbubble in an ultrasound field [2, 14, 19]. The studies were performed by recording two-dimensional (2D) bubble pictures using a high-speed imaging system and deriving radius-time curves from 2D bubble pictures [2, 5, 14]. In an experiment done on a previous study [2], recording movies of bubbles with a high frame rate camera operating at 3 MHz and comparing real images size to simulations showed that there is no systematic error in measurement for microbubbles with diameters greater than 0.8μm [2]. However, the influence of the contribution of the bubble parts above and below the focal plane were discarded.

The aim of this thesis work was to investigate whether a systematic error occurs when measuring microbubbles in focus, when taking into account all layers contributing to the image. With this intention, the image formation of microbubbles were computed with an ideal three-dimensional point spread function (PSF) and compared to photographs of microbubbles. The artificial images were subjected to segmentation techniques for objectively comparing original microbubble sizes with measured sizes.

1.2 Statement of the problem

A 3D object under a microscope can be considered as a stack of thin 2D layers [20]. When 3D objects are observed through a microscope, the image formed consists of contributions from all of these layers. A bubble is considered in focus if the middle layer of the sphere is in the focal plane. If a bubble is larger than the depth of focus, the part of the bubble above the focal plane influences the image formation and therefore the bubble size measures. Consequently, images from an axial shift above the focal plane are not identical to the images from the same shift below the focal plane. If a bubble is of a size in the order of the wavelengths of the light

used, the system resolution and the segmentation method influence the bubble size measured.

In a previous study, comparing real images to simulations of a 2D PSF on circular objects, no systematic error was found when measuring the size of microbubbles with diameters of 0.35μm and greater [2]. However, the influence of the contribution of the bubble parts above and below the focal plane were not considered. Hence, the aim of this study is to thoroughly investigate whether a systematic error occurs when measuring microbubbles in focus after taking into account all layers contributing to the image and to analyze the effect of defocusing in measuring the bubble size.

1.3 Objective of the thesis

1.3.1 General objective

The main objective of this thesis is to investigate and find out whether there is a systematic error in measuring the size of 3D objects of size greater than the depth of focus of the optical photography system.

1.3.2 Specific objectives

The specific objectives of this thesis are to:

- Compute 2D image formation from 3D objects, hollow spheres, using 3D PSF;
- Quantify the size of 2D imaged formed from 3D objects using image processing;
- Find under which circumstances the image formation leads to a significant deviation in measurement of the actual bubble size.

1.4 Significance of the thesis

Application of ultrasound contrast agent is now a common practice in medical diagnostic. The findings of this study could lead to a better optical characterization and understanding of the behavior of a single contrast agent microbubble in an ultrasound field. Hence, understanding the acoustic properties of individual microbubble formulations is important for optimizing the ultrasound imaging parameters for improved sensitivity, image contrast, resolution in both large vessels and microvasculature studies.

Moreover, new generations of ultrasound contrast agents are under investigation to further

improve the scattering from blood and to ameliorate its detection in the presence of surrounding tissue. Therefore, a better understanding of bubbles could help in developing sophisticated perfusion and blood flow detection techniques. Furthermore, the application of ultrasound contrast agents is evolving towards therapeutics. Thus, in the long run this research would help in better understanding of bubbles in drug delivery system.

1.5 Scope and delimitations of the thesis

The thesis only considers and models 3D objects (microbubbles) as hollow spheres. Moreover, the parameters chosen to describe the optical system were unrealistically superb compared to those of the actual experimental setup. The number of 2D slices taken from the 3D objects to compute the image formed from the 3D objects is limited by computational (memory and speed) constraints. The quantification of artificial objects (spheres) is limited by the image resolution taken. The quantification of actual contrast agent microbubbles is beyond the scope of the thesis.

1.6 Organization of the thesis

The rest of the thesis is organized into the following chapters. In Chapter 2, the basic concepts and physic of medical ultrasound imaging are discussed. Chapter 3 illustrates the relevant literatures about contrast agent microbubbles.

Chapter 4 provides a description on fundamentals of optical microscopy, components of a microscope, technical terms in microscopy and wave nature of light. Chapter 5 discusses the concepts of optical image processing, optical image levels, image formation in microscopy, image segmentation, quantification of objects and relevant researches in the area.

Chapter 6 explains the methodologies and procedures proposed in this thesis for effective measurement of ultrasound contrast microbubbles based on image processing while Chapter 7 presents selected results accompanied by useful discussions. Supplementary results are also included in Appendices A to E.

Chapter 8 offers a summary and discussion of the research findings in this thesis, their implications as well as recommendations for possible future research.

CHAPTER 2

Ultrasound Imaging

2.1 Introduction

Medical ultrasound (US) imaging, also known as echography, is one of the most frequently used front-line clinical imaging modalities [1]. It is used to visualize different body parts and their functions by means of blood and myocardial velocities [21]. Although it has been used in clinical practice for more than half a century [21], it is still advancing in technology, to the extent that it has a well-established place in clinical practices and currently accounts for about one in four of all imaging procedures worldwide [22]. In addition, it is characterized by its safety, affordability, accessibility, real-time image displays and portable imaging modality [1].

Historically, the basis of US imaging can be traced back to the time of Lazzaro Spallanzani, an Italian physiologist and biologist. In 1790, he discovered that bats navigate in the dark using their hearing rather than sight, through the reflection of high frequency sounds (echo location) [23] as shown in Fig. 2.1. Following this discovery, several scientists and physicist were inspired to study the nature of sound.

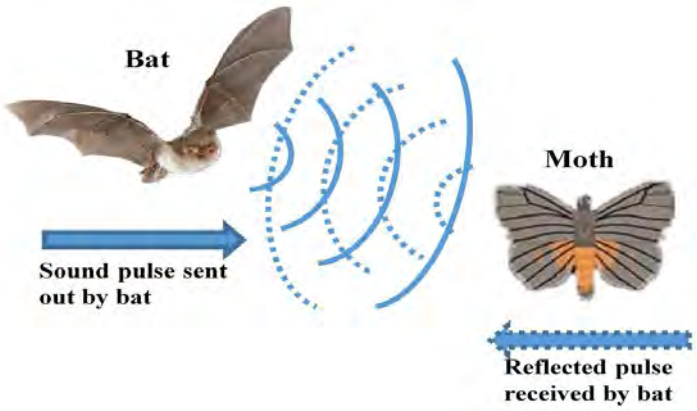

Figure 2.1: *Echo location by animals.*

However, it was After World War II, the potential of US as a diagnostic imaging modality was realized [23]. In the early 1950s, John Wild and John Reid in Minnesota developed a prototype

brightness mode (B-mode) ultrasonic imaging instrument [24]. In 1955, the earliest ultrasonic Doppler devices for monitoring tissue motion and blood where developed by two Japanese investigators, Shigeo Satomura and Yasuhara Nimura [24].

Despite that diagnostic US has been in existence for more than 50 years, yet it continues to evolve at a surprisingly rapid rate [3]. Technical advances are still being made. The introduction of contrast agents for better delineation of the anatomy, measurement of tissue perfusion, precise drug delivery mechanisms, and determination of elastic properties of the tissues are examples of current researches in the area [24, 25]. Today, US is the second most utilized diagnostic imaging modality in medicine, second only to conventional x-ray, and is a critically important diagnostic tool of any medical facility [24].

2.2 Principle of Ultrasound imaging

Ultrasound imaging is an imaging technique, which uses a frequency beyond human hearing (i.e $>$ 20KHz). However, the typical frequency range used is 1 - 50MHz [26]. In US imaging, a short pulse of mechanical energy is delivered to the tissues and the pulse travels at the speed of sound, and with changes in the tissue acoustic properties, a fraction of the pulse is reflected as an echo and returns to the source. Collection of the echoes over time and recording of the echo amplitudes provide information about the tissues along the path of travel. Repeating the process hundreds of times with a small incremental change in the direction of the pulse interrogates a volume, from which a gray-scale tomographic image (see Fig. 2.2b) can be synthesized [25].

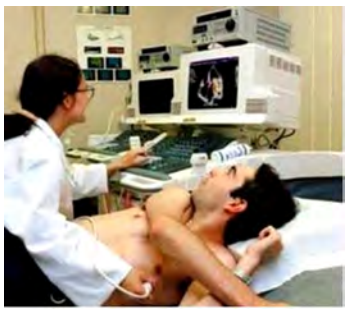

(a)

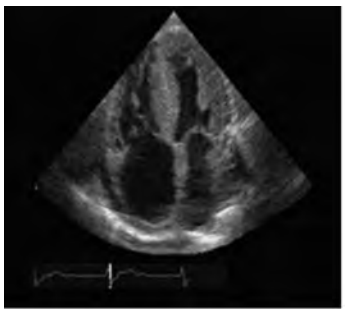

(b)

Figure 2.2: *(a) Echocardiography being performed in a hospital, and (b) A typical echocardiogram [27].*

2.3 Ultrasound imaging modes

Ultrasound images are created using a pulse-echo mode format of US production and detection. Instead of applying a continuous electrical signal to the crystal, pulses are used to obtain spatial

information. Each pulse is directionally transmitted into the patient and experiences partial reflections from tissue interfaces that create echoes, which return to the transducer. US images are acquired mainly in three echo modes (amplitude-mode, brightness-mode and motion-mode) [21]. A typical modern ultrasound scanner is shown in Fig. 2.3.

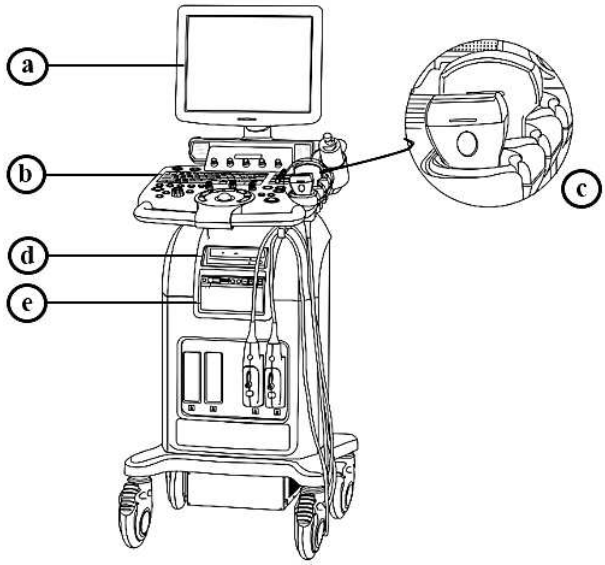

Figure 2.3: *Modern ultrasound scanner with a monitor (a), manual controls (b), several probes (c), DVD-RW drive (d), and a printer (e) [29].*

2.3.1 A-mode

Amplitude (A-mode) is the simplest mode of one-dimensional (1D) data acquisition which is based on the pulse–echo principle [21, 25]. It displays reflected (both specular and scattered) ultrasound waves as a function of time (see Fig. 2.4).

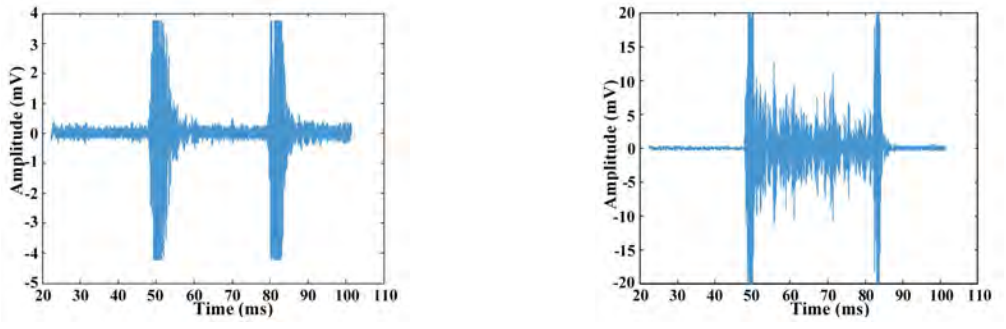

(a) ***(b)*** .

Figure 2.4: *Reflected signal as a function of time (a) For a homogeneous object in water. Obviously, a large reflection occurs at the interfaces between the two matters. (b) For an inhomogeneous object in water. The reflections show an exponential decay [21].*

2.3.2 B-mode

Brightness (B-mode) imaging is the electronic conversion of the A-mode and A-line information into brightness-modulated dots along the A-line trajectory. In general, the

brightness of the dot is proportional to the echo signal amplitude. A two-dimensional (2D) image data (Fig. 2.5) is obtained by translating the transducer between two A-mode acquisitions [21, 30].

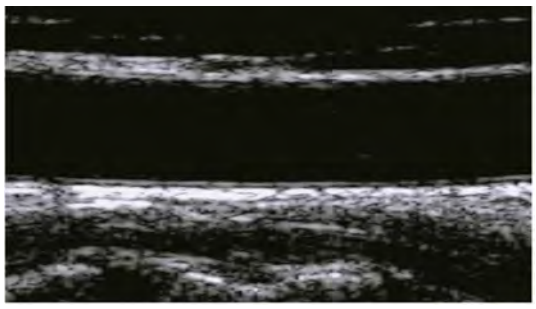

Figure 2.5: *Ultrasound B-Mode image of carotid artery on a healthy volunteer. Flowing blood appears as a solid black area inside of the vessel walls [26].*

2.3.3 M-mode

Motion (M-mode) imaging is a technique that uses B-mode information to display the echoes from a moving organ from a fixed transducer position and beam direction on the patient [21]. The echo data from a single ultrasound beam passing through moving anatomy are acquired and displayed as a function of time. It yields a 2D image with depth and line number as the dimensions (see Fig. 2.6).

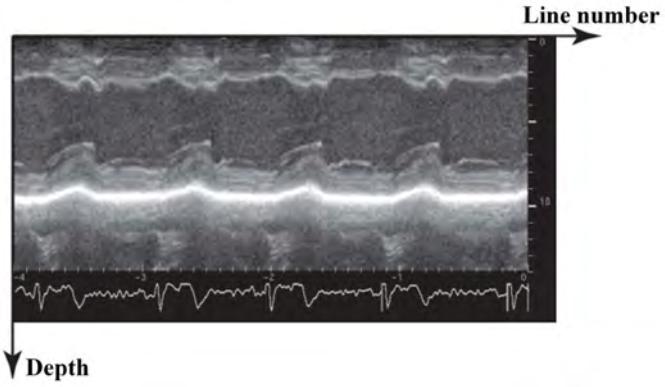

Figure 2.6: *M-mode image of the heart wall for assessment of cardiac wall motion during contraction. The black region is blood, the bright reflection is the pericardium (i.e., a membrane around the heart), and the gray region in between is the heart muscle itself [22].*

2.4 Doppler ultrasound imaging

Doppler ultrasound imaging is a technique which is used to visualize and measurement of moving reflector object, such as blood cells flowing in the body. It is based on the shift of frequency in an ultrasound wave caused by a moving reflector, such as blood cells in the vasculature (Fig. 2.7) [25]. Hence, Data acquisition and reconstruction are different from gray scale imaging [21]. Even when blood cannot be seen directly, its movement can be detected.

(a) ***(b)*** .

Figure 2.7: *Doppler ultrasound exploits changes in frequency from interaction with moving objects [21]. (a) Blood moving towards transducer produces higher frequency echoes, and (b) Blood moving away from transducer produces lower frequency echoes.*

The Doppler Effect

The Doppler principle states that the frequency of the reflected ultrasound is altered by a moving target in a way that if a sound source moves toward the observer, the reflect sound frequency increases, conversely if the source moves away from the observer (see Fig. 2.8), the reflected sound frequency decreases and the generalized Doppler shift is expressed as [25]:

$$f_d = f_r - f_i = \frac{2 f_i v \cos(\theta)}{u}, \tag{2.1}$$

where f_r, and f_i, are reflected sound frequency and incident sound frequency respectively. Thus, the Doppler shift is proportional to the velocity of the blood cells.

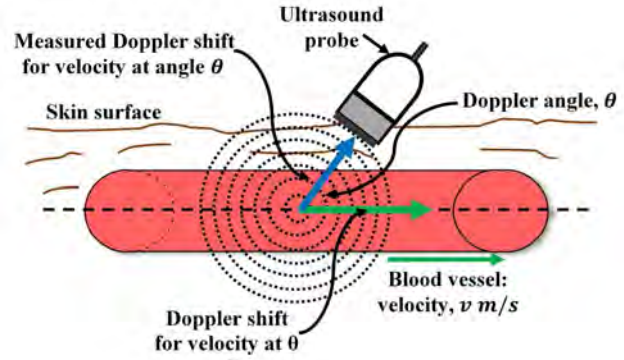

Figure 2.8: *Geometry of Doppler ultrasound data acquisition [21].*

Calculation of the blood velocity is straightforward by rearranging the Doppler equation:

$$v = \frac{f_d u}{2 f_i \cos(\theta)} \tag{2.2}$$

Thus, the measured Doppler shift at a Doppler angle θ is adjusted by $1/\cos(\theta)$ in order to achieve accurate velocity estimates. At a 60-degree Doppler angle, the measured Doppler frequency is half of the actual Doppler frequency, and at 90 degrees, the measured frequency is zero. The preferred Doppler angle ranges from 30 to 60 degrees. At too large an angle (greater than 60 degrees), the apparent Doppler shift is small, and minor errors in angle accuracy can result in large errors [25].

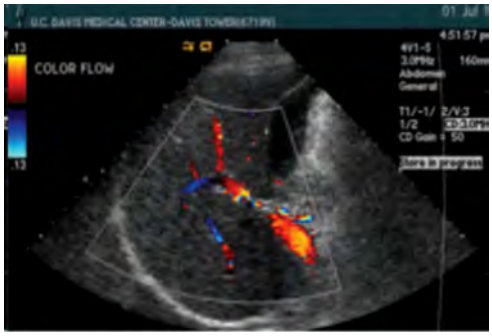

Figure 2.9: *Color Doppler imaging showing veins as blue color and arteries as red color. The color bar shows the speed level. [25].*

In this chapter it was discussed about traditional US imaging techniques, which are common in clinical setups. However, this techniques has limitations. First, the signal acquired form microcirculations is very low, as result it is difficult detect microcirculations. Second in some cases the contrast is very low and it is awkward to distinguish normal tissue from defected tissue. Due to this problems, now a day's ultrasound contrast agents also known as microbubbles are used to alleviate this challenges. Hence, in the next chapter it will be discussed about microbubbles and how they improve traditional ultrasound imaging.

CHAPTER 3

Ultrasound Contrast Agents

3.1 Introduction

Gray scale ultrasound (US) imaging enables to visualize differences between and within tissue structures. However, ultrasound differentiation of normal from abnormal tissue is sometimes difficult. This may be due to the fact that even when tissues are pathologically different, their ultrasonic properties may be quite similar [32]. For instance, tissue like blood, a fluid composed of plasma and blood cells are similar to each other acoustically. As a result, the echoes from blood are completely masked by the neighboring tissue response, remains relatively dark in an echo image [1].

To overcome the limitations of conventional US, gas bubbles of micrometer radius are introduced into a patient's bloodstream as agents for contrast enhanced US (CEUS) imaging [1]. Medical ultrasound imaging is based on the pulse echo principle and these microbubbles are excellent US scatterers due to their high reflectivity (echogenicity). Hence, increasing the received signal strength is, therefore, the objective of most ultrasonic contrast agents (see Fig. 3.1) [32]. To summarize, contrast agents improve the sensitivity of conventional US

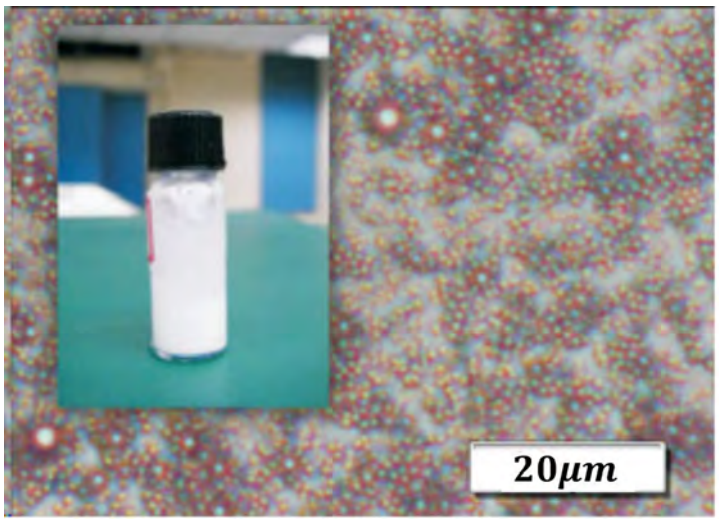

Figure 3.1: *Bright-field microscopic images of microbubbles [34].*

imaging to the micro-circulation and are nowadays used in various medical investigations [34]. For instance, they make blood better detectable in B-mode and Doppler mode imaging, even small vessels [35–37]. In addition, they are also used to enhance detection of flow within abnormal vessels, including tumor vascularization and stenotic vessels, quantify the perfusion of various organs, like liver or kidney and provide better delineation of ischemic areas [38].

3.2 Structure and composition of contrast agents

Typical microbubbles used for biomedical purposes are composed of two main parts, gas core and shell as shown in Fig. 3.2. The gas core is a single chamber and comprises a large majority of the total particle volume and provides the mechanism for US backscatter by expansion during the rarefaction phase of the pressure wave and contraction during the compression phase [39]. Whereas, the shell (membrane) acts as a barrier between the encapsulated gas and the surrounding aqueous medium. Moreover, different shell materials, which are biodegradable may be used, including lipid (3 nm thick), protein (15-20 nm thick) and polymer (100-200 nm thick) [39].

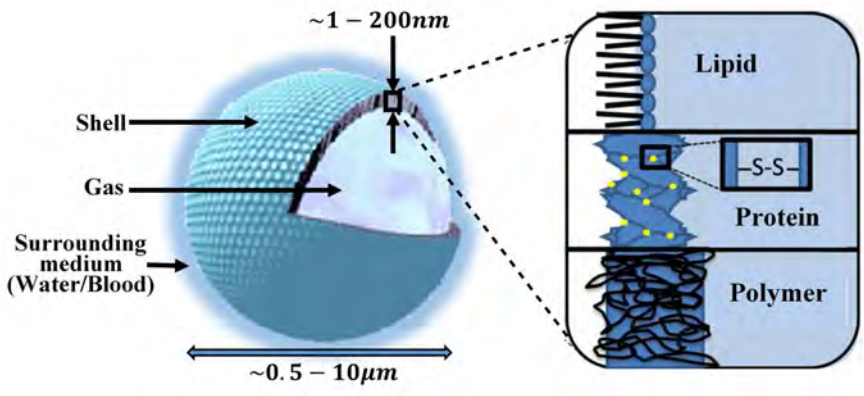

Figure 3.2: *Structure and composition of typical microbubbles [39].*

3.3 Production and administration of contrast agents

Echogenic gaseous microbubbles (colloidal bubbles) are produced by chemical reaction and/or mechanical agitation [24]. During early time of the discovery of ultrasound contrast agents, air bubbles were formed with wide distribution of sizes by hand-agitated, rigorously stirring saline solution [40]. However, one of the problems of gas bubbles formed principally by means of agitation was that they varied in size and were often too large to pass through the pulmonary capillaries [32].

Moreover, these bubbles would have a very short lifetime in the order of a few seconds [24]. Consequently, agitation is no longer used to form gas bubbles instead insonification of saline solution, which is capable of producing microbubbles, which are significantly smaller, more uniform, and stable than those created by hand agitation [32]. Over the years, insonification of solutions has become the most common approach for the generation of ultrasound contrast material [32]. Nonetheless, agitated saline is also still used for the detection of right-to-left shunts in the heart [41].

Table 3.1: *Currently marketed ultrasound contrast agents [42].*

Brand name	Manufacturer	Year approved	Inner gas	Outer shell	Approved for	Marketed in
Optison	GE Healthcare	1997	Perflutren	Albumin	LVO/EBD	USA, Europe
Definity/ Luminity	Lantheus Medical Imaging	2001/2006	Perflutren	Lipid	LVO/EBD, Liver[a], Kidney[a], DAV[a]	USA, Canada, Europe, Australia, parts of Asia
Sonovue/ Lumason	Bracco Imaging	2001/2014	Sulfur hexafluoride	Lipid	LVO/EBD, Breast[a], Liver[a], DAV[a]	North America, New Zealand, Europe, Brazil, parts of Asia
Sonazoid	GE Healthcare	2007	Perflubutane	Lipid	Liver[a], Breast[a]	Japan, South Korea

[a] Only in certain countries. LVO, left ventricular opacification; EBD, endocardial border definition; DAV, diagnostic assessment of vessels. GE, general electric.

3.4 Requirements of contrast agents

An ideal US contrast agent should be non-toxic, injectable intravenously, capable of traversing the pulmonary capillary bed after a peripheral injection, stable enough to achieve enhancement for the duration of the examination and uniform in size [24, 38].

3.4.1 Non-toxicity

Obviously, the shell material and filling gas should be selected so as to satisfy standard pharmacological/toxicological requirements [40, 43]. This includes that the gas used should be inert, which doesn't generate toxicity during metastasis and for this reason, the perfluoro gases have been chosen, in which a carbon chain has its hydrogen atoms replaced by fluorine or Sulphur [40]. In addition, microbubbles must be cleaned through the immune and respiration system. United states food and drug administration (FDA) approved gases is listed in Tab. 3.1).

3.4.2 Capable of traversing pulmonary circulation

Ultrasound contrast agents are often administered by injection intravenously into the bloodstream, which would minimize the risk of intra-arterial injection [24, 44]. Consequently, blockage of any blood vessel supplying a major organ could have extremely serious, even fatal results [43]. Therefore, to allow the applications of these agents to image parts of the body safely, microbubbles are produced having dimensions less than smallest blood vessel (i.e. between 1 and 10 μm) with a mean diameter of 2-3 μm [2, 5].

3.4.3 High echogenicity than tissue

The high echogenicity of microbubbles is as a result of their compressibility during volumetric oscillation (pulsation). Consequently, they scatter much more energy than rigid spheres of the same size would do [43]. This compressibility of microbubbles arises from their gas cores, which creates a mismatch in acoustic impedance between microbubbles and surrounding tissues. Subsequently they become highly echogenic in vivo [34] and hence the scattering effect is maximized. For instance, once microbubbles are administered into a body cavity or the cardiovascular system, they are capable of increasing the intensity of backscattered ultrasound up to 20-30 dB [45, 46]. Nevertheless, the increase in intensity depends on the applied acoustic field and characteristics of the contrast agent particles (CAP) [43].

3.4.4 Stability

Stability of free microbubbles

Stability of microbubbles is crucial in order to achieve enhancement for the duration of the examination. However, free air bubbles (bubble without shell) have a very short lifetime, which is not suitable for human applications [24]. In addition, maintaining microbubbles suspended in a liquid at a constant size is technically challenging. Stability of microbubbles is

affected by: changes in environment, surface tension between gas-liquid interface and acoustic pressure [5, 41]. These effects eventually will result in dissolution of microbubbles. The dissolution time of microbubbles is calculated using Epstein and Plesset equation [47] and Ostwald coefficient [48] and it is used to compare dissolution of microbubbles. Ostwald coefficients for different gases and their predicted dissolution time is listed on Tab. 3.2.

Table 3.2: *Ostwald coefficient and disappearance time for 3 μm diameter bubbles containing different gases [5].*

Gases	**Ostwald coefficient (x10^6)**	**Disappearance time (s)**
Air	23,168	0.02
Sulfur hexafluoride (SF_6)	5,950	0.1
Perfluoropropane (C_3F_8)	583	1.1
Perfluorohexane (C_6H_{14})	24	2

Although, maintaining microbubbles stability is challenging, it could be achieved by wisely selecting the gas and the shell type used. Hence, the first effective way to reduce dissolution is to choose gases with higher molecular weight (lower Ostwald coefficients), such as perfluorocarbons (Definity, Sonazoid, and Optison) or sulfur hexafluoride (SonoVue) [5]. These gases with higher molecular weight reduce the solubility or diffusion time of the microbubble, [5] prolonging their effective life in the circulation, where they are subject to mechanical trauma by the action of heart valves and by the US beam [5, 40]. Although these gases slow down microbubble dissolution time compared to air, still free gas bubbles do not persist long enough to be of practical use in the human body [5].

Stability of coated microbubbles

The second way to increase dissolution time of microbubbles is the addition of materials at the gas-liquid interface [5]. This material is known as coating material (surfactant shell). It has a strong influence on the microbubbles response to an acoustic pressure and plays a key role in characterizing the behavior of bubbles [5]. Surfactant layer is comprised of proteins, lipids or polymers.

Coating microbubbles has several advantages, such as stabilizing bubbles by dampening vibrations, preventing coalescence to form larger bubbles, greatly reducing the surface tension

at the interface and preventing dissolution [40]. For instance, both polymer and albumin enhance the bubble's stability by supporting a strain to counter the effect of the surface tension. However, now more commonly used surfactants are coated by lipids [40, 49]. Current commercially available agents like Sonovue, Definity (both phospholipids), Optison (human albumin), and Sonazoid (lipids) are approved for human use and all are coated [5, 49].

3.5 Microbubbles ultrasonic response

When microbubbles are subjected to an US oscillating pressure field, they undergo oscillation in response to the pressure changes of the US pulse. The major parameter affecting microbubble behavior the local acoustic power [38]. It is described by mechanical index (MI), which is directly proportional to the peak rarefactional (negative) pressure and inversely proportional to the square root of the ultrasound frequency (in MHz) and is given by

$$MI = \frac{P_N}{\sqrt{\nu}}, \tag{3.1}$$

where P_N is the peak negative pressure of the US wave in megapascals (MPa), and ν the center frequency of the US wave in megahertz (MHz). Even though the MI has a dimension, it is typically reported as a dimensionless number [5]. The vibration of microbubbles is related either linearly or non-linearly to the applied acoustic pressure field based on the incident US beam.

Low acoustic power (i.e. $MI < 0.1$) [29] the instantaneous radius oscillates linearly and symmetrical in relation to the amplitude of the applied external pressure field, and the frequency of the backscattered US is equal to that of the transmitted US [34]. Low MI imaging is appropriate for Doppler applications as well as for real-time contrast imaging, if a sufficient acoustic response can be obtained from the microbubbles [38].

Intermediate acoustic power (i.e. $0.1 < MI < 0.5$) the bubbles oscillations increase in amplitude and become asynchronous with the ultrasound wave [38]. The pulsation of the bubbles becomes more nonlinear (not essentially sinusoidal) [2, 5, 38]. Consequently, the bubbles start to produce harmonic US waves, which are different from that of the incident wave (fundamental frequency). These harmonics are multiples of the transmitted fundamental frequency: subharmonic frequency (e.g., half the fundamental frequency), second harmonics (twofold the fundamental frequency) and ultra-harmonics which can be obtained at 1.5 or 2.5

times the fundamental frequency [34, 38].

High acoustic power (i.e. $MI > 0.5$) further increasing acoustic power results in complex highly non-linear bubble behavior, which can be revealed by phenomena like bubble collapse (diffuse into the surrounding fluid) within a very short time, fragmentation and merging [2, 34]. This eventually results in bubble destruction, which produces a strong transient echo, very rich in non-linear components, which could provide the most sensitive detection of US contrast agents particularly when coupled with color or power Doppler [38].

The strategies for contrast imaging are currently based on either the linear or nonlinear properties of microbubbles [34].

3.6 Characterization of microbubbles

Microbubbles dynamics are often characterized using two techniques [5], acoustic and optical. The former technique is based on the measurement of attenuation and scattering. Whereas, the latter is based on recordings of oscillation of individual bubbles using optical setup and using a fast framing camera. Both methods have their own advantages and disadvantages (discussed in Sec. 3.6.1 and Sec. 3.6.2).

3.6.1 Acoustic characterization

Acoustic characterization is done by insonifying microbubbles and measuring acoustic responses (Fig. 3.4), the absorbed and scattered energy of the microbubbles [5]. The acoustic measurement is helpful to determine average elasticity and viscosity of microbubbles. In addition, recent in vitro studies have shown that single bubble responses can be measured acoustically [7, 11, 12]. However, there are three main challenges with single bubble measurements. First, it is difficult to isolate single microbubbles within an ultrasound beam. Secondly, it is difficult to prevent bubble destruction and to operate in the linear regime. Finally, in order to quantify the size-dependent shell properties, the corresponding initial bubble radius should be measured accurately [7]. Nevertheless, the three difficulties could be addressed by applying filtering mechanism of single bubble [7].

The experimental setup for single bubble acoustic characterization is shown in Fig. 3.3. Acoustic responses of single microbubbles are measured at low pressure amplitudes using a highly sensitive calibrated receiving transducer. The bubbles are isolated in a capillary tube

and their resting radii are determined by optical means. The measured bubble responses are analyzed and compared to numerical simulations using a Rayleigh-Plesset-type equation, incorporating the viscoelastic properties of the phospholipid shell [7]. Despite its advantages,

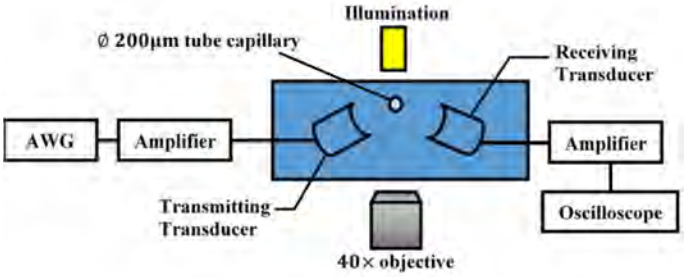

Figure 3.3: *Single bubble characterization experimental setup [50]*

there are few drawbacks with this filtering mechanism. For instance, it does not give direct measurement of bubble size and it requires highly sensitive calibrated receiving transducer. Moreover, phenomenas such as "compression-only" [50, 51], "thresholding" [51] behavior and non-spherical oscillations are not observed [52, 53].

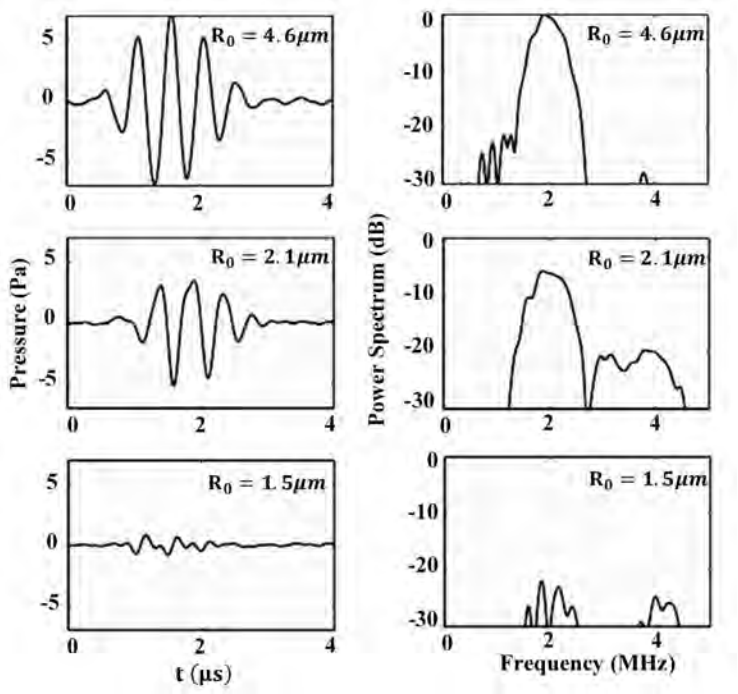

Figure 3.4: *Measured acoustic responses of three single bubbles of different sizes excited with a driving pressure of 100 kPa. The response amplitude decreases with decreasing bubble radius. Furthermore, the second harmonic response is highest for the bubble closest to resonance size, i.e.,* $R_0 = 2.1\mu m$ *[7].*

3.6.2 Optical characterization

Instead of only listening bubbles sound echo, it is much interesting to see source of these sounds, which is bubble vibration. It is based on recordings of oscillation of individual bubbles using optical setup and using a fast framing camera. Watching bubbles has several advantages over listening [5]. The wavelength of light is much shorter than that of ultrasound, typically 0.5 μm and 500 μm, respectively [5]. Consequently, optical observations are more accurate in characterizing individual bubbles. In addition, it enables to observe the source of oscillation and how each bubble behaves under the influence of ultrasound as shown in the Fig. 3.6. Moreover, optical observation enables to discriminate individual bubbles easily and provides direct quantitative information on bubble size (Fig. 3.7 and Fig. 3.8).

Several authors have shown that high-speed optical recordings provide quantitative information on the dynamic behavior of single microbubbles in an US field [15, 54]. Detailed experimental set-up for an optical measurement system and high-speed camera system is described by C. T. Chin and C. Lancée [18]. The basic setup for taking pictures of oscillating contrast agent microbubbles is shown in Fig. 3.5.

In spite of its advantages, optical observation has some limitations [7]. It is costly and of limited availability. In addtion, due to the limited resolving power of the optical system, it is unable to detect small radial displacements (< 30 nm) at low acoustic pressure amplitudes (on the order of 20 kPa). Furthermore, it does not provide direct quantitative information on the amplitude of oscillation of the microbubble.

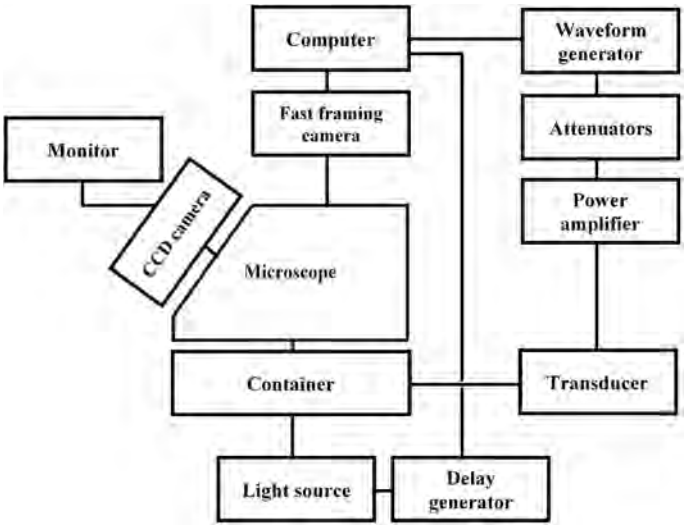

(a) *Basic setup block diagram*

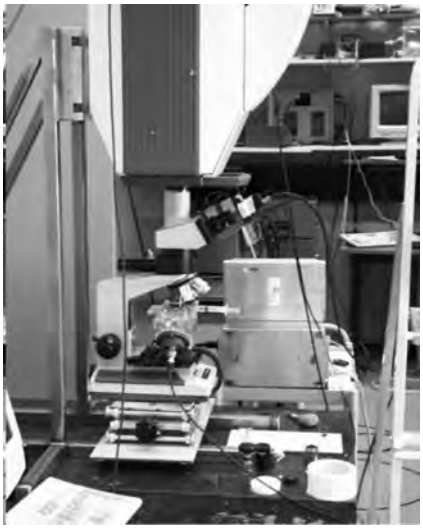

(b) *Actual setup*

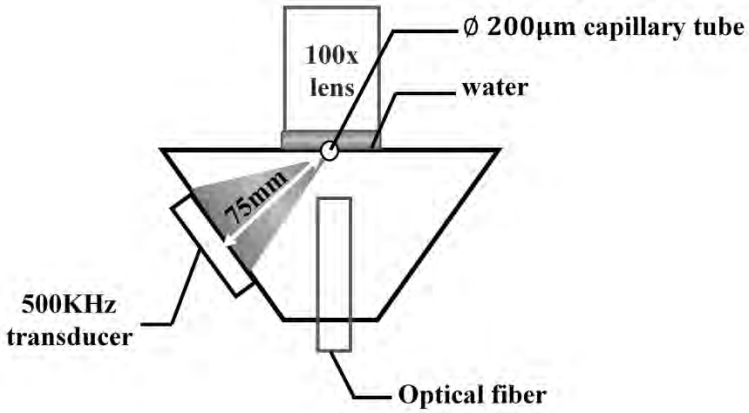

(c) *Container front view*

Figure 3.5: *(a) Basic setup block diagram, (b) Actual setup, and (c) Container front view [2].*

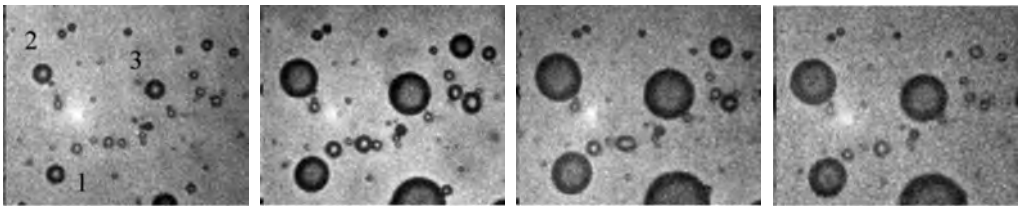

(a) ***(b)*** ***(c)*** ***(d)***

Figure 3.6: *Optical image sequence of three microbubbles with apparently the same initial diameters, insonified at MI = 0.93. Each frame corresponds to a* $55 \times 45 \mu m^2$ *area. Frame (a) was taken before ultrasound arrival. The microbubbles expanded to different maximal diameters (b)-(d) [2].*

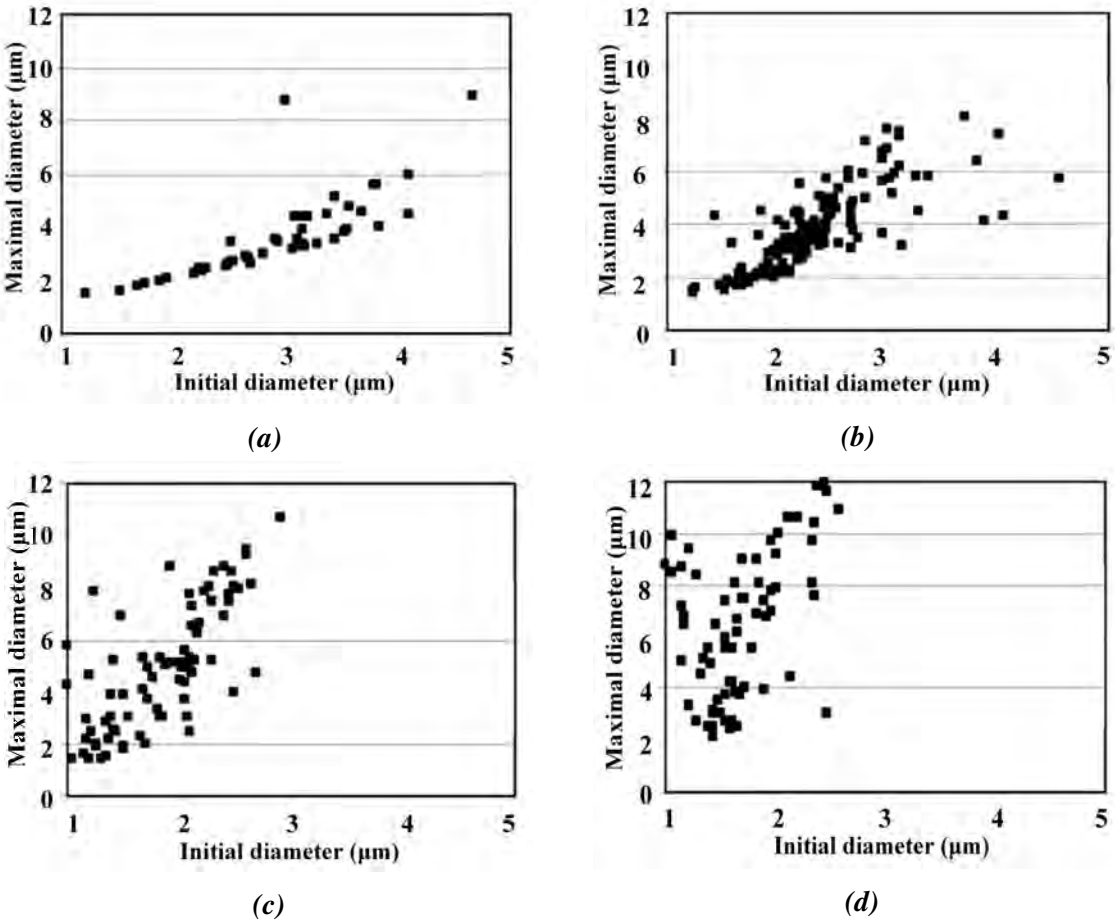

Figure 3.7: *Bubble expansion at four different acoustic pressures. (a) MI = 0.089, (b) MI = 0.15 (c) MI = 0.25, and (d) MI = 0.39 [2].*

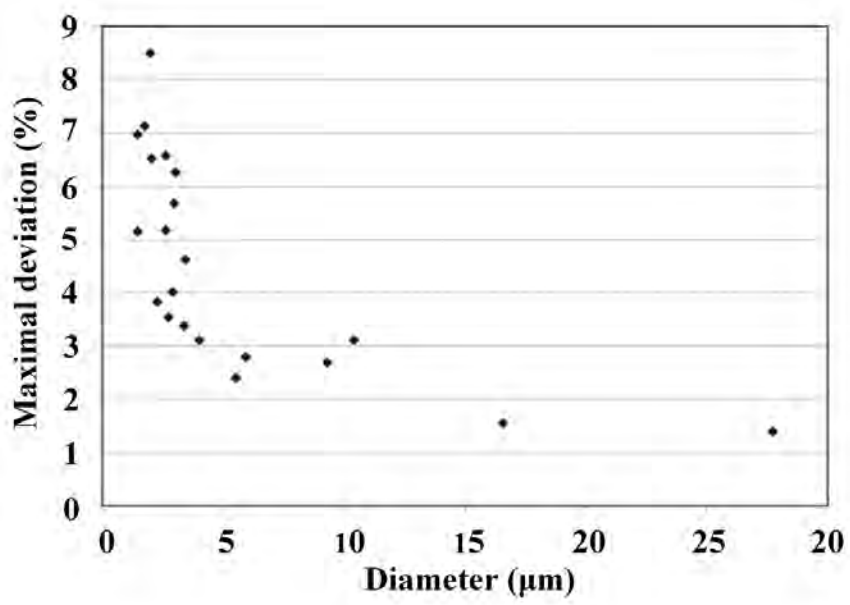

Figure 3.8: *Maximal deviation in bubble measurement due to random error as a function of mean bubble diameter measurement [7].*

CHAPTER 4

Physics of Light Microscopy

4.1 Introduction

A compound light microscope is an optical instrument, as the name implies it uses visible light and optical components in order to magnify an image of an object (specimen). The word compound refers to the two lenses, the objective and ocular (eyepiece) which work together to produce the final magnification.

Arrangement and different parts of basic light microscope are shown in Fig. 4.1. Of all these components, the critical important components in image formation are the objective lens and condenser lens. The former is responsible in gathering light diffracted by the specimen and formation of magnified real image near the eyepieces and the latter is responsible for focusing of light from the illuminator onto a small area of the specimen. Other components which are less critical to image formation include the eyepieces (lens the viewer looks through), microscope stage (where the slide is placed), stage clips (metal clips that hold the slide in place), lamp (for illumination of specimen), condenser diaphragm (controls the angle of illuminating wavefronts that bathe the specimen), field stop diaphragm (limits the brightness of light reaching the focal plane), lamp socket and its cord, filters (for increasing contrast, for selectively transmitting only wanted wavelengths), polarizers (for contrast-enhancing), retarders (alters the polarization state or vibration plane of a light wave), and stand with coarse and fine (tunes the focus and increases the detail of the specimen) focus dials [57]. Detailed description of each and other components is beyond the scope of this thesis and readers could consult previous literatures for this purpose [55].

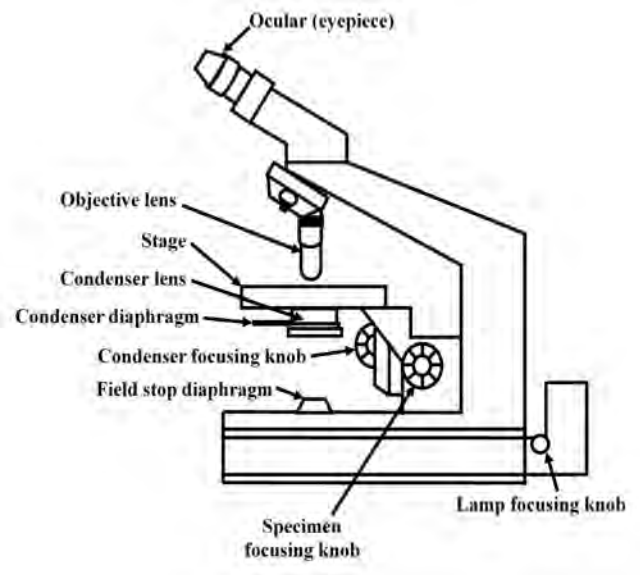

Figure 4.1: *Components of a typical compound light microscope.*

4.2 Optical parameters of light microscopy

Refractive index

It is also known as index of refraction, n, which describes how light propagates through a medium. Refractive index of a medium is calculated as

$$n = \frac{c}{\mathrm{v}} \tag{4.1}$$

where c is the speed of light in a vacuum, and v is speed of light in other medium such as glass or biological material. Refractive indices for different materials are listed on Tab. 4.1.

Table 4.1: *Refractive indices for different materials [58, 59].*

Materials	**Approximate Index**
Vacuum (also close for air)	1.00
Water (visible to NIR[1])	1.33
Oil	1.51
Glass	1.52
ZnSe (infrared)	2.40
Germanium	4.00

[1] NIR, Near infrared.

Focal length

Focal length, f, is the value that describes the ability of the optical system to focus light. It is the distance from the lens to the image plane (detector) when a point source located at infinity

is imaged in focus [56]. That is,

$$d_f = \infty \Longrightarrow d_i = f$$
$$d_i = \infty \Longrightarrow d_f = f$$

where f is the focal length of the lens, d_f and d_i are distance of specimen and image from the lens respectively as shown in Fig. 4.2.

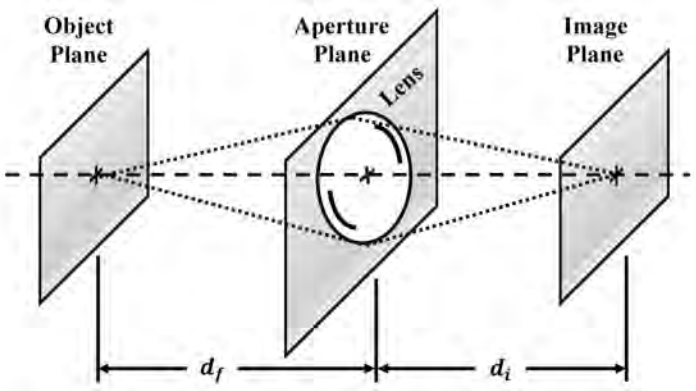

Figure 4.2: *An optical system consisting of a single lens, d_f is focal distance from specimen to aperture plane and d_i is focal distance from aperture (lens) to image plane.*

The power of a lens, P, is given by $P = 1/f$; if f is given in meters, then P is in diopters. By definition, the focal plane is that plane in object space where a point source will form an in-focus image on the image plane, given a particular d_i [56]. The focal length is given by lensmaker's equation:

$$\frac{1}{f} = (n-1)\left(\frac{1}{R_1} - \frac{1}{R_2}\right). \tag{4.2}$$

Where, R_1 and R_2 are lens front and back radii of curvature.

Numerical aperture

The numerical aperture, *NA*, of a microscope objective is a measure of its ability to gather light and thus resolve fine specimen detail at a fixed objective distance [60]. The numerical aperture is formulated as [61]:

$$NA = n\sin(\alpha) \approx n\,(D/2f)\,, \tag{4.3}$$

where n is refractive index of the medium located between the front lens of the objective and the specimen cover glass, f is the focal distance, D is diameter of the numerical aperture and α is known as acceptance angle, which is one half of the angular aperture, which could range up to 90° theoretically as shown in Fig. 4.3. The bigger the acceptance angle α, the higher is the numerical aperture and the more light is collected. The approximation in Eq. (4.3) assumes

small aperture and high magnification, respectively. These approximations begin to break down at low power and high *NA*, which normally do not occur together [56].

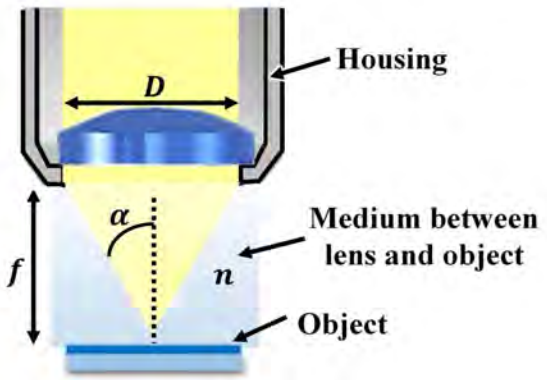

Figure 4.3: *Angular aperture of an objective lens.*

Resolution

Resolution, Res, or resolving power of a microscope is its ability to distinguish two objects from one another [62], when they are in close proximity (see Fig. 4.4). In the bright-field microscopy, where *NA* of the objective $(NA_{obj}) > NA_{cond}$, the *xy* resolution is given as [57]:

$$Res = \frac{1.22 * \lambda}{NA_{obj} + NA_{cond}}, \tag{4.4}$$

where λ is the wavelength. On the other-hand when NA_{cond} is adjusted to that of NA_{obj}, i.e. the aperture of the condenser is essentially the same as the objective aperture, then Eq. (4.4) simplifies to:

$$Res = \frac{1.22 * \lambda}{2NA_{obj}}. \tag{4.5}$$

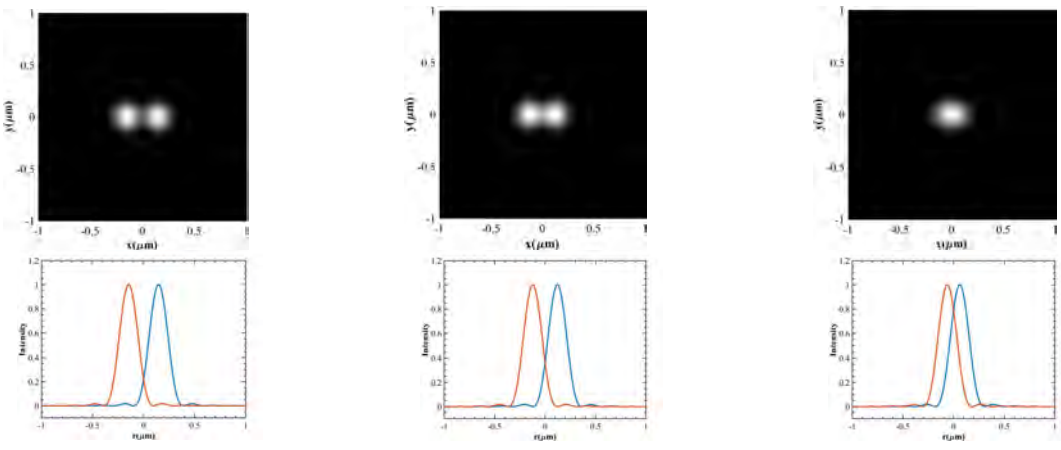

(a) ***(b)*** ***(c)***

Figure 4.4: *Resolving two points at different distances and their intensity profiles. (a) Two points resolved, (b) Resolution limit (Rayleigh limit, first diffraction minimum coincides with maximum of other), and (c) Not resolved.*

Depth of focus

Depth of focus (DOF) is the distance Δz over which the image specimen can be expected to be observed without significant optical aberration (loss of sharpness in the image) which can be derived from considerations of wave optics as [63]:

$$\Delta z = \frac{\lambda}{4n\left(1-\sqrt{1-\left(\frac{NA}{n}\right)^2}\right)}. \tag{4.6}$$

4.3 Basic physics of light

4.3.1 Dual nature of light

Visible light, the agent used as the analytic probe in light microscopy, is a form of energy known as electromagnetic (EM) field. EM wave is a synchronized oscillation of electrical and magnetic fields. This energy is contained in discrete units or quanta called photons that have the properties of both particles and waves [57]. Light as a particle possesses a momentum. These photons are detected as individual quanta of energy (as photoelectrons) on the surfaces of quantitative measuring devices such as charge-coupled device (CCD) or photomultiplier tubes [57]. On the other hand, light as wave exhibits an oscillation with specific frequency [66]. This dual-character description of light, which is also shared by matter is described in Fig. 4.5.

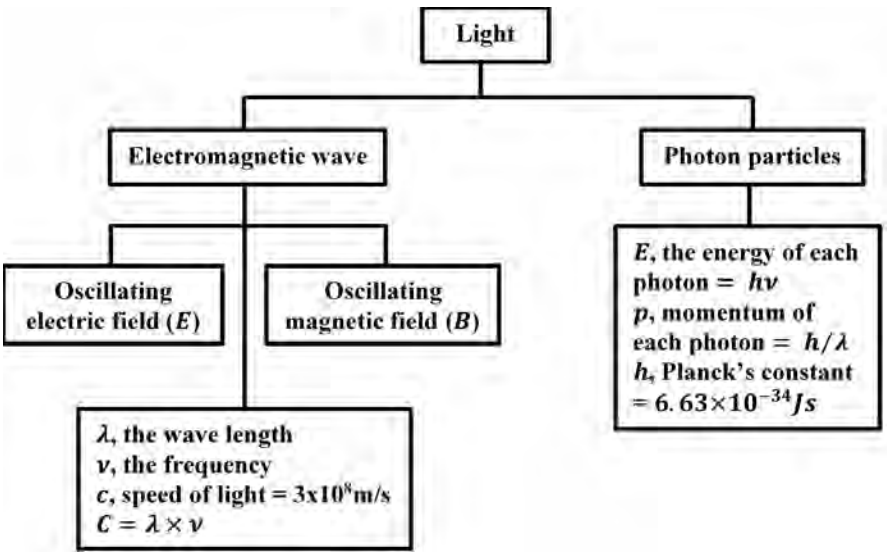

Figure 4.5: *Dual characteristics of light.*

4.4 Light as waves interaction

4.4.1 Superposition

When two separate waves arrive at the same place wherein they overlap, they will simply add to (or subtract from) one another without permanently destroying or disrupting either wave [69]. The resulting disturbance at each point in the region of overlap is the algebraic sum of the individual constituent waves (Fig. 4.6) at that location. This recombination and summation of two or more superimposed waves is known as superposition. The addition of two initial waves produces a resultant wave whose amplitude may be increased (constructive interference) or diminished (destructive interference) as shown inFig. 4.6 [57].

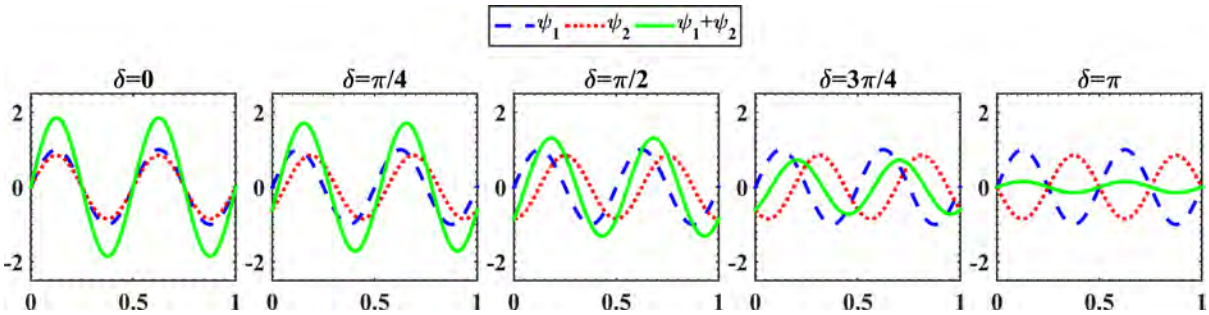

Figure 4.6: *The sum* $\psi = \psi_1 + \psi_2$ *(green) of the waves* $\psi_1 = 1.0\sin(kz)$ *(blue) and* $\psi_2 = 0.85\sin(kz - \delta)$ *(red), plotted for various values of* δ.

4.4.2 Diffraction

Diffraction is the apparent bending of light (wave) as it passes around the edge (corner) of an object (barrier) and the spreading out of waves as they pass through openings (aperture) (see Fig. 4.7). Diffraction phenomena depends upon the size of obstacle and amount of bending depends on the relative size of the wavelength of light to the size of the opening. If the opening is much larger than the light's wavelength, the bending will be almost unnoticeable. However, if the size of obstacle is comparable to the wavelength of light, the amount of bending is considerable, and easily seen with the naked eye [57, 67].

In the microscope, light from the illuminator is diffracted by the specimen, collected by the objective lens, and focused in the image plane, where waves constructively and destructively interfere to form a contrast image [57]. Interference and diffraction have no significant physical distinction. The only distinction is on the number of waves that interfere. If only few waves are superimposing it is considered as interference. On the other hand, if we are treating large number of superimposing waves it is considered as diffraction [69].

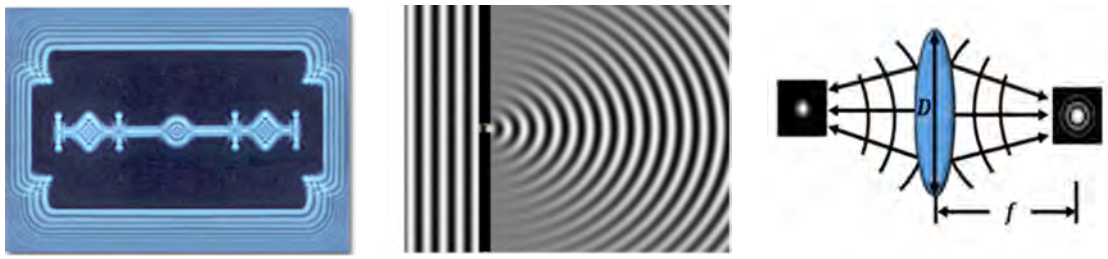

(a) *(b)* *(c)*

Figure 4.7: *Diffraction when: (a) Light encounters a sharp edge of a razor blade, (b) Light passes through a small aperture, and (c) Light is focused on a small spot [68]*

Diffraction by an arbitrary aperture

Consider the configuration depicted in Fig. 4.8. A monochromatic plane wave propagating in the z-direction is incident on the opaque diffracting screen Σ. We now want to find the consequent flux-density distribution in space or equivalently at some arbitrary distant point P.

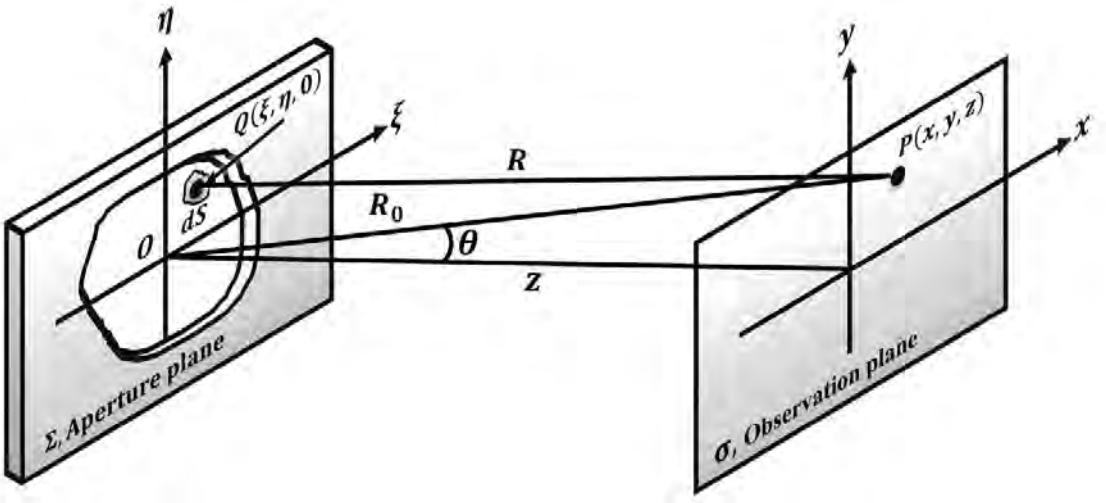

Figure 4.8: *Geometry of diffraction by an arbitrary aperture.*

Each point on the aperture plane Σ emits a spherical wavelet, which is written as

$$U(Q) = U_0 \frac{e^{jkR}}{R}, \tag{4.7}$$

where R is distance between point field source $Q(\xi,\eta,0)$ on the aperture plane and point $P(x,y,z)$ on the observation plane (σ), and U_0 is the source strength.

The field strength at point p for a differential area dS, within the aperture yields [66, 69],

$$U(x,y,z) = -\frac{jk}{2\pi} \iint_S U(\xi,\eta,0) \frac{e^{jkR}}{R} dS. \tag{4.8}$$

Equation (4.8) expresses the observed field $U(x,y,0)$ as a superposition of diverging spherical waves $\left(e^{jkR}/R\right)$ originating from secondary sources located at each and every point Q within the aperture S. Moreover, R doesn't change very much as Q varies over S. Thus, R in the denominator can be assumed to be constant at a value R_0. However, change in R in the exponent should be taken into account, since it produces a multiplicative factor [59]. In addition, Eq. (4.8) can be further simplified by making certain assumptions about R. The point of observation is very distant from the coherent line source and $R_0 \gg a$, where a is the radius of the aperture. Under these circumstances R never deviates appreciably from its midpoint value R_0. Consequently, that the field at P becomes

$$U(x,y,z) = -\frac{jk}{2\pi}\iint_S U(\xi,\eta,0)\frac{e^{jkR}}{R_0}dS. \tag{4.9}$$

Since $z = R_0\cos(\theta)$, for small angle θ (angle measured between $(\xi=0,\eta=0,z=0)$ and (x,y,z)), R_0 can be taken to be equal to z. Having made this approximation, we can bring the $1/z$ outside the integral. Which results

$$U(x,y,z) = -\frac{jk}{2\pi z}\iint_S U(\xi,\eta,0)e^{jkR}dS. \tag{4.10}$$

Now, the distance R between the point $Q(\xi,\eta,0)$ and $P(x,y,z)$ can be calculated as

$$\begin{aligned} R &= \sqrt{(x-\xi)^2+(y-\eta)^2+z^2} \\ R &= z\sqrt{(\frac{x-\xi}{z})^2+(\frac{y-\eta}{z})^2+1} \end{aligned} \tag{4.11}$$

For $(x-\xi) \ll z$ and $(y-\eta) \ll z$, R can be approximated by first-order Taylor's[1] series [58]

$$\begin{aligned} R &\approx z\left[1+\frac{(x-\xi)^2}{2z^2}+\frac{(y-\eta)^2}{2z^2}\right], \\ R &\approx z+\frac{(x-\xi)^2}{2z}+\frac{(y-\eta)^2}{2z}. \end{aligned} \tag{4.12}$$

Using the distance approximation in Eq. (4.12), Eq. (4.10) yields

$$U(x,y,z) = -\frac{jke^{jkz}}{2\pi z}\iint_S U(\xi,\eta,0)e^{jk\left[\frac{(x-\xi)^2}{2z}+\frac{(y-\eta)^2}{2z}\right]}d\xi d\eta. \tag{4.13}$$

[1] $\sqrt{1+x} = 1+\frac{1}{2}x-\frac{1}{8}x^2+\frac{1}{16}x^3+\ldots,$

Expanding and regrouping the transverse-position terms in the exponent,

$$(x-\xi)^2+(y-\eta)^2=(x^2+y^2)+(\xi^2+\eta^2)-2(x\xi+y\eta), \tag{4.14}$$

results different form of Eq. 4.13

$$U(x,y,z)=-\frac{jke^{jkz}}{2\pi z}e^{jk\frac{\left(x^2+y^2\right)}{2z}}\iint_S U(\xi,\eta,0)e^{jk\frac{\left(\xi^2+\eta^2\right)}{2z}}e^{-jk\frac{(x\xi+y\eta)}{z}}d\xi d\eta. \tag{4.15}$$

Eq. (4.15) is general diffraction equation.

Fraunhofer (Far-field) diffraction formula

For any finite aperture of diameter D with sufficiently large z, far-field condition is satisfied [58] when

$$z \gg D^2/\lambda \tag{4.16}$$

Then $r_f=\sqrt{2\lambda z}\gg\sqrt{2D}$ for all $\xi,\ \eta$ within the aperture and Fresnel number is small,

$$N_f=r/r_f\ll 1 \text{ (Fraunhofer zone)}, \tag{4.17}$$

Now, in Fraunhofer zone, where $r_f\gg\frac{k}{2}\left(\xi^2+\eta^2\right)$

$$e^{jk\frac{\left(\xi^2+\eta^2\right)}{2z}}\approx 1 \tag{4.18}$$

Hence, the integral Eq. (4.15) results, Fraunhofer formula,

$$U(x,y,z)=-\frac{jke^{jkz}}{2\pi z}e^{jk\frac{\left(x^2+y^2\right)}{2z}}\iint_S U(\xi,\eta,0)e^{-jk\frac{(x\xi+y\eta)}{z}}d\xi d\eta. \tag{4.19}$$

Eq. (4.19) is a 2D Fourier transform[2] of $U(\xi,\eta,0)$, which can be integrated in closed form. This region is known as far-field region (zone).

Fraunhofer diffraction by circular aperture

In the study of optical instrumentation, Fraunhofer diffraction at a circular aperture is an effect of great practical significance [69, 72]. Fraunhofer diffraction requires that the waves leave the aperture in a nearly parallel bundle traveling toward a very distant point P. Hence, lens is used to form a point image of this parallel bundle at a much closer distance to the aperture without changing the pattern. A typical arrangement of circular diffraction is shown in Fig. 4.9.

A plane wave impinges a circular aperture contained by a screen Σ and far-field diffraction pattern spread across distant observing screen σ. Moreover, the lens is merged with the aperture

[2] $\mathscr{F}\{f(x,y)\}=F(\xi,\eta)=\int_{-\infty}^{\infty}\int_{-\infty}^{\infty}f(x,y)e^{-j2\pi(x\xi+y\eta)}dxdy$

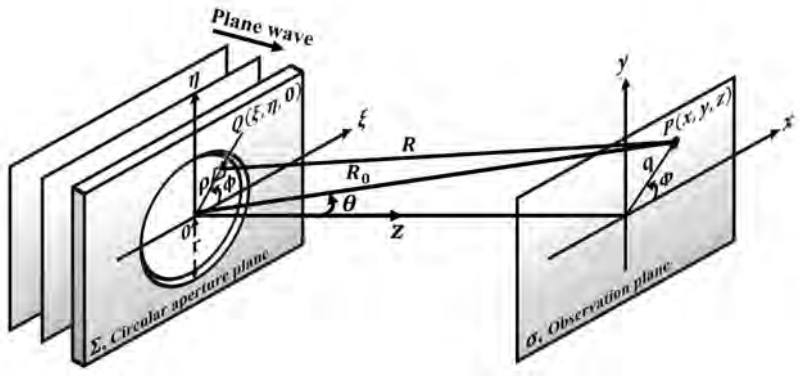

Figure 4.9: *Geometry of diffraction by a circular aperture.*

in Σ screen, because in practice the edge of the lens also defines the aperture and the form of the pattern is basically intact. The light wave reaching Σ is cropped, so that only a circular segment propagates through lens to form an image in the focal plane. The xy and $\xi\eta$ are the focal plane of the lens and aperture plane coordinate system respectively. Point P is general point but very close to the origin of the observation plane.

The aperture plane and $U(\xi,\eta,0)$ describe the aperture:

$$U(\xi,\eta,0) = \begin{cases} 1, & \rho(\xi,\eta,0) \leq r \\ 0, & \rho(\xi,\eta,0) > r \end{cases} \tag{4.20}$$

where $\rho = \sqrt{\xi^2+\eta^2}$ is the radial distance from the center of the lens to the source S of the emitted wave. Now, letting $U_0 = -\frac{jke^{jkz}}{2\pi z} e^{jk\frac{\left(x^2+y^2\right)}{2z}}$ Eq. (4.19) becomes

$$U(x,y,z) = U_0 \iint_S U(\xi,\eta,0) e^{-jk\frac{(x\xi+y\eta)}{z}} d\xi d\eta. \tag{4.21}$$

Recognizing the angular symmetry of the lens and the diffraction pattern, the aperture and the plane of observation can be converted to polar coordinates. For a wave emitted at a point Q in the lens with coordinates (ξ,η) or angular coordinates (ρ,ϕ) and arrive at P with coordinates (x,y) or angular coordinates (q,Φ),

$$\begin{aligned} \xi = \rho\cos\phi \ , \ \eta = \rho\sin\phi \\ x = q\cos\Phi \ , \ y = q\sin\Phi \end{aligned} \tag{4.22}$$

Here ρ is the angular radius ($\rho = \sqrt{\xi^2+\eta^2}$) of Q and ϕ is its polar angle; q is the angular radius $\left(q = \sqrt{x^2+y^2}\right)$ of P and Φ is its polar angle.

Following Eq. (4.22),

$$x\xi + y\eta = \rho q\cos\phi\cos\Phi + \rho q\sin\phi\sin\Phi = \rho q\cos(\phi - \Phi), \tag{4.23}$$

and differential element of area is now,

$$dS = \rho d\rho d\phi. \tag{4.24}$$

Substituting Eq. (4.23), Eq.(4.20) and Eq.(4.24) into Eq. (4.19), results

$$U(q,z) = U_0 \int_0^{2\pi}\int_0^{r} e^{-jk\frac{(\rho q\cos(\phi-\Phi))}{z}} \rho d\rho d\phi. \tag{4.25}$$

The thorough solution for Eq. (4.25) can be found in various literatures [58, 59, 68]. However, the result is worth mentioning here. Hence, Fraunhofer diffraction for circular aperture becomes

$$U(r,z) = CS\left(\frac{2J_1\left(\frac{krq}{z}\right)}{\frac{krq}{z}}\right) \tag{4.26}$$

and the intensity $I(q,z) = |U(r,z)|^2$,

$$I(r,z) = I_0\left(\frac{2J_1\left(\frac{krq}{z}\right)}{\frac{krq}{z}}\right)^2. \tag{4.27}$$

where $S = \pi r^2$, r is radial distance from the center of the σ to observation point P. $I_0 = C^2S^2 = pS/\lambda^2 z^2$, p is total power incident upon aperture and J_1 is the first-order Bessel function of the first kind (see Appendix B). In addition, Eq. (4.27) can also be expressed in-terms of the angle of observation [70], i.e. the angle (θ) between the axis of the circular aperture and the line between aperture center and observation point,

$$I(\theta) \;=\; I_0\left(\frac{2J_1(kr\sin\theta)}{ka\sin\theta}\right)^2 \tag{4.28}$$

or [2],

$$I(r) = I_0\left(\frac{2J_1(ar)}{ar}\right)^2,\ a = \frac{2\pi NA}{\lambda}, \tag{4.29}$$

where NA is the numerical aperture of the objective lens, and λ is the wavelength of the light. The intensity of the Fraunhofer diffraction pattern of a circular aperture is known as the Airy pattern (Fig. 4.10)

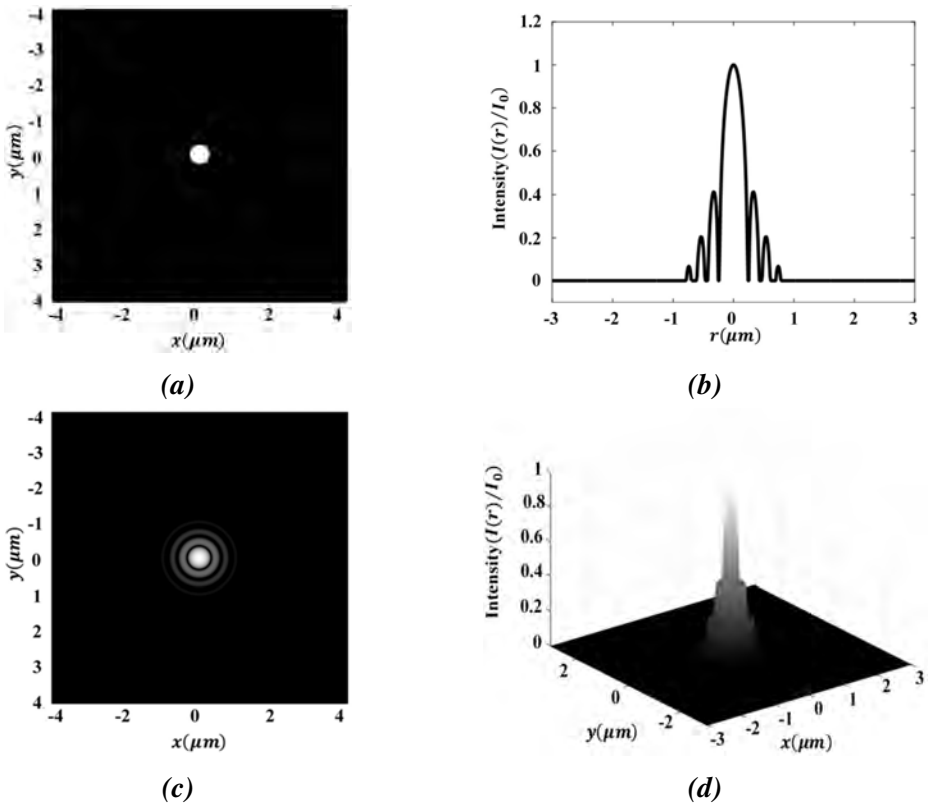

Figure 4.10: *Fraunhofer circular diffraction. (a) Pupil, (b) 1D intensity profile, (c) 2D pattern, and (d) 3D circular diffraction pattern. (For sub figures (b), (c) and (d) the view is in Log scale with 3 decade).*

Axial irradiance through circular aperture

For a circular aperture illuminated with a plane wave, general diffraction equation becomes [59],

$$U(q,z) = \frac{jke^{jkz}}{2\pi z} e^{jk\frac{\left(q^2\right)}{2z}} \int_0^r J_0\left(\frac{k\rho q}{z}\right) e^{jk\frac{\left(\rho^2\right)}{2z}} \rho d\rho. \tag{4.30}$$

Unfortunately, this integral cannot be solved in terms of elementary functions, though it can be solved in terms of Lommel functions [70]. This approach is not particularly useful, and it is usually easier to solve it numerically. However, Eq. (4.30) can be reduced if we take along the z-axis $(x = 0,\ y = 0,\ z)$, which gives axial irradiance [59],

$$\begin{aligned} U(0,z) &= \frac{jke^{jkz}}{2\pi z} \int_0^r e^{jk\frac{\rho^2}{2z}} \rho d\rho \\ U(0,z) &= \frac{jke^{jkz}}{2\pi z} \left[e^{jk\frac{\rho^2}{2z}} \Big|_0^r \right] \\ U(0,z) &= 2je^{jkz} e^{\left(\frac{jkr^2}{4z}\right)} \sin\left(\frac{kr^2}{4z}\right), \end{aligned} \tag{4.31}$$

or

$$U(0,z) = 4\sin^2\left(\frac{kr^2}{4z}\right). \tag{4.32}$$

So we obtain a series of maxima and minima (zeros) in intensity along the z-axis as shown in Fig. 4.11.

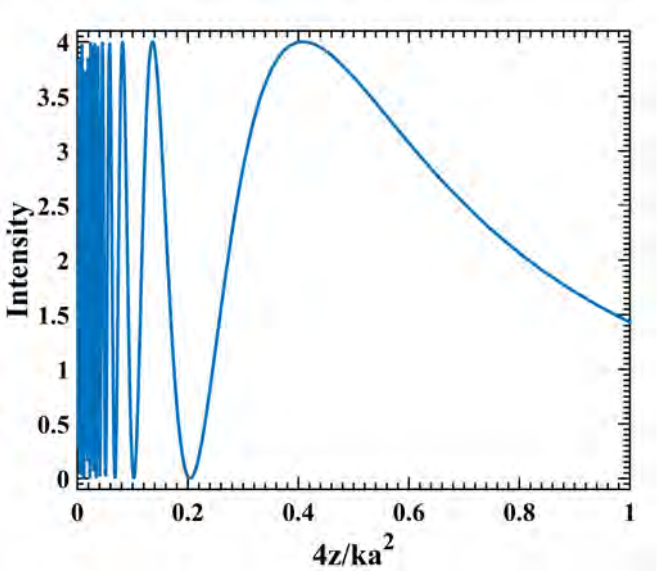

Figure 4.11: *Intensity along the axis of a circular aperture according to the Fresnel diffraction theory.*

In this chapter it is shown that an optical system is mainly characterized by its point spread function, which determines the image formed at the CCD. It is also discussed how light propagates axially, which is determines the intensity of the PSF at different depth of focus. From this, we are able to model the optical system. Therefore, now we can move on to discussing how an optical image is formed at the CCD. Thus, the next chapter is dedicated to discuss how to model an image formation in microscope and how to apply an image processing in order to quantify the image formed.

CHAPTER 5

Optical Image Processing

5.1 Introduction

While optical microscopy is almost 400 years old [73, 74], it has seen steady improvement and growing use in biomedical research and clinical medicine as well as in various other fields [56]. The developments of the past decade have offered a diverse mechanism for investigating biological and material samples, allowing us to peer into spaces much too small to be seen with the naked eye. In the modern age, the images produced by a microscope are converted into digital form for storage, analysis, or processing prior to display and interpretation [57, 75]. This has been possible following introduction of modern electro-optical sensor technologies, modern charge-coupled device (CCD) cameras [74] and the like.

The usage of a light microscope for the quantitative analysis of samples requires an understanding of: nature of light, the interaction of light with the desired sample, the characteristics of modern optical microscopy, the characteristics of modern electro-optical sensors (specifically, CCD cameras), and use of appropriate algorithms for the restoration, segmentation, and analysis of digital images [74]. Digital image processing greatly increases the process of extracting information about the sample from a microscope image. Consequently, digital imaging is progressively becoming an essential part of microscopy. Digital image processing can be used to extract quantitative information about the sample from a microscope image, and it can transform an image so that a displayed version is much more informative than it would otherwise be [56].

5.2 The four kinds of digital microscopy images

Through the eyepieces of a microscope, we can't see the original object, rather its image. In digital microscopy, images pass through different forms, in both analog and digital form. In fact, four kinds of distinct images could be captured at any one time, each of which is a

representation of the sample that lies beneath the objective lens of the microscope [56]. These four levels of images include optical image, continuous image, digital image and displayed image (see Fig. 5.1).

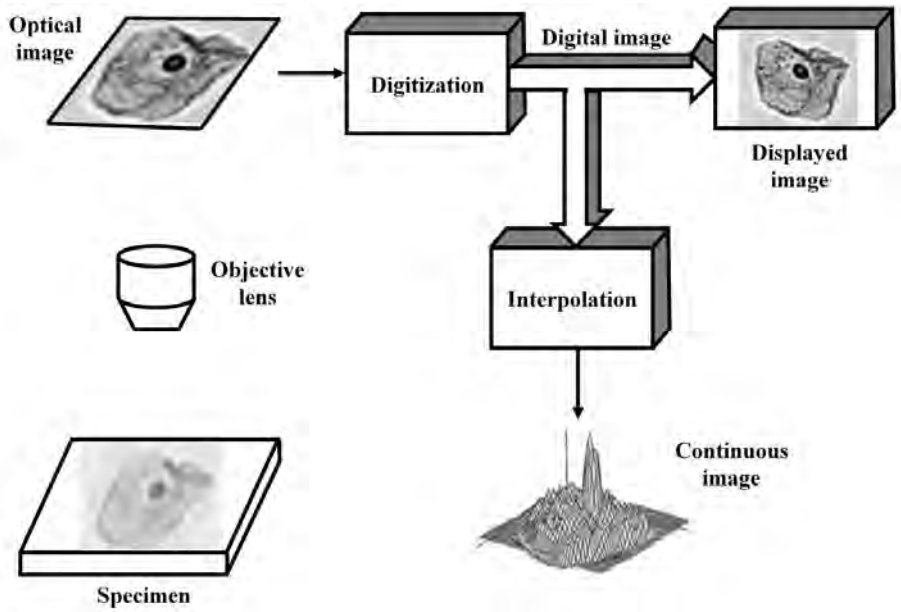

Figure 5.1: *The four kinds of images in digital microscopy. The microscope forms an optical image of the specimen. This is digitized to produce the digital image, which can be displayed and interpolated to form the continuous image [56].*

5.2.1 Optical image

The optical components of microscope, mainly the objective and the ocular lenses act together to create an optical image of the sample on the image sensor, CCD camera array. It is a continuous distribution of light intensities across a two-dimensional surface. Optical image is a two-dimensional (2D) superposition of a three-dimensional (3D) specimen slices. The optical image is limited in resolution, subjected to distortion and noise may be introduced by the imaging process. Hence, although, it contains some information about the sample, it does not fully represent the specimen [56].

5.2.2 Continuous image

Optical images can be represented mathematically as continuous functions of two spatial variables $f(x,y)$ where the coordinate (x,y) denotes spatial position with real valued entries x and y and f denotes a gray value (light intensity) at that spatial position. The physical meaning and the values of f vary according to the individual imaging process. This mathematical (real-valued analytic function of two real variables) representation is known as continuous image.

5.2.3 Digital image

A digital image is formed by the process of digitization. Digitization is performed via a two-step procedure: sampling and quantization (see Fig. 5.2). The continuous optical image, $f(x,y)$ is sampled, commonly on a rectangular grid, small cells of the same shape and size known as pixels (image cells), and the sample values are quantized, density value at each pixel (or sampling point) is assigned to one of the finite set of integers selected as suitable to produce a rectangular array of integers. That is, the now discrete coordinate positions (N,M) are integers, and the light intensity at a given spatial position is represented by a non-negative integer. The digitization process can severely damage an image or even render it useless for analytical or interpretation purposes [56]. Moreover, in order to go back from discrete (digital) to continuous, the process of interpolation is needed. Interpolation enables us to generate an approximation of the continuous image (analytic function), which represents the original optical image.

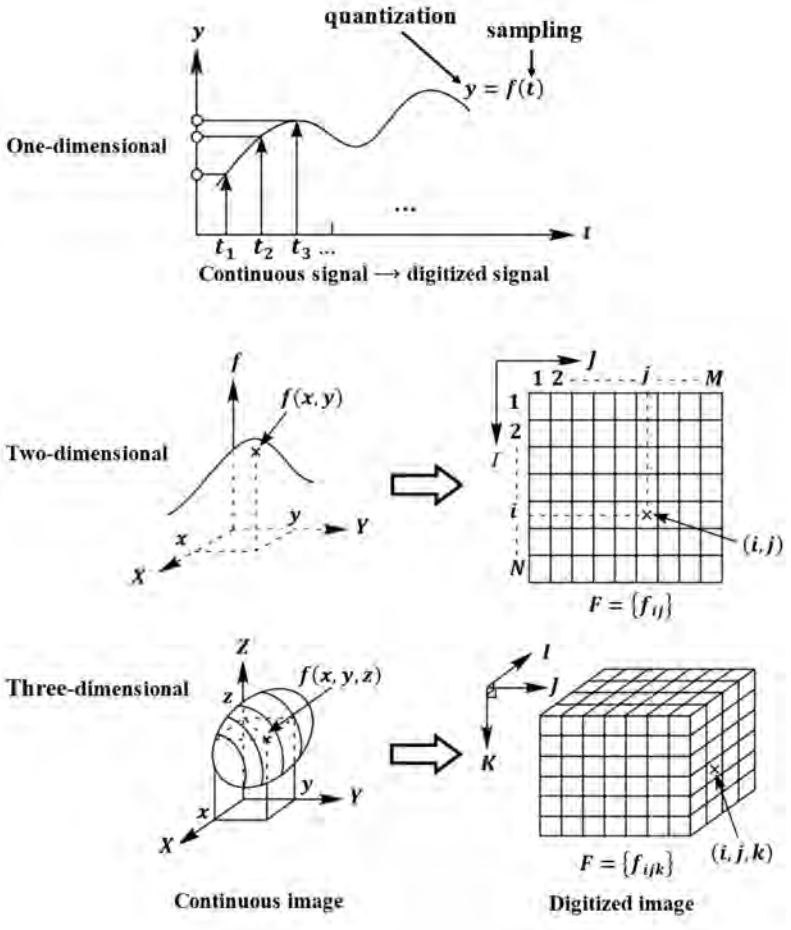

Figure 5.2: *Digitization of signals and images [76].*

5.2.4 Displayed image

Human eyes can not view or interpret an image that exists in digital form. Therefore, the digital image must be transformed back into optical form before it can be seen. In order to display an image on a screen, it requires interpolation, but that is implemented on a hardware. The display spot (pixel) is controlled by the digital image and acts as the interpolation function that creates a continuous visible image on the screen. The display hardware must be able to interpolate the digital image in such a way as to preserve the information of interest [56]. Finally, we visualize the specimen digital image on a display.

5.3 Image formation in microscopy

Image formation in microscopy can be viewed as transformation of input distribution into an output distribution [77]. Hence, a simple lens may be viewed as a system that transforms a spatial distribution of light in the object plane to a distribution in image plane. Whatever the specific physical nature of the input and output distributions is (as depicted in Fig. 5.3), the concept of a mapping between an input distribution (the thing that is to be investigated, seen or visualized) and an output distribution is valid [78].

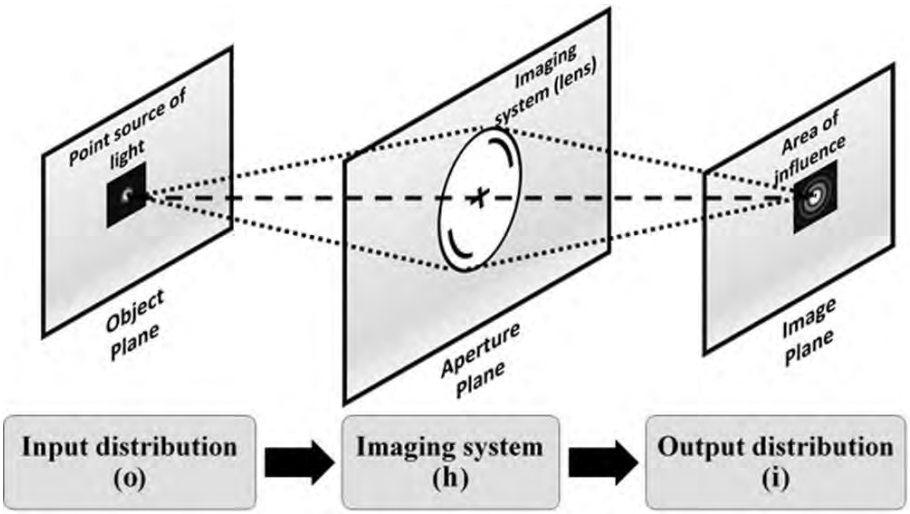

Figure 5.3: *An overview of the image formation by an optical system.*

5.4 Mathematics of image formation

Optical image formation can be formalized as a mathematical model comprising a functional representation of the scene (the object function o) and that of the optical system characterization (the point spread function (PSF), h). Additionally, the image will contain additive noise n.

These are essentially combined as follows to form an image [78]:

$$\begin{aligned} Image &= Object function * PSF + noise \\ i &= o * h + n. \end{aligned} \tag{5.1}$$

PSF is the image of a point light source from the specimen projected by the objective of the microscope onto the image plane and is represented by the Airy disk pattern. It is a characteristic of the imaging instrument (i.e. microscope) and is a deterministic function (that operates in the presence of noise).

Object function this describes the object (or scene) that is being imaged (its surface or internal structure) and the way light is reflected from that structure to the imaging instrument.

Noise is a nondeterministic function which is a consequence of all the unwanted external disturbances that occur during the recording of the image data. Since, it is stochastic function, it is often described in terms of some statistical noise distribution (e.g. Gaussian).

Convolution operator * A mathematical operation which 'smears' (i.e. convolves) one function with another, PSF and object in our case.

5.4.1 Linear imaging systems

Although, majority of real-world imaging systems are nonlinear, they may be well approximated as linear systems [77]. In addition, linear systems are well-understood. However, non-linear theory is still developing and difficult to understand, and deviations from strict linearity are often best handled in practice by approximation techniques which exploit the better understood linear methods [78].

Let $f_1(x,y)$ and $f_2(x,y)$ be two input images and consider an image acquisition system described by the operator $H\{\cdot\}$ and $I(x,y)$ is the output image formed when H is applied on the linear combination of f_1 and f_2. Then H is linear if

$$I = H\{af_1 + bf_2\} = aH\{f_1\} + bH\{f_2\} \tag{5.2}$$

for any two scalars a and b. Equation (5.2) implies that applying the linear operator to a weighted sum of two inputs produces the same result as first applying the operator to the inputs separately and then summing the weighted outputs. Linearity concept is illustrated in Fig. 5.4. The first row of Fig. 5.4 shows the two input distributions, their sum and then the result of applying the linear operator (a blur) to the sum. The second row shows the result of first

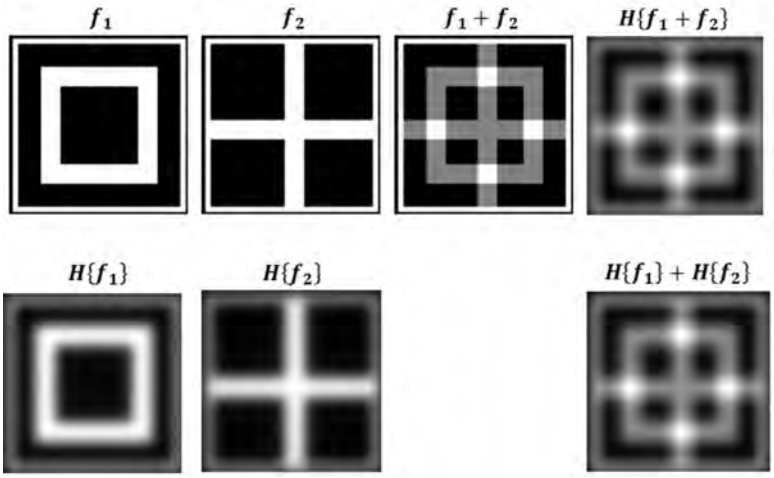

Figure 5.4: *Demonstrating the action of a linear operator H. Applying the operator (a blur in this case) to the inputs and then linearly combining the results produces the same result as linearly combining them and then applying the operator.*

applying the operator to the individual distributions and then the result of summing them. In each case the final result is the same. The operator applied is a convolution with ideal noise free point spread blur function (discussed in Sec. 5.4.3).

5.4.2 Linear superposition integral

In an optical imaging system, each and every point in the input distribution (specimen) contribute to the output image (see Fig. 5.5). Hence, if the system is linear, the contributions to the final output should combine linearly. For an optical imaging system with a 2D input

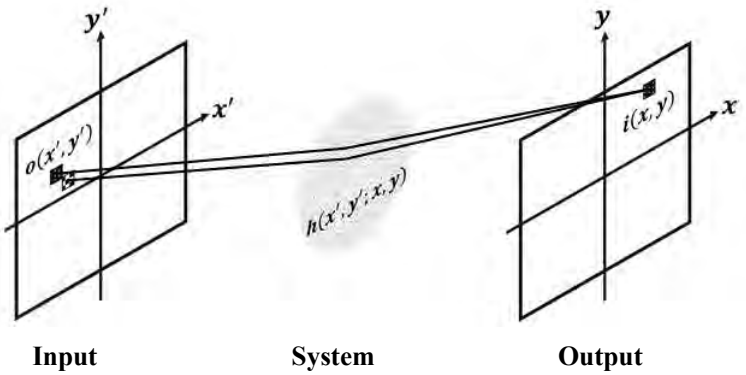

Figure 5.5: *The linear superposition principle. Each point in the output is given by a weighted sum (integral) of all input points [78].*

function $o(x',y')$ in an input domain (x',y') and the response of the system to the input be $i(x,y)$, then the linear image formation is described by the integral operator which is called the linear superposition integral [78]:

$$i(x,y) = \iint o(x',y')h(x',y';x,y)dx'dy' \tag{5.3}$$

where h is a filter. From Eq.(5.3), it is vivid that the behavior of the output image is determined by the filter function, h. In an optical imaging the filter function is referred as PSF. This function describes influence made by each infinitesimal point in the input distribution to each infinitesimal point in the resulting output distribution. Hence, it is a function of four variables $(x,y;x',y')$.

5.4.3 Point-spread function

The PSF of a system is defined as the response of the image system to an input point object (point source) consisting of a very small intensity point [78]. In the context of optical imaging, PSF is response of a focused optical system to an impulse (point light source). In the limit that the point becomes infinitesimal in size, it can be represented as an input function, Dirac delta function,

$$f(x',y') = \delta(x'-x_0,y'-y_0) = \begin{cases} \infty, & x'=x_0,\ y'=y_0 \\ 0, & otherwise \end{cases} \tag{5.4}$$

Hence, for a linear system, we can substitute this into the linear superposition integral, Eq.(5.3), to give

$$i(x,y) = \iint \delta(x'-x_0,y'-y_0)h(x',y';x,y)dx'dy' \tag{5.5}$$

Now, applying the sifting theorem

$$\int_{-\infty}^{\infty}\int_{-\infty}^{\infty} f(x,y)\delta(x-x_0,y-y_0)dxdy = f(x_0,y_0), \tag{5.6}$$

we get,

$$i(x,y) = h(x,y,x_0,y_0). \tag{5.7}$$

The filtering function in the superposition integral $h(x',y';x,y)$ is termed the PSF because it measures the spread in output intensity response due to an infinitely sharp input point light source. Moreover, the PSF describes how each point at the input will look like at the output. Therefore, for a linear optical imaging system (in the absence of noise) the output image is the combination of the PSF responses. Consequently, the PSF determines the output image characteristics of an optical imaging system. The effect of PSF in an optical imaging system is shown in Fig. 5.6.

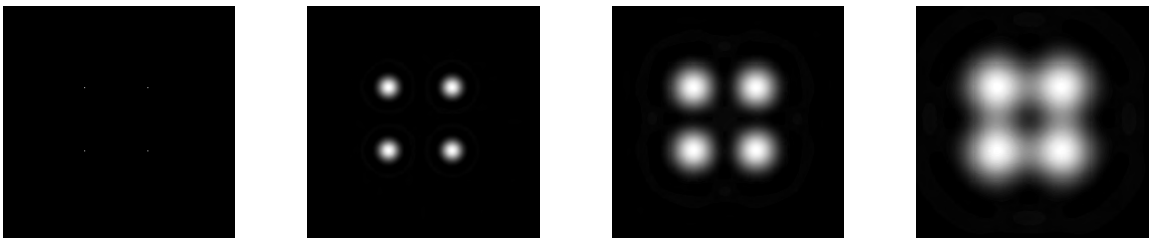

(a) *(b)* *(c)* *(d)*

Figure 5.6: *The effect of PSF in optical imaging system. As the PSF becomes broader and broader, the initial point input distribution become wider and finally starts to overlap.*

5.4.4 Linear shift-invariant systems and the convolution integral

In optical imaging, another important characteristic of filters is shift invariance. A filter/system is shift invariant provided if $y(n)$ is the response of the system to $x(n)$, then the system with the shifted input $x(n-k)$ gives a shifted output $y(n-k)$ [77]. This implies that co-existent response of the output variable to a given value of the input variable does not depend on where the input occurs. Thus, the combined properties of linearity and shift invariance gives rise to linear shift-invariant (LSI) systems [77]. For an LSI system, the operation of the filter on the image is described by convolution, denoted by $*$; an output $i(x,y)$ is said to be given by the convolution of the input $f(x,y)$ with the PSF, $h(x,y)$. Thus, for 1D function,

$$i(x) = \int f(x')h(x-x')dx'. \tag{5.8}$$

For 2D shift-invariant imaging systems, the linear superposition integral in Eq. (5.3) reduces to a simpler and very important form of convolution integral:

$$i(x,y) = \iint f(x',y')h(x-x',y-y')dx'dy'. \tag{5.9}$$

5.5 Digital microscope image conversion

A digital microscopy image acquired using a CCD camera can be represented in different intensity levels, as full color, gray scale or black and white image.

5.5.1 Black and white image

Binary (black and white) objects are logical arrays of 0s and 1s [79]. Typically, they are represented such that pixels belonging to the object take a value of "1" and the remaining pixels are "0".

5.5.2 Gray scale image

Gray level of an image is a range of shades of gray without apparent color (see Fig. 5.7). The darkest possible shade is black, which is the total absence of transmitted or reflected light. On the other hand, the lightest possible shade is white, the total transmission or reflection of all visible wavelength. The rest are intermediate shades of gray. Gray level image data matrix can have integer values in the range [0, 255] or [0,65535] for 8-bit and 16-bit depth, respectively [79].

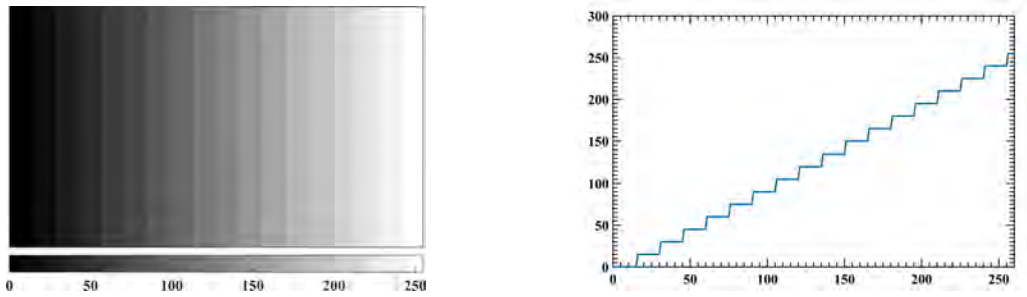

(a) *(b)*

Figure 5.7: *Gray scale image (a) Shades of 18 gray shade levels, and (b) Gray shade intensity profile.*

5.5.3 Color image

A color image can be considered as a stack of three gray-scale images. These three images forming a color image are known as red, green and blue component as shown in Fig. 5.8. Hence, color (RGB) images are considered as a special case of multichannel (3 channels with 8 bits each) images [79,80]. Color image processing is beyond the scope of this thesis and readers may consult the related materials available in many literatures to learn more on the subject [81–83]. Gray scale images are represented in the RGB color space with equal intensity levels of the three primary colors (red, green, and blue) equal to the gray values. Fig. 5.9 presents a pseudo-color, gray scale as well as black and white microscopic images of microbubbles.

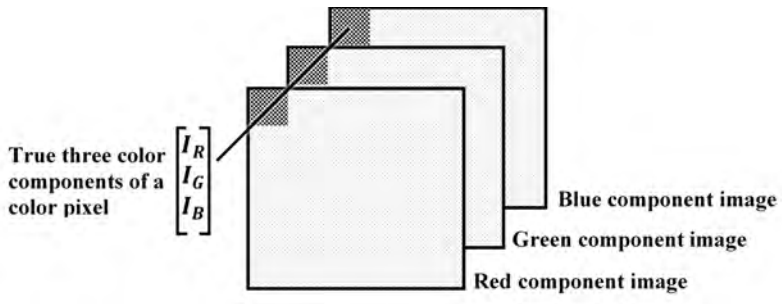

Figure 5.8: *The three color image components (Red, Green, Blue).*

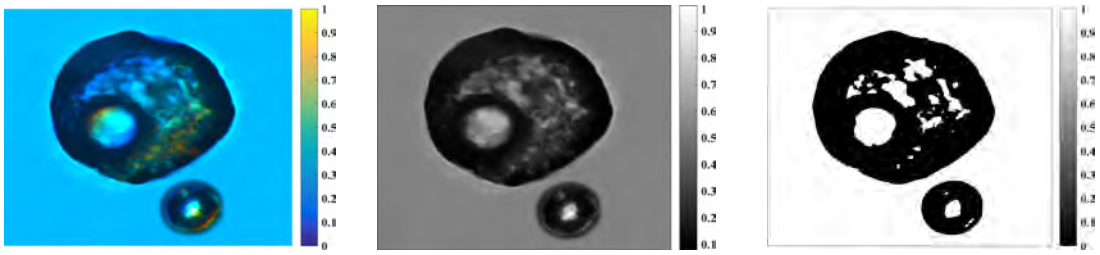

(a) *(b)* *(c)*

Figure 5.9: *Microscope images of microbubble. (a) Pseudo-color, (b) Gray scale, and (c) Black and white.*

5.6 Image segmentation

Image segmentation is critical step in digital image analysis. It is the division of an image into disjoint (nonoverlapping) regions or categories, which correspond to different objects or parts of objects [56]. Every pixel in an image is allocated to one of a number of these categories. A good segmentation is typically one in which: neighboring pixels which are in different categories have dissimilar values and pixels in the same category have similar greyscale of multivariate values and form a connected region. Once isolated, these objects can be measured. There are three general approaches to segmentation, termed thresholding, edge-based methods [84–87] and region-based methods [88–90]. However, in this thesis only segmentation based on thresholding will be discussed.

5.6.1 Thresholding

Thresholding is computationally simple and most commonly used method of segmentation. It is used to discriminate between the objects of interest (also known as the foreground) and the background on which they lay. The output is either the label “object” or “background,” which can be represented as a Boolean variable. Given a single thresholding value, T, in general, a gray-level thresholding operation can be expressed as [56],

$$g(x,y) = \begin{cases} F, & i(x,y) \leq T \\ B, & i(x,y) > T \end{cases}. \tag{5.10}$$

where $i(x,y)$ is the original image, $g(x,y)$ is the thresholded image, and F and B correspond to the foreground and background designated gray-level values respectively. Hence, all pixels above the threshold value are assigned to the background and all pixels below the threshold are assigned to the foreground. In general, the choice of the threshold, T, has considerable effect

on the boundary position and overall size of segmented objects (see Fig. 5.10).

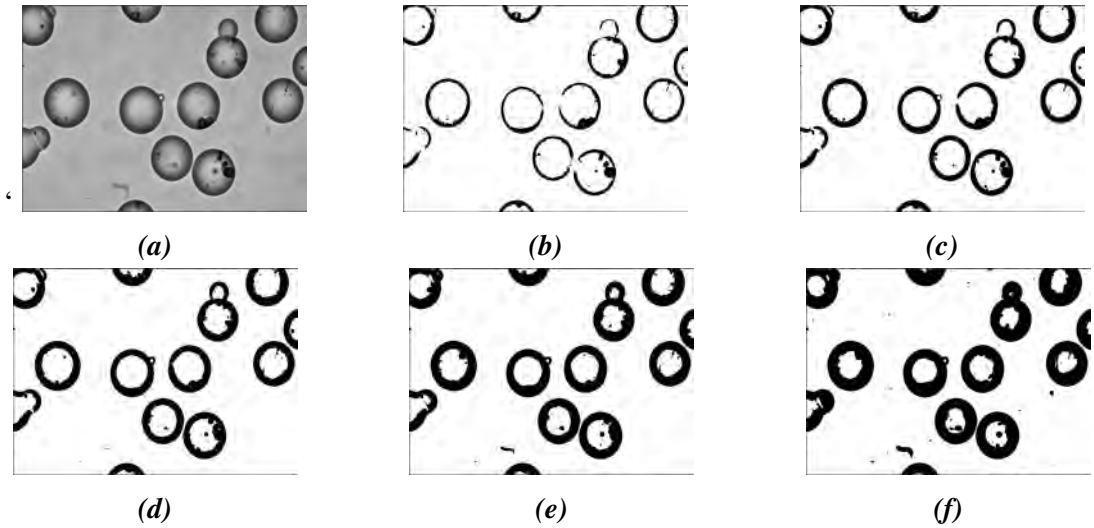

Figure 5.10: *Five segmentations of a microbubble image assuming normalized gray values between 0 and 1, obtained using manually-selected thresholds of (a) Original gray scale image, (b) $T = 0.3$, (c) $T = 0.35$, (d) $T = 0.4$, (e)$T = 0.45$, and (f) $T = 0.5$.*

5.7 Object quantification

Object quantification has various applications in different areas. For instance, it can be used to measure object structure or morphology defining properties, such as: area, perimeter, shape, etc. It can also be used to differentiate between objects by measuring and comparing their properties [79, 91, 92]. In order to measure an object, it must be segmented and pass through morphological post processing. This will enable to define objects from which measurements can be carried out [73]. The extracted objects can be treated either as binary objects or as gray-level objects.

Object measurements can be broadly classified as (1) geometric measures, (2) ones based on the histogram of the object, and (3) those based on the intensity of the object [73]. Geometric measures, including those that quantify object structures, can be computed for both binary and grayscale objects. In contrast, histogram and intensity-based measures are applicable to grayscale objects. Another category of measures, which are distance based, can be used for computing the distance between objects or between two or more components of objects [73].

5.7.1 Quantification of binary objects

A binary object can be described in terms of its size, shape, or distance to other objects. One common measure is, for example, area..

Area Consider the function $I_n(i,j)$ described for an object label map of an $N \times M$ image, then

$$I_n(i,j) = \begin{cases} 1, & \text{if } I(i,j) = n^{th} \text{ object number} \\ 0, & \text{Otherwise} \end{cases} \tag{5.11}$$

The area in pixels of the n^{th} object is then given by [56],

$$A_n = \sum_{i=0}^{N-1} \sum_{j=0}^{M-1} I_n(i,j). \tag{5.12}$$

Similarly other measures could be computed on binary images.

5.7.2 Quantification of microbubble objects

In a previous study, experiments on 583 optical observations of freely flowing, oscillating, individual microbubbles from an experimental ultrasound contrast agent (UCA) were analyzed [2]. In this study, images of microbbubles in an ultrasound field with a 500-kHz frequency at acoustic amplitudes ranging from 0.06 MPa to 0.85 MPa were recorded using high frame rate camera operating at 3 MHz. Furthermore, the study compared true bubble radius to actual bubble radius and it was observed that object size measurement for one-dimensional objects and two-dimensional objects (bubbles) is affected by the optical system point spread function (Fig. 5.11), visual focus (see Fig. 5.12) and segmentation technique used (see Fig. 5.13). The study concluded that there is no systematic error when measuring the size of microbubbles with diameters of 0.8μm or higher while pronounced errors are observed for smaller diameters (see Fig. 5.14).

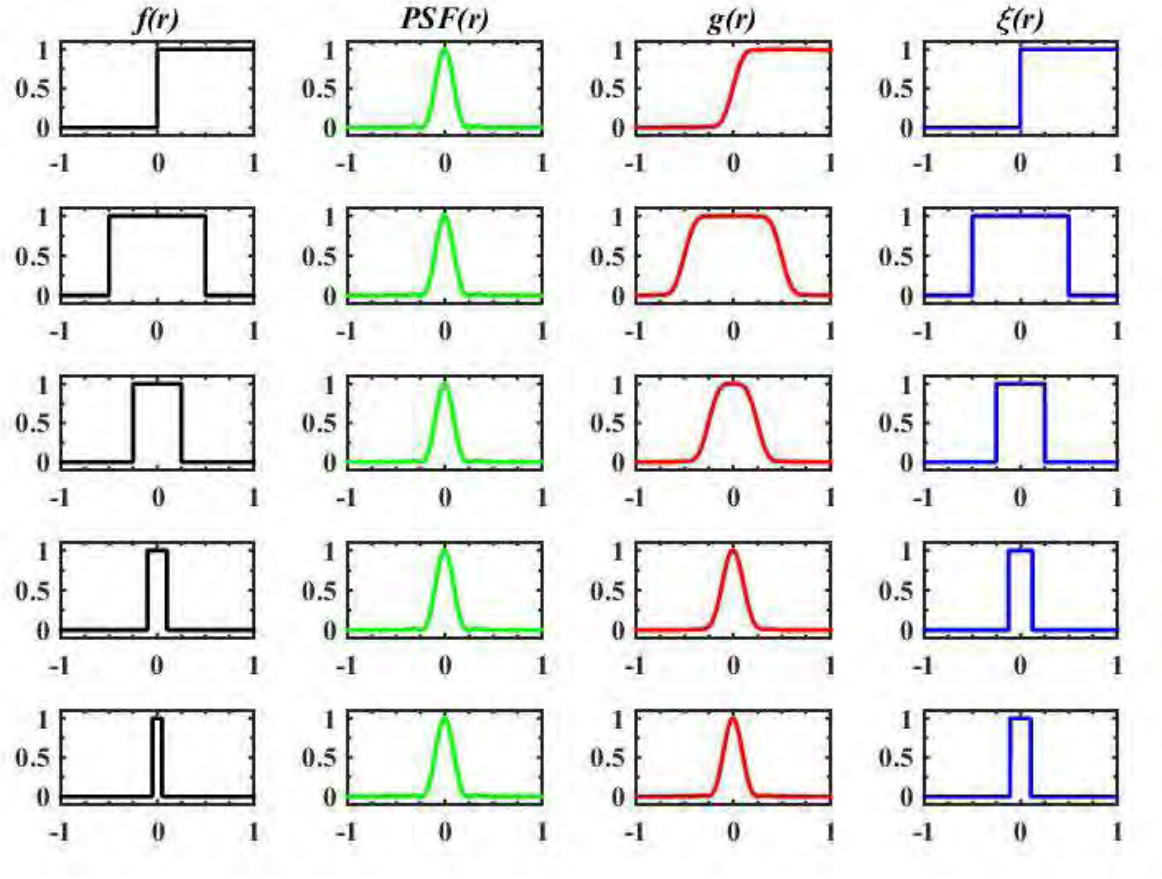

Figure 5.11: *One-dimensional, differently sized objects f, convolved with the PSF, resulting in optical images g. Segmented objects ξ were obtained after applying the threshold $\theta = 0.5$. Objects diameter before segmentation (∞, $1.0\mu m$, $0.50\mu m$, $0.20\mu m$, $0.10\mu m$) and after segmentation (∞, $1.0\mu m$, $0.50\mu m$, $0.24\mu m$, $0.22\mu m$) [2].*

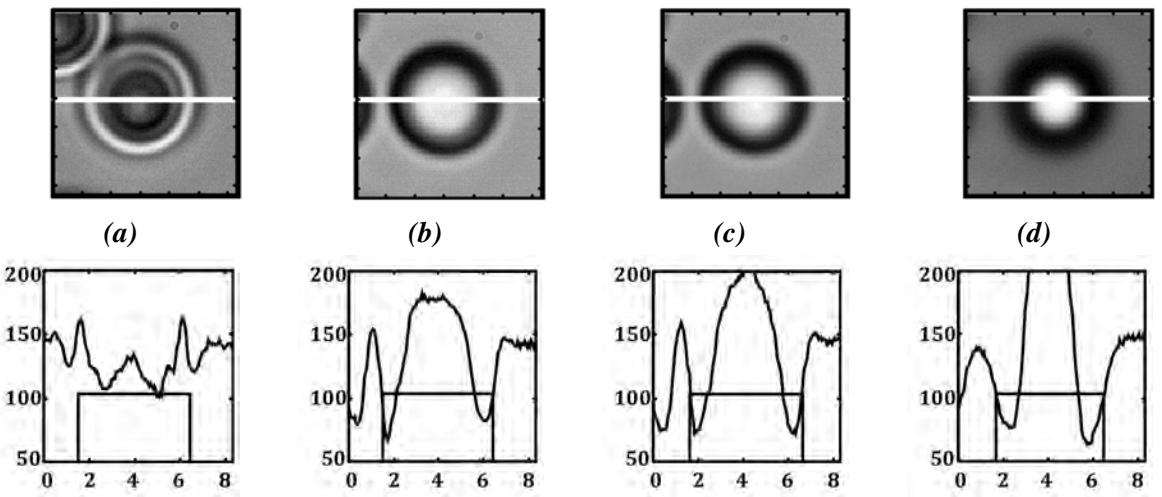

Figure 5.12: *Intensity cross-sections of a $5\mu m$ glass calibration particle, $4\mu m$ proximal to focus (a), $2\mu m$ proximal to focus (b), in focus (c), and $2\mu m$ distal to focus (d) [2].*

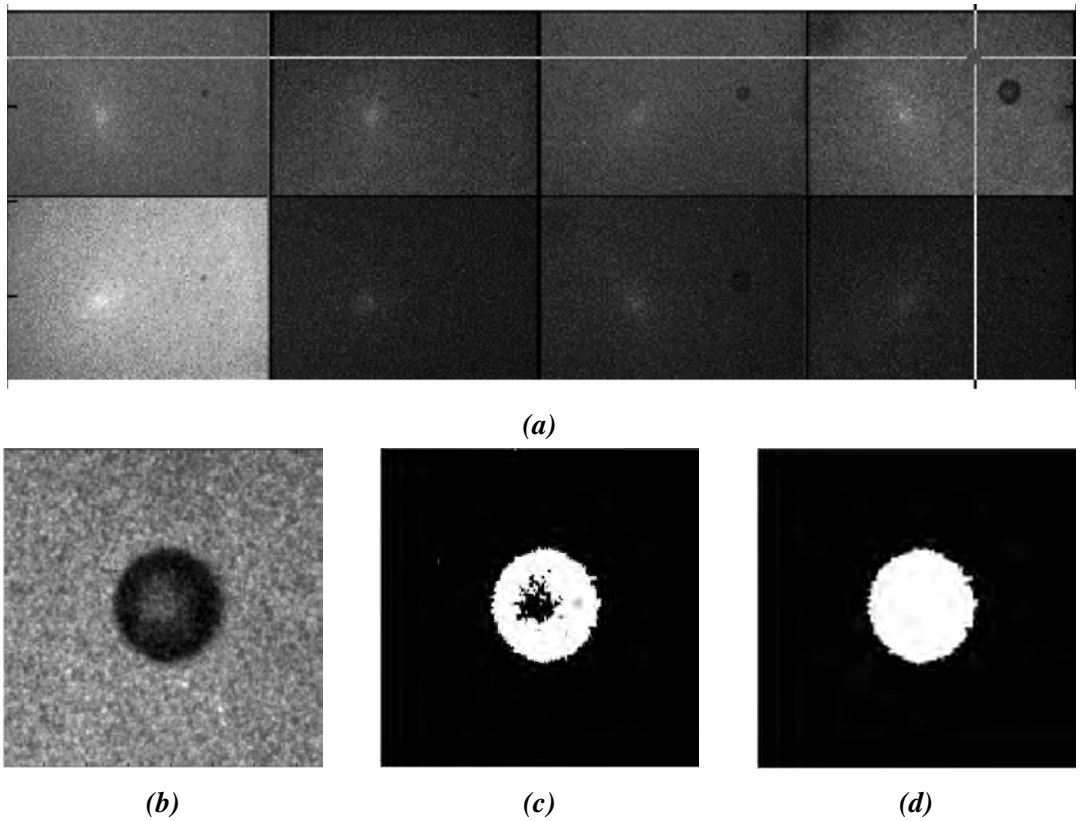

(a)

(b) *(c)* *(d)*

Figure 5.13: *Selection of region of interest, optical observation is done by recording eight two-dimensional frames at 100 MHz. The first frame was taken a few microseconds before ultrasound waves reached the contrast agent. The other seven frames were taken during ultrasound insonification, with 330 ns interframe time (a) and Semi-automated segmentation (b), binary segmented image (c), segmented object (d) [2].*

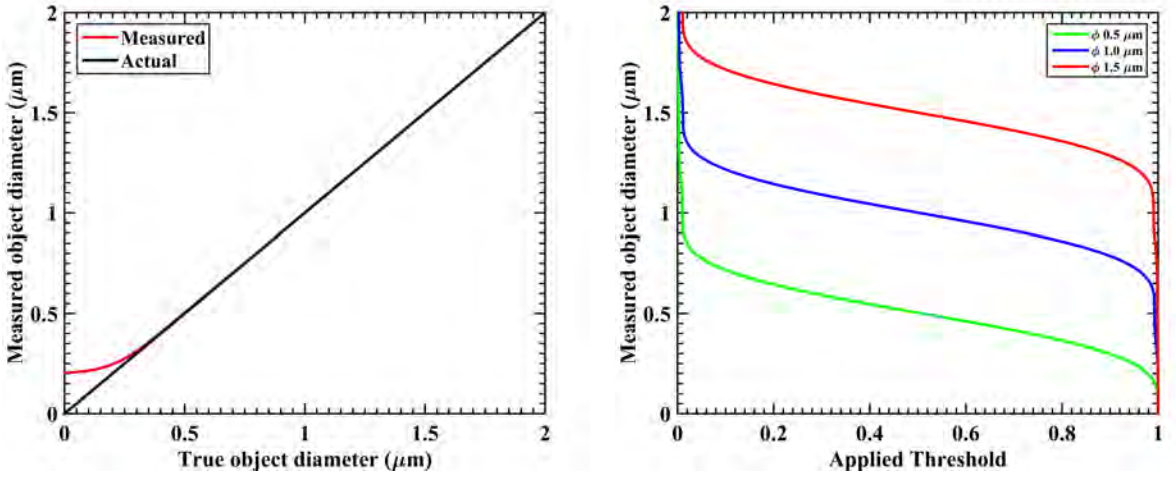

(a) *(b)*

Figure 5.14: *Object size comparison of: (a) Measured object diameter (ζ) versus true object diameter (τ) after segmentation using the threshold $\theta = 0.5$, and (b) Measured object diameter (ζ) as a function of applied threshold (θ) for three different object diameters [2].*

CHAPTER 6

Methodology

6.1 Modeling 3D artificial objects

In order to mimic real microbubbles, the 3D object functions are chosen to be spheres with radius r, represented as a stack/layers of white rings on a black background images (or black rings with white background). Ring thickness (R_t) is taken to be 200 nm, assuming a polymer encapsulating layer. The white ring objects with black background were created using the following function in 3D:

$$o(x,y,z) = \begin{cases} 1, & (x^2+y^2+z^2) \leq r^2, \ \ (x^2+y^2+z^2) \geq (r-R_t)^2 \\ 0, & \textit{Otherwise} \end{cases} \tag{6.1}$$

Similarly the black ring with white background artificial images could be generated easily.

6.2 Modeling 3D microscope images

Extending two dimensional optical image formation of an ideal (noise-free) microscope to three dimensional, the 3D image formation can be expressed in xyz-coordinates by [93]:

$$i(x,y,z) = \iiint o(x',y',z')h(x-x',y-y',z-z')dx'dy'dz'. \tag{6.2}$$

where i is the image, o is the object imaged, and h is the point spread function of the optical imaging system. Knowing that a three-dimensional object under a microscope can be considered as a stack of thin two-dimensional layers, the image of an object in the focal plane can be computed with the weighed sum of each contributing layer:

$$i(x,y,z) = \sum_z \left(w(z) \iint o(x',y')h(x-x',y-y')dx'dy' \right) \tag{6.3}$$

where w is a weighing function. Moreover, as the microscope is ideal, we can take circularly symmetric point spread function in the focal plane [2]:

$$h(r) = \left(2\frac{J_1(ar)}{ar} \right)^2 \tag{6.4}$$

where $J_1$is the first-order Bessel function of the first kind, $r = \sqrt{x^2 + y^2}$, and

$$a = \frac{2\pi NA}{\lambda}, \tag{6.5}$$

in which λ is the wavelength of the light, and NA is the numerical aperture of the objective lens.

The weighing function w has a form similar to the intensity field from a circular piston [29]:

$$w(z) \propto \left| \sin\left(\frac{\pi R^2}{2\lambda z}\right) \right|, \tag{6.6}$$

where R is the radius of the objective lens. Moreover, the depth of focus Δz is taken to be [74]:

$$\Delta z = \frac{\lambda}{4n\left[1 - \sqrt{1 - \left(\frac{NA}{n}\right)^2}\right]}. \tag{6.7}$$

where n is a refractive index.

To generate artificial optical images, the two-dimensional point spread function in Eq. (6.4) was computed, using $NA = 1.25$ and $\lambda = 500$ nm. Several layers were taken depending on the sphere object size and the object was sliced with depth of focus $\Delta z = 133$ nm from Eq. (6.7). In addition, $R = 1.75$ mm and 1.75 mm $\leq z \leq$ 1.76 mm were used to compute the weighing functions shown in Eq. (6.6). After convolution of the object with the respective weighed point spread function, the resulting two-dimensional images were stacked and normalized, according to Eq. (6.3).

6.3 Image segmentation

Once an optical image of a microbubble is recorded, the process of size measurement was done in an automated fashion. To discriminate dark objects from a light background and vise-versa, a gray-level window slicing has been used as follows:

$$\xi(x,y) = \begin{cases} 1, & o(x,y) \leq T \\ 0, & o(x,y) > T \end{cases}, \tag{6.8}$$

where ξ is the segmented image and T is the threshold gray-level. Image segmentation was done with a threshold $T = 0.5$, knowing that the artificial images represent perfect black-and-white images [3].

6.4 Object size quantification

For a segmented object (see Fig. 6.1),

$$I(i,j) = \begin{cases} 1, & \text{if } I(i,j) \text{ is part of the object} \\ 0, & \text{Otherwise} \end{cases} \tag{6.9}$$

The bubble on pixel region $A_{N\times M}$ is measured by summation of all points in the segmented area,

$$A_{N\times M} = \sum_{i=0}^{N-1}\sum_{j=0}^{M-1} I(i,j). \tag{6.10}$$

For a CCD camera image of size $W \times H$, the actual size of each pixel area is computed as:

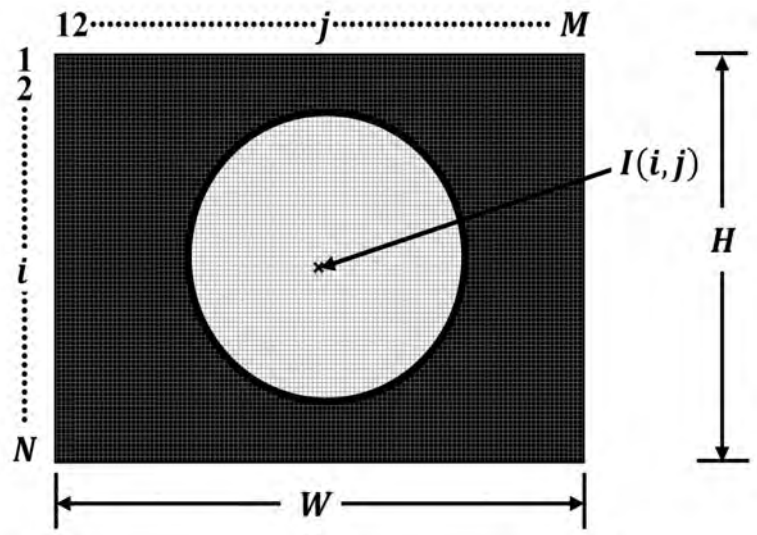

Figure 6.1: *Illustration of object size measurement after segmentation.*

$$P_w = W/M \tag{6.11}$$

$$P_h = H/N \tag{6.12}$$

$$P_a = P_w \times P_h \tag{6.13}$$

where P_w is pixel width and P_h is pixel height while P_a is pixel area.

Now, the segmented actual bubble area becomes,

$$A_b = A_{N\times M} \times P_a, \tag{6.14}$$

yielding the measured bubble radius

$$r_b = \sqrt{\frac{A_b}{\pi}}. \tag{6.15}$$

CHAPTER 7

Result and Discussion

7.1 Introduction

This study set out to investigate and find out whether there is a systematic error in measuring the size of three-dimension (3D) objects like microbubbles from a microscope image using image processing. The results for each step of methodology is presented in this chapter. The results are presented in figure, graph and table form. The results displayed include modeling of artificial 3D objects, 2D slice of the 3D objects, model of the 3D optical imaging system, the final image formed by the 3D optical imaging system, comparison of the true size of imaged 3D artificial object with measured size. Each theme that emerged from the data is discussed, described, and supported with examples of actual data.

7.2 Modeling of 3D artificial objects

In this study, the 3D artificial objects are taken to be hollow spheres as shown in Fig. 7.1. Each sphere objects have a shell thickness of 200 nm assuming a polymer surfacant (shell) and a radius ranging from 0.5 μm to 5 μm, which is a typical size range of microbubbles.

7.3 Modeling 3D optical imaging system

Following the simulation of artificial 3D objects, next step is to model the 3D optical imaging system. This is done by first generating an ideal one dimensional (1D) point spread function (PSF) as shown in Fig. 7.2. The PSF is generated using Eq. 6.4 for the value of refractive index, $n = 1.33$, assuming that the medium between the objective and the specimen is water, numerical aperture of objective lens NA=1.25 and wavelength, $\lambda = 500$ nm.

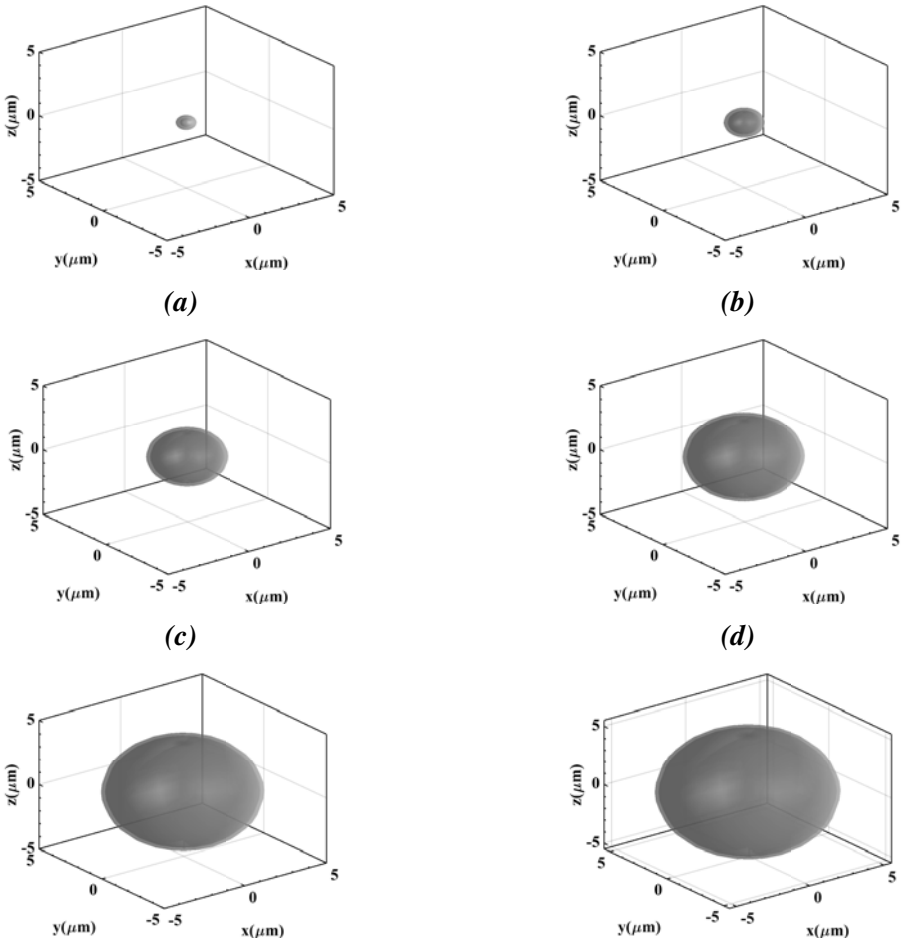

Figure 7.1: *Simulation of 3D objects with radius: (a)* $0.5\mu m$*, (b)* $1\mu m$*, (c)* $2\mu m$ *(d)* $3\mu m$ *(e)* $4\mu m$*, and (f)* $5\mu m$*.*

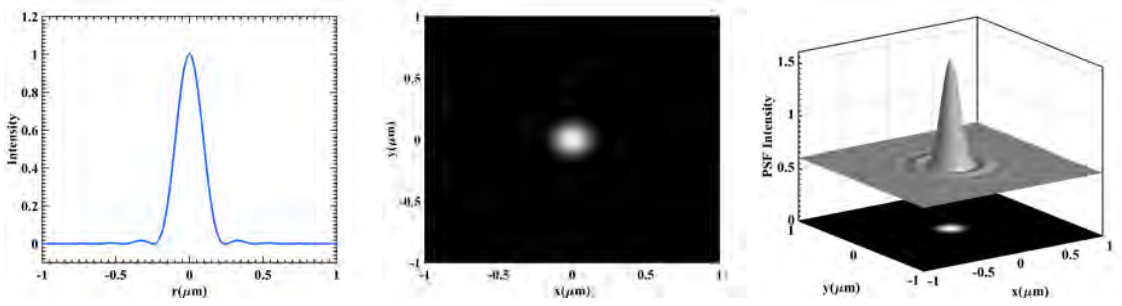

Figure 7.2: *Simulation of ideal PSF in: (a) 1D, (b) 2D, and (c) 3D using parameters* $\lambda = 500nm$*,* $NA = 1.25$ *and* $n = 1.3$*.*

Now 1D PSF is obtained, from this 3D PSF is generated by weighting the 1D PSF. The reason the 1D PSF is weighted is in real microscope the point spread function distribution has higher intensity near the focus and when it is out of focus its intensity fades. This fading in an intensity can be simulated by computing the axial irradiance based on the Eq. 6.6. Taking lens radius, R=1.75mm, $\lambda = 500$nm and axial depth, z in mm depending on the size of the objects, the weighting function is generated (see Fig. 7.3).

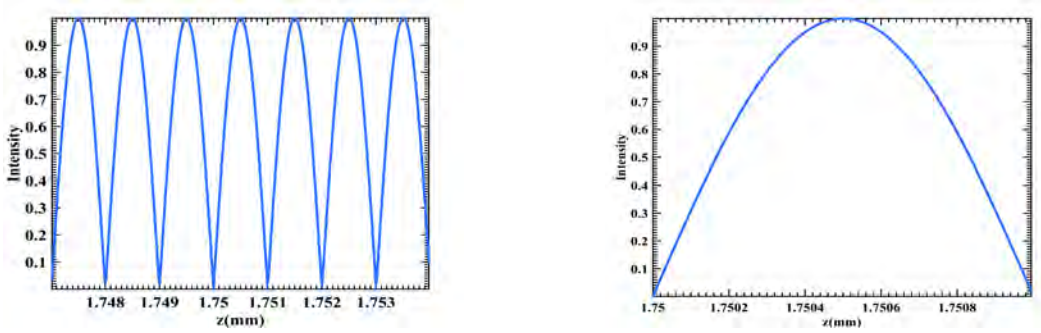

(a) *(b)*

Figure 7.3: *Weighting function profile: (a) Over the focus (*$1.747\ mm \leq z \leq 1.756\ mm$*) and (b) Near the focus for* $\Delta z = 133\ nm$.

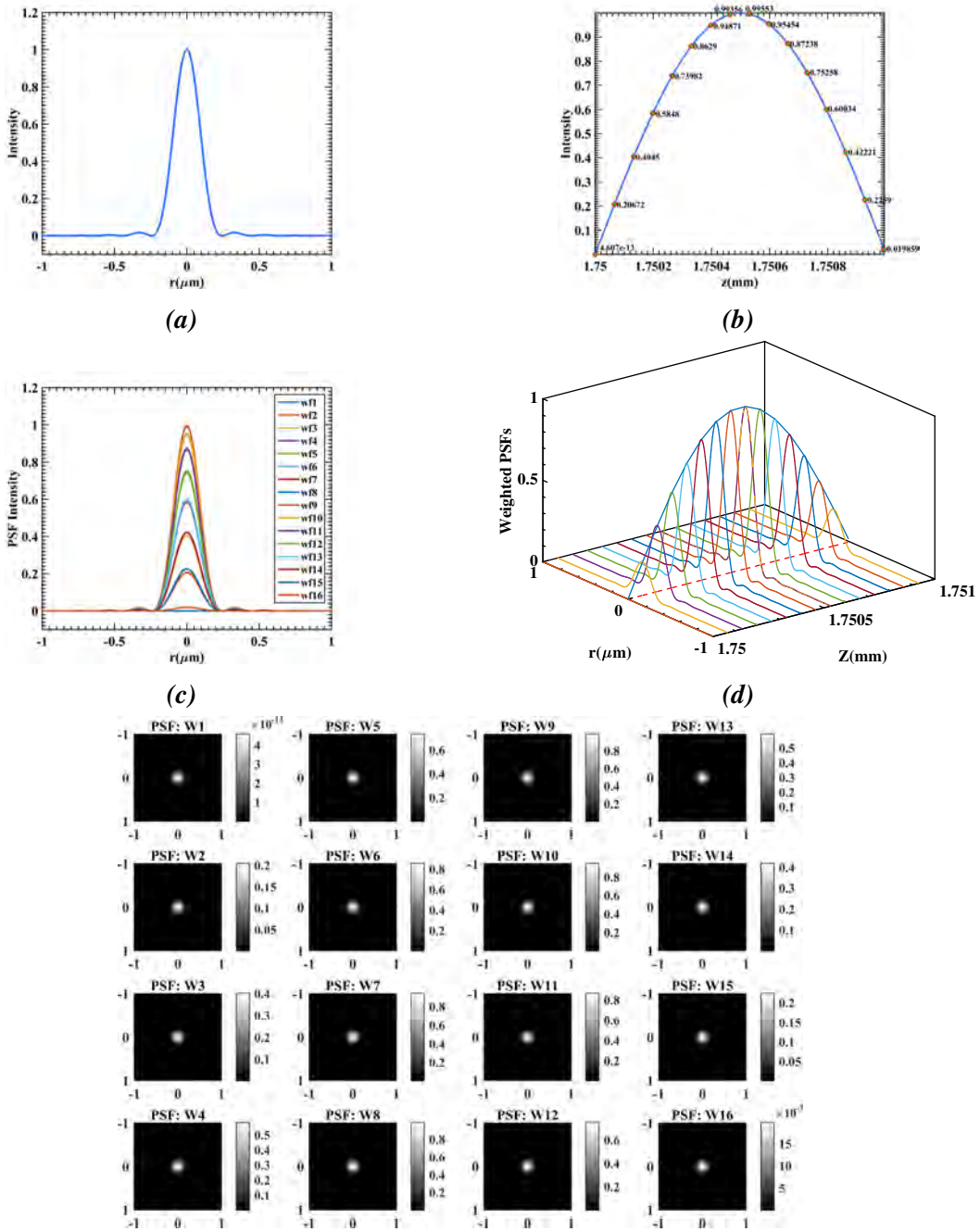

(c) *(d)*

(e)

Figure 7.4: *Simulation of 16 weighted point spread functions. (a) Ideal 1D PSF, (b) 1D weighing function, (c) 1D weighted PSFs, and (d) 2D weighted PSFs.*

7.4 Slicing white ring and black ring objects

A 3D object can be considered as a stack of infinitely thin two-dimensional layers. When 3D objects are imaged through a microscope, the image formed onto the charge coupled device (CCD) element consists of contributions from all layers. Hence, to take into account the contribution of each layer in a 3D objects, each object is sliced based on the optical system depth of focus. The depth of focus is computed based on the formula stated in Eq. 6.7, for the typical values of $n = 1.3$, and $\lambda = 500$ nm and the sliced objects result is depicted in Fig. 7.5.

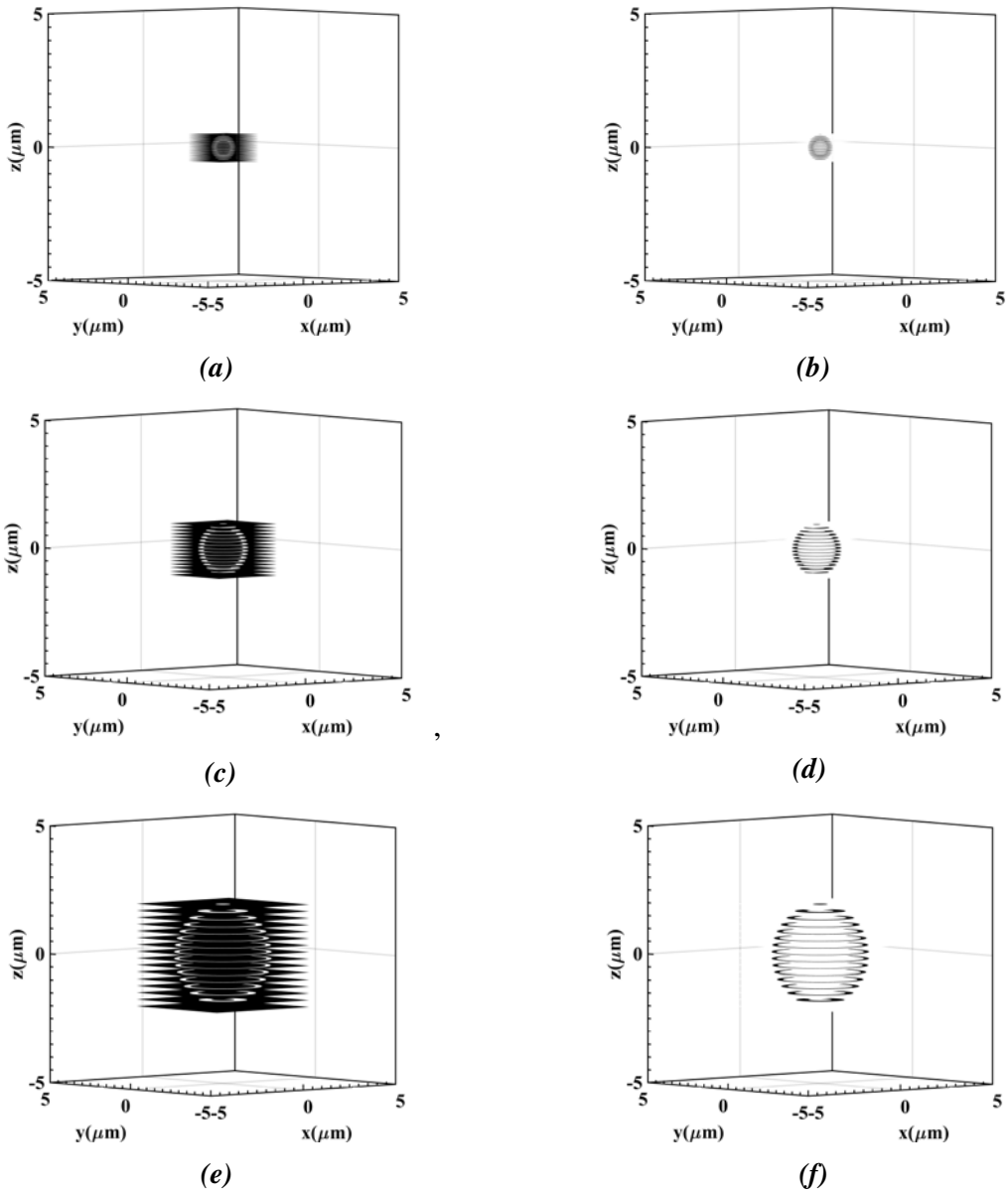

Figure 7.5: *Slices of white ring objects (left column) and black ring objects (right column) with radius and slice depth of: (a, b)* $0.5\mu m$ *and* $0.5 * \Delta z$*, (c, d)* $1\mu m$ *and* $1 * \Delta z$*, and (e, f)* $2\mu m$ *and* $2 * \Delta z$ *(see Appendix A for objects* $r > 2\mu m$*). Note: multiples of* Δz *is used for each object, to visualize same (16) number of slices with out overlapping. However, for the actual size measurement* $\Delta z = 133nm$*.*

7.5 Simulating shift of focus

Microbubbles are often observed through microscope under the influence of an ultrasound and it is likely that they get out of focus. As a result, the imaged captured would be blurred and the size measures would deviate from the actual size measurement. Therefore, measuring the microbubbles size while they are out of focus would help to analyze the effect of defocussing in quantifying bubbles dimension. Consequently, it is possible to predict the actual size of bubbles even though they are imaged out of focus. The simulation of shift of focus for both small objects and large objects is shown in Fig. 7.6 and Fig. 7.7 respectively. It can be seen

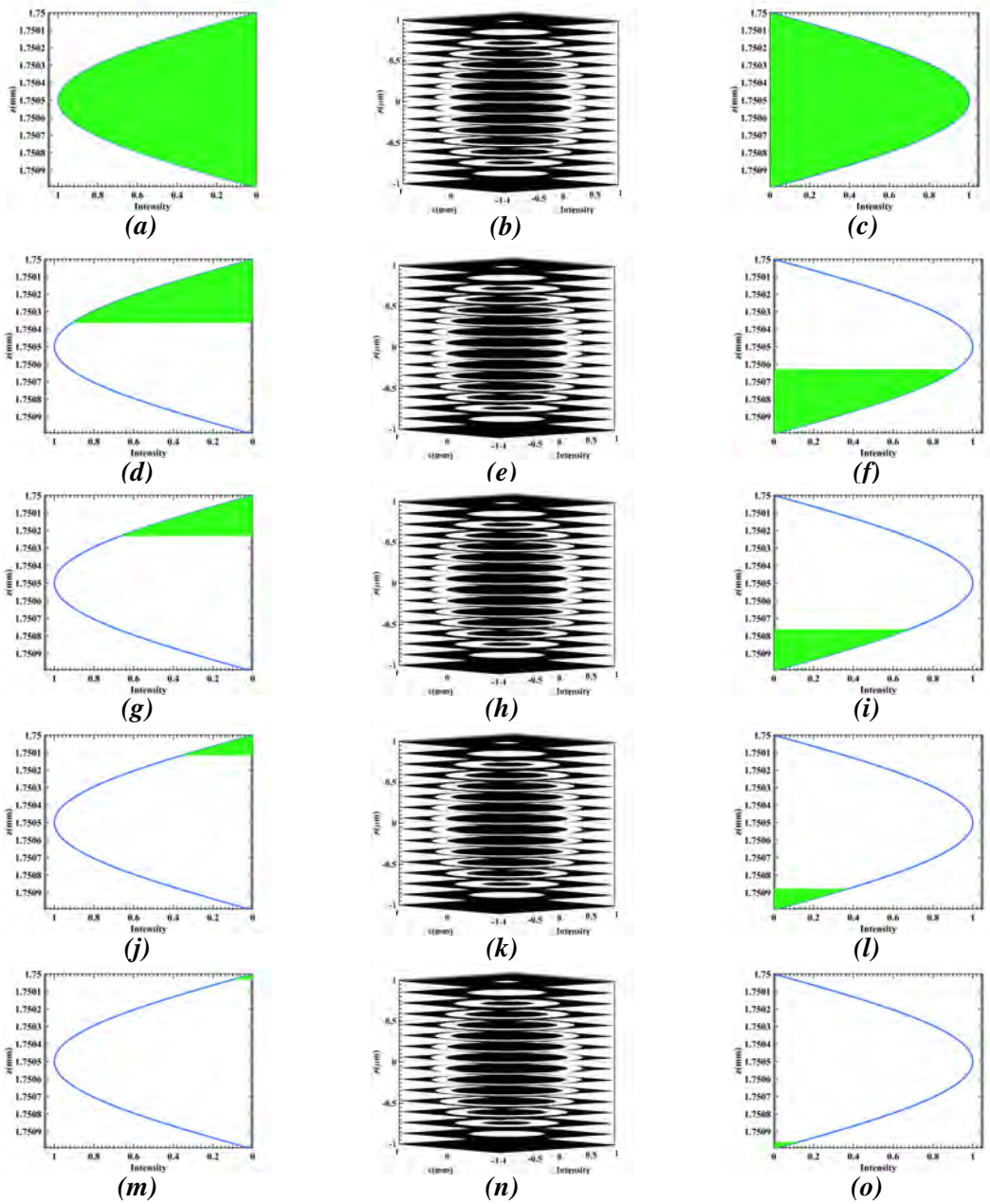

Figure 7.6: *Simulation of shift of focus (green region) for objects of radius $r = 0.5\mu m$. First column is above focus, third column is below focus while the middle column is the 3D object. Going from the second row to the last, the shift is 25%, 50%, 75%, and 90% respectively.*

the figures that small objects interfere with small portion of the light, similarly large objects accordingly. When an object is in focus all slices contribute for the image formation. Hence, they are weighted with their full size in focus (green region). On the other hand, when an object is out of focus it is weighted by the portion of the light where the object is in focus.

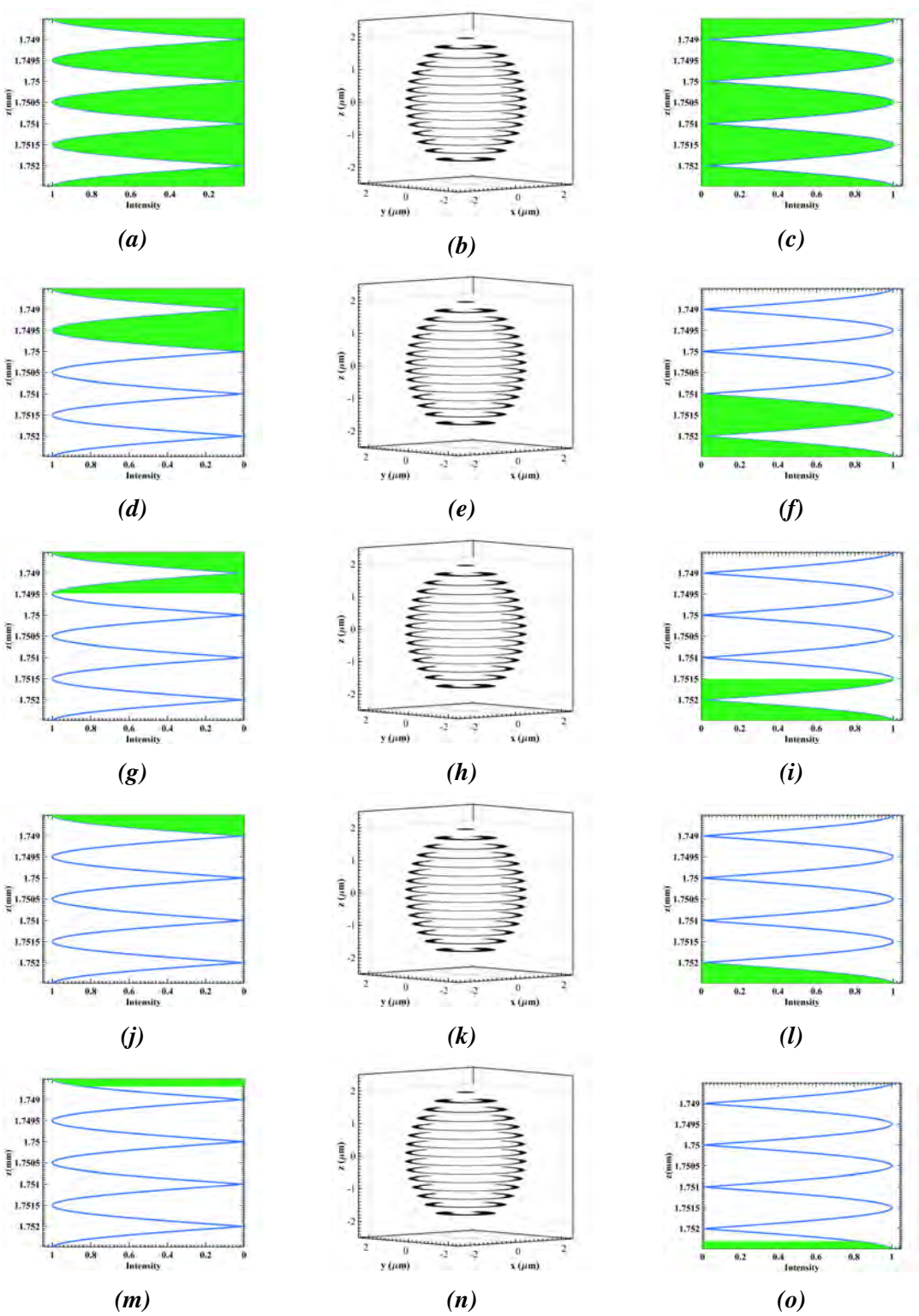

Figure 7.7: *Simulation of shift of focus (green region) for objects of radius $r = 2\mu m$. First column is above focus, third column is below focus while the middle column is the 3D object. Going from the second row to the last, the shift is 25%, 50%, 75%, and 90% respectively.*

7.6 Compute 2D image formation

An optical image of a radially symmetric flat object in focus, observed through a microscope, is expressed by convolution of the PSF of the optical system and the object. Hence, to compute the 2D image formed at the CCD first the 3D object slices, Fig. 7.8 are convolved with the weighted PSFs and the convolution result, Fig. 7.9 shows that near the focus the intensity is higher as seen on the intensity bar. In addition, the blurring effect of PSF when convolved with an object is shown in Fig. 7.10 and Fig.7.12. Second the convolved object slices are stacked and summed up to form a 2D image (see Fig.7.12 and Fig. 7.13) formation of the 3D object.

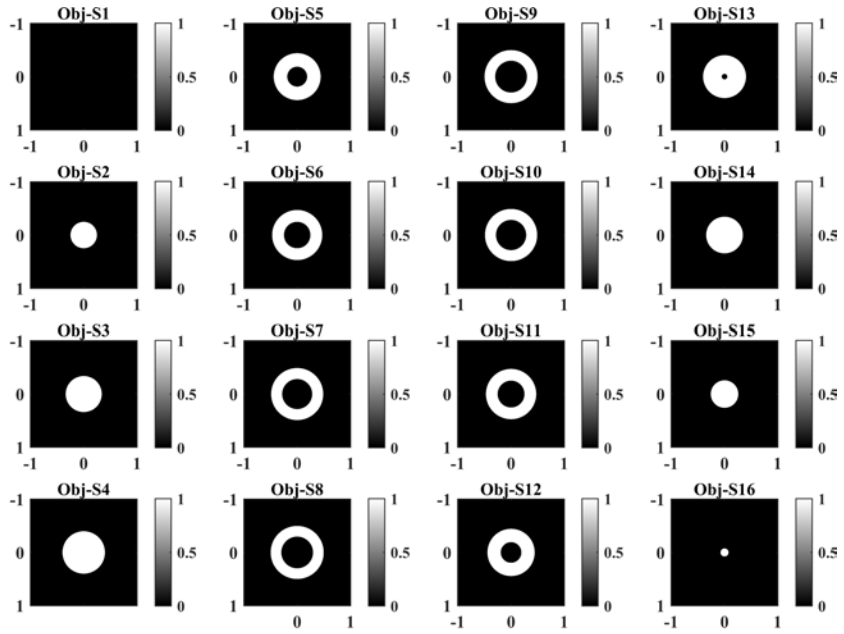

Figure 7.8: *16 2D slice images of 3D object taken with* $0.5 * \Delta z$ *for radius of* $r = 0.5\mu m$.

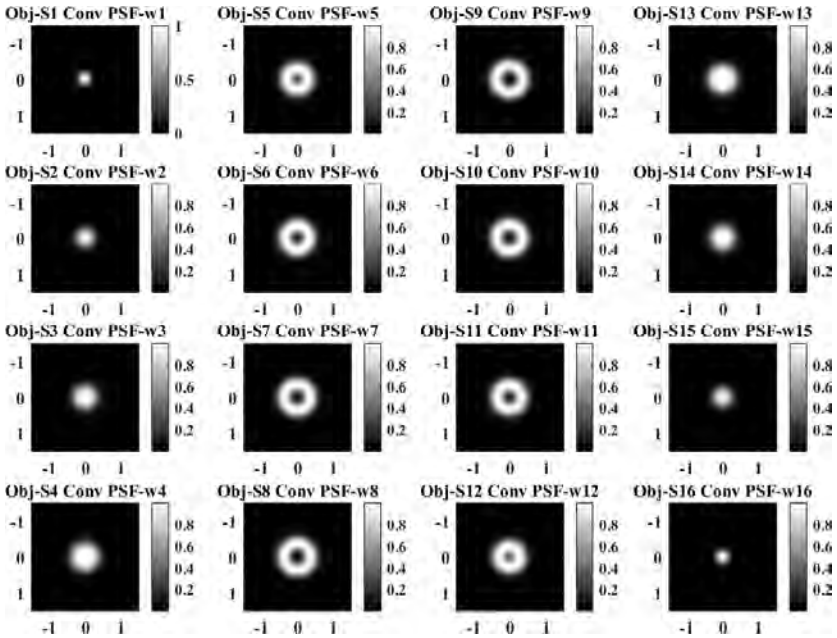

Figure 7.9: *Simulation of convolution between 16 weighted PSFs and object slices. Convolution result is normalized.*

7.7 Quantification of 2D image formed

Before quantifying the artificial objects, a test grid was built similar to the one used in a previous study [2]. It consists of differently sized transparent triacontakaidigons (32-sided polygons) on a dark background, each specified by the diameter of the biggest circle fitting inside the triacontakaidigon as shown in Fig. C.1. The test grid optical images are 8-bit with size corresponding to 43×32 μm^2 area. The median intensity v' inside triacontakaidigon (see Apendix C) one was $v' = 170$ and the median background value u' was $u' = 10$, giving a 50% threshold level of $\theta' = 1/2(u' + v') = 90$. These values are summarized in Tab. C.1 in the appendices. Triacontakaidigon two was too small to be measured. For circles diameter > 1 μm, measured values differ from specified values in the order of 1%.In order to quantify the bubbles dimension first the 2D image formed is segmented using gray level window slicing using threshold value T=0.5. Second the segmentation results a binary, black and white image of the bubble with a ring. Next applying morphological image processing the all the region inside the bubble becomes white for white ring with black background (see Fig. 7.11b) and black for the black ring white background (see Fig. 7.13b). However, it is complemented to get white region inside the bubble and black background. Finally the number of white region pixels and their area is computed to get the total area of the bubble.

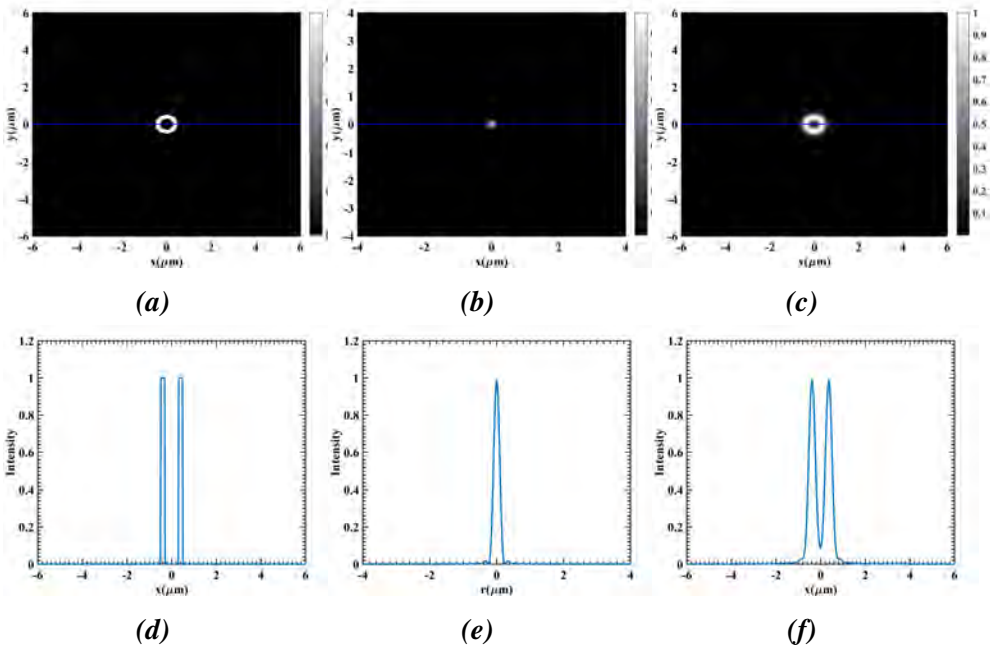

Figure 7.10: *Effects of PSF on slices during convolution. (a) White ring object slice at the focus, (b) 2D PSF at the focus, and (c) Convolved slice. (d, e and f) are intensity cross-sections for (a, b and c) respectively.*

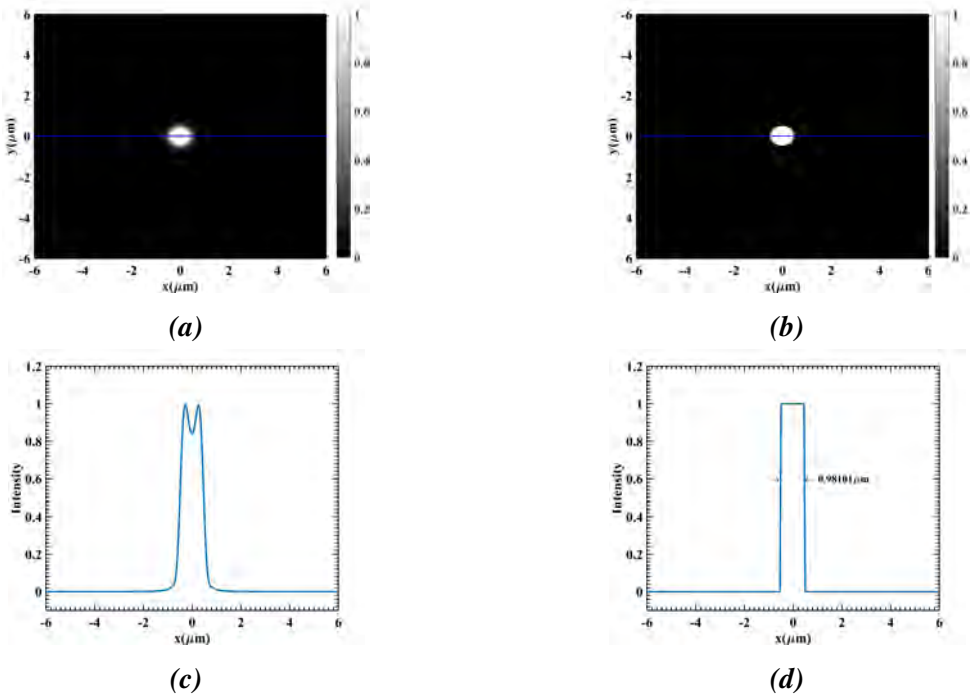

Figure 7.11: *Segmentation of 16 stacked white ring object slices. (a) Stacked weighed object slices, (b) Segmented object and (c, d) are intensity cross-sections of (a, b) respectively.*

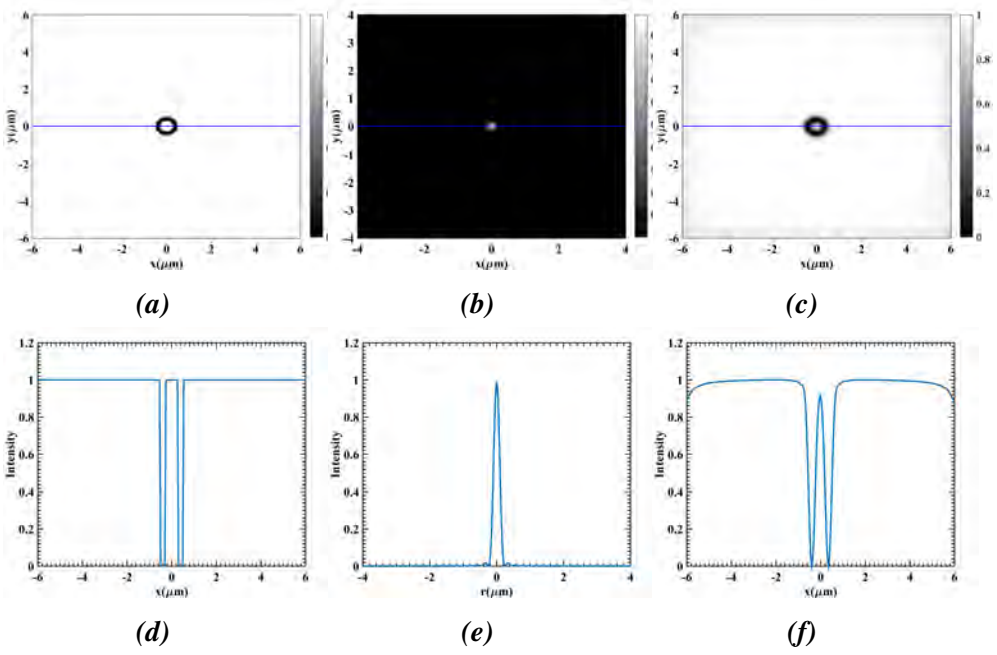

Figure 7.12: *Effects of PSF on slices during convolution. (a) Black ring object slice at the focus, (b) 2D PSF at the focus, and (c) Convolved slice. (d, e and f) are intensity cross-sections for (a, b and c) respectively.*

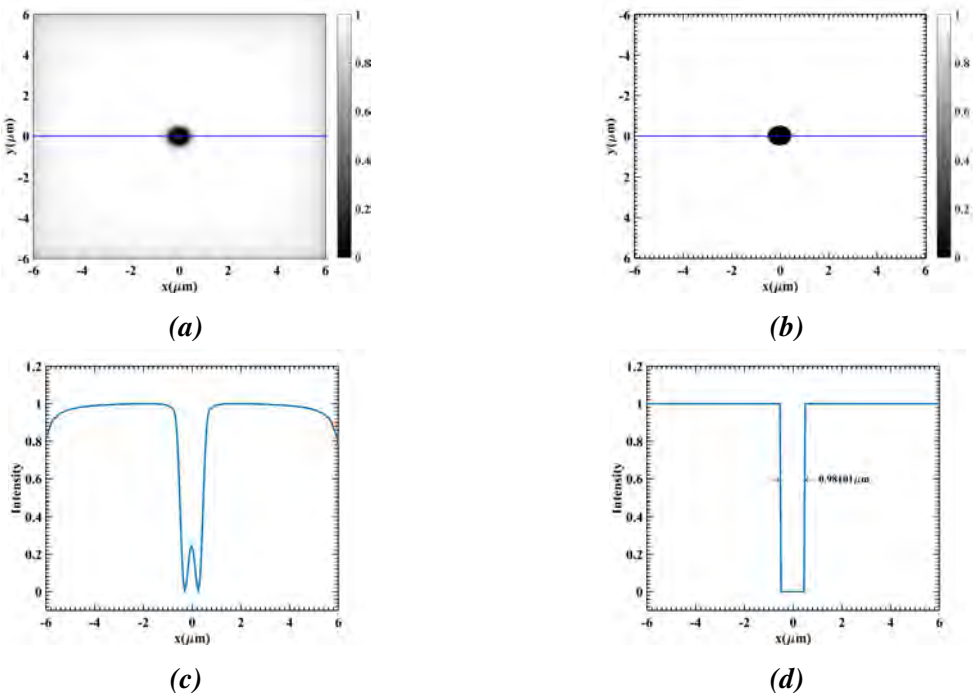

Figure 7.13: *Segmentation of 16 stacked black ring object slices. (a) Stacked weighed object slices, (b) Segmented object and (c, d) are intensity cross-sections of (a, b) respectively.*

Finally, repeating quantification for all artificial objects a comparison was made between true object size and measured object size is made for the two kinds of objects as shown in Fig. 7.14. A systematic error is observed for objects in focus with radius $\leq 1.65\ \mu$m. Moreover, for objects in focus with radius $> 1.65\ \mu$m, measurements showed that even if the objects are in focus, there is discrepancy of 0.66% for white ring object and 0.64% for black ring objects, between the true object size and measured size. In addition, a comparison was made between true object size and measured object size for objects shifted by 25%, 50%, 75% and 90% (see Fig. 7.6 and Fig. 7.7), above the focus (Fig. 7.14) and below the focus (see Appendix D). The comparison was done for objects of size $0.9\mu\text{m} \leq r \leq 5\mu\text{m}$, to avoid negative values, when mean absolute percentage error is calculated. Moreover, size measurement of objects with white ring slightly differ from objects with black ring as presented in Tab. 7.1. The reason is that convolving a white ring object is different from black ring objects. When white ring object with black background is convolved with PSF the contribution of the white ring for the convolution result is higher than black ring. As a result for white ring objects the size measures are slightly higher than black ring objects. Moreover, the results showed that for the same shift above the focus and below the focus, the size measured values of an object differ by 3.6%.

7.7.1 True versus measured object size above focus

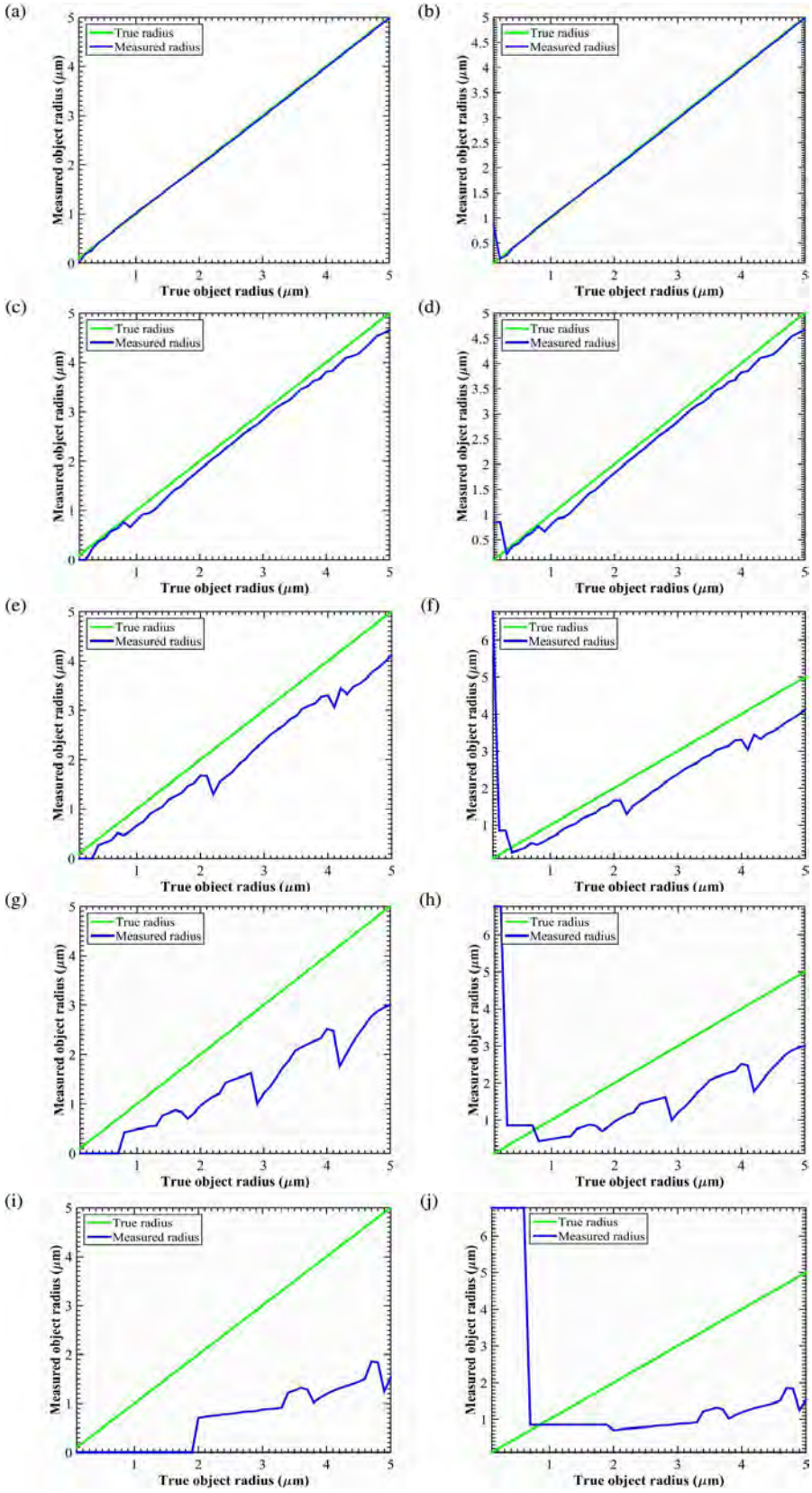

Figure 7.14: *Measured object diameter versus true object diameter at different shift values above focus. White ring object (Left column) and Black ring object (Right column). Shift of focus is 25%, 50%, 75% and 90%, from top to bottom respectively. (see Appendix D for shift values below focus).*

7.7.2 Percentage error measured above the focus

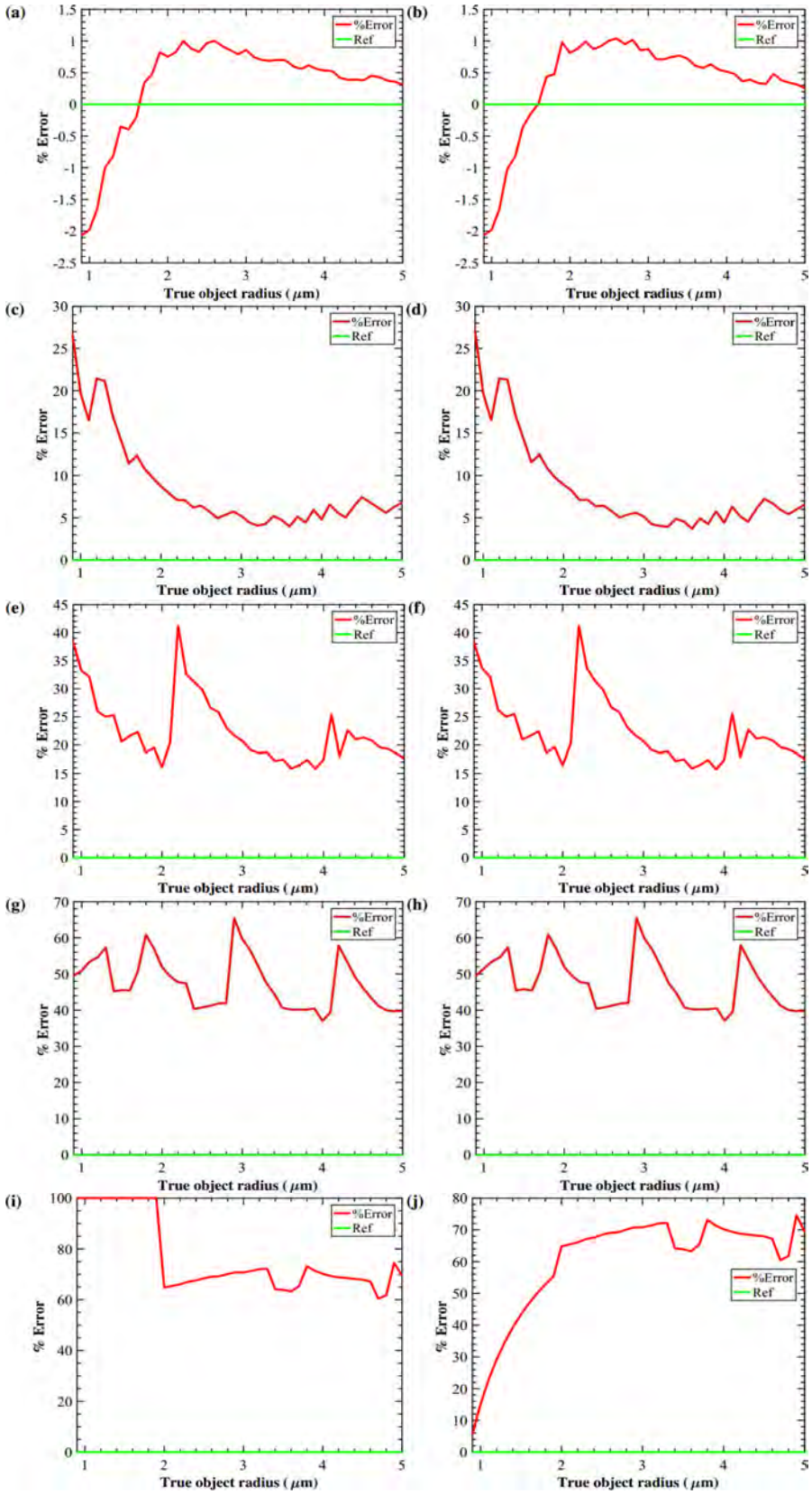

Figure 7.15: *Object size measured percentage error at different shift values above focus. White ring objects (Left column) and black ring objects (Right column). Shift of focus is 25%, 50%, 75% and 90%, from top to bottom respectively. (see Appendix D for shift values below focus).*

Table 7.1: *Comparison of black vs white ring object mean percentage error. For objects measured above and below focus.*

Shift of focus (%)	**Mean percentage error for white ring object of (r >= 0.9 μm)**		**Mean percentage error for black ring of object (r >= 0.9 μm)**	
	Above focus	**Below focus**	**Above focus**	**Below focus**
25%	8.59380	5.96420	8.52160	5.86710
50%	22.6226	19.0577	22.7076	19.1277
75%	47.344	42.5200	47.4123	42.5779
90%	76.4813	64.6456	59.7057	64.6868

The results on Tab. 7.1 summarizes the effect of defocussing in quantifying a microscope image of a microbubble. It is shown that effect of defocussing becomes elaborated for shift of focus above 25%. In addition the mean percentage error above focus and below focus is different. The reason is that the weighting function is not exactly symmetric, the weighting values below the focus is slightly greater than the the weighting values above the focus. Moreover, the percentage error for white ring and black ring objects is different. The reason could be the effect of convolution, convolving a white ring object with black background and convolving a black ring object with white background is not the same. Specifically the blurring effect of the PSF differs for both cases. As a result, the segmentation will result different values of size measures for the same shift of focus.

CHAPTER 8

Conclusion and Recommendation

8.1 Conclusion

This thesis introduced a novel technique to model a three-dimensional (3D) optical imaging system and quantification of the resulting simulated optical images. It is presented that even though a 3D object is in focus, its two-dimensional (2D) optical image size defers from the actual size. Artificial objects with different sizes were measured with an error less than 1% for an object with diameter greater than 1.65 μm, which is caused by the low resolution of the modeled object and the segmentation process. For smaller objects, the size measurement discrepancy between the actual and measured gets more pronounced. In addition, size measurements for smaller objects of actual radius < 0.9 μm of white rings with black background slightly differ from size measurements of black rings of same actual radius with white background. Furthermore, the effect of defocusing on object size measurement is also confirmed by the various tests carried out in this thesis study.

8.2 Recommendation for future work

The research that has been undertaken in this thesis has highlighted a number of topics on which further research would be beneficial. Several areas where information is lacking were highlighted in the different chapters. Whilst some of these were addressed by the research in this thesis, others remain. For example, the 3D objects used to model the microbubbles are ideal artificial objects having spherical geometry. Also, the parameters used to model the 3D optical imaging system are ideal cases that assume no optical aberrations. Future studies might, for example, investigate on 3D objects (contrast agent microbubbles, red blood cell) by recording real microscopic images at different depth of focus, and apply a more advanced segmentation technique to measure the 3D object sizes. Moreover, further research can be made in predicting actual object size of 3D objects from images recorded by a microscope at any focus.

References

[1] A. Stanziola, M. Toulemonde, Y. O. Yildiz, R. J. Eckersley, and M.-X. Tang, "Ultrasound imaging with microbubbles [life sciences]," *IEEE Signal Processing Magazine*, vol. 33, no. 2, pp. 111–117, 2016.

[2] M. Postema, A. Bouakaz, C. T. Chin, and N. de Jong, "Simulations and measurements of optical images of insonified ultrasound contrast microbubbles," *IEEE transactions on ultrasonics, ferroelectrics, and frequency control*, vol. 50, no. 5, pp. 523–536, 2003.

[3] T. L. Szabo, *Diagnostic ultrasound imaging: inside out*. Academic Press, 2004.

[4] S. H. Bloch, M. Wan, P. A. Dayton, and K. W. Ferrara, "Optical observation of lipid-and polymer-shelled ultrasound microbubble contrast agents," *Applied physics letters*, vol. 84, no. 4, pp. 631–633, 2004.

[5] N. De Jong, M. Emmer, A. Van Wamel, and M. Versluis, "Ultrasonic characterization of ultrasound contrast agents," *Medical & biological engineering & computing*, vol. 47, no. 8, pp. 861–873, 2009.

[6] J. Sijl, H. J. Vos, T. Rozendal, N. de Jong, D. Lohse, and M. Versluis, "Combined optical and acoustical detection of single microbubble dynamics," *The Journal of the Acoustical Society of America*, vol. 130, no. 5, pp. 3271–3281, 2011.

[7] J. Sijl, E. Gaud, P. J. Frinking, M. Arditi, N. de Jong, D. Lohse, and M. Versluis, "Acoustic characterization of single ultrasound contrast agent microbubbles," *The Journal of the Acoustical Society of America*, vol. 124, no. 6, pp. 4091–4097, 2008.

[8] J.-M. Gorce, M. Arditi, and M. Schneider, "Influence of bubble size distribution on the echogenicity of ultrasound contrast agents: a study of sonovue^{TM}," *Investigative radiology*, vol. 35, no. 11, pp. 661–671, 2000.

[9] K. Sarkar, W. T. Shi, D. Chatterjee, and F. Forsberg, "Characterization of ultrasound contrast microbubbles using in vitro experiments and viscous and viscoelastic interface models for encapsulation," *The Journal of the Acoustical Society of America*, vol. 118, no. 1, pp. 539–550, 2005.

[10] M. J. Blomley, J. C. Cooke, E. C. Unger, M. J. Monaghan, and D. O. Cosgrove, "Microbubble contrast agents: a new era in ultrasound," *British Medical Journal*, vol. 322, no. 7296, p. 1222, 2001.

[11] V. Sboros, S. D. Pye, C. A. MacDonald, J. Gomatam, C. M. Moran, and W. N. McDicken, "Absolute measurement of ultrasonic backscatter from single microbubbles," *Ultrasound in medicine & biology*, vol. 31, no. 8, pp. 1063–1072, 2005.

[12] V. Sboros, S. Pye, T. Anderson, C. Moran, and W. McDicken, "Acoustic rayleigh scattering at individual micron-sized bubbles," *Applied physics letters*, vol. 90, no. 12, p. 123902, 2007.

[13] A. L. Klibanov, P. T. Rasche, M. S. Hughes, J. K. Wojdyla, K. P. Galen, J. H. Wible Jr, and G. H. Brandenburger, "Detection of individual microbubbles of ultrasound contrast agents: imaging of free-floating and targeted bubbles," *Investigative radiology*, vol. 39, no. 3, pp. 187–195, 2004.

[14] S. M. van der Meer, B. Dollet, M. M. Voormolen, C. T. Chin, A. Bouakaz, N. de Jong, M. Versluis, and D. Lohse, "Microbubble spectroscopy of ultrasound contrast agents," *The Journal of the Acoustical Society of America*, vol. 121, no. 1, pp. 648–656, 2007.

[15] N. de Jong, P. J. Frinking, A. Bouakaz, M. Goorden, T. Schourmans, X. Jingping, and F. Mastik, "Optical imaging of contrast agent microbubbles in an ultrasound field with a 100-mhz camera," *Ultrasound in medicine & biology*, vol. 26, no. 3, pp. 487–492, 2000.

[16] Y. Sun, D. E. Kruse, P. A. Dayton, and K. W. Ferrara, "High-frequency dynamics of ultrasound contrast agents," *IEEE transactions on ultrasonics, ferroelectrics, and frequency control*, vol. 52, no. 11, pp. 1981–1991, 2005.

[17] P. A. Dayton, J. S. Allen, and K. W. Ferrara, "The magnitude of radiation force on ultrasound contrast agents," *The Journal of the Acoustical Society of America*, vol. 112, no. 5, pp. 2183–2192, 2002.

[18] C. T. Chin, C. Lancée, J. Borsboom, F. Mastik, M. E. Frijlink, N. de Jong, M. Versluis, and D. Lohse, "Brandaris 128: A digital 25 million frames per second camera with 128 highly sensitive frames," *Review of scientific instruments*, vol. 74, no. 12, pp. 5026–5034, 2003.

[19] J. E. Chomas, P. Dayton, J. Allen, K. Morgan, and K. W. Ferrara, "Mechanisms of contrast agent destruction," *IEEE transactions on ultrasonics, ferroelectrics, and frequency control*, vol. 48, no. 1, pp. 232–248, 2001.

[20] H. Netten, L. J. Van Vliet, F. R. Boddeke, P. De Jong, and I. T. Young, "A fast scanner for fluorescence microscopy using a 2-d ccd and time delayed integration," *BioImaging, vol. 2 (4)*, 1994.

[21] P. Suetens, *Fundamentals of medical imaging*. Cambridge university press, 2009.

[22] P. N. Wells, "Ultrasound imaging," *Physics in medicine and biology*, vol. 51, no. 13, p. R83, 2006.

[23] I. Minin and O. Minin, *Ultrasound Imaging and Medical Applications*. InTech, 2011.

[24] K. Shung, *Diagnostic Ultrasound: Imaging and Blood Flow Measurements, Second Edition*. CRC Press, 2015.

[25] J. T. Bushberg and J. M. Boone, *The essential physics of medical imaging*. Lippincott Williams & Wilkins, 2011.

[26] J. Viti, "High framerate imaging of ultrasound contrast agents," Ph.D. dissertation, Erasmus University Rotterdam, 2016.

[27] S. M. van der Meer, "Ultrasound contrast agents : resonances of coated bubbles," Ph.D. dissertation, Universiteit Twente, 2007.

[28] G. Kossoff, "Basic physics and imaging characteristics of ultrasound," *World journal of surgery*, vol. 24, no. 2, pp. 134–142, 2000.

[29] M. Postema, *Fundamentals of medical ultrasonics*. CRC Press, 2011.

[30] C. J. Pavlin and F. Foster, "Basic physics of high-frequency ultrasound imaging," pp. 3–16, 1995.

[31] J. E. Aldrich, "Basic physics of ultrasound imaging," *Critical care medicine*, vol. 35, no. 5, pp. S131–S137, 2007.

[32] B. B. Goldberg, J.-B. Liu, and F. Forsberg, "Ultrasound contrast agents: a review," *Ultrasound in medicine & biology*, vol. 20, no. 4, pp. 319–333, 1994.

[33] D. A. Hutchins, H. Mair, P. Puhach, and A. Osei, "Continuous-wave pressure fields of ultrasonic transducers," *The Journal of the Acoustical Society of America*, vol. 80, no. 1, pp. 1–12, 1986.

[34] C. K. Yeh, "Ultrasound microbubble contrast agents for diagnostic and therapeutic applications: current status and future design," *Chang Gung Med J*, vol. 35, no. 2, 2012.

[35] H. Becher and P. N. Burns, *Handbook of contrast echocardiography: Left ventricular function and myocardial perfusion*. Springer Science & Business Media, 2012.

[36] P. Burns, P. Hilpert, and B. Goldberg, "Intravenous contrast agent for ultrasound doppler: In vivo measurement of small tumor vessel dose-response," pp. 322–324, 1990.

[37] A. B. N. de Jong and F. ten Cate, "Ultrasound contrast imaging. principles and applications," *Klinische Fysica*, vol. 3, p. 24–31, 2000.

[38] J. M. Correas, L. Bridal, A. Lesavre, A. Méjean, M. Claudon, and O. Hélénon, "Ultrasound contrast agents: properties, principles of action, tolerance, and artifacts," *European radiology*, vol. 11, no. 8, pp. 1316–1328, 2001.

[39] S. Sirsi and M. Borden, "Microbubble compositions, properties and biomedical applications," *Bubble Science, Engineering & Technology*, vol. 1, no. 1-2, pp. 3–17, 2009.

[40] R. Lencioni *et al.*, *Enhancing the role of ultrasound with contrast agents*. Springer, 2006.

[41] M. E. BURKARD *et al.*, "Behavior of bubbles of slowly permeating gas used for ultrasonic imaging contrast." *Investigative radiology*, vol. 30, no. 5, pp. 315–321, 1995.

[42] A. W. Appis, M. J. Tracy, and S. B. Feinstein, "Update on the safety and efficacy of commercial ultrasound contrast agents in cardiac applications," *Echo research and practice*, vol. 2, no. 2, pp. R55–R62, 2015.

[43] E. Stride and N. Saffari, "Microbubble ultrasound contrast agents: a review," *Proceedings of the Institution of Mechanical Engineers, Part H: Journal of Engineering in Medicine*, vol. 217, no. 6, pp. 429–447, 2003.

[44] E. Quaia, *Contrast media in ultrasonography*. Springer, 2005.

[45] F. S. Foster, P. N. Burns, D. H. Simpson, S. R. Wilson, D. A. Christopher, and D. E. Goertz, "Ultrasound for the visualization and quantification of tumor microcirculation," *Cancer and Metastasis reviews*, vol. 19, no. 1-2, pp. 131–138, 2000.

[46] F. Stuart Foster, P. N. Burns, D. H. Simpson, S. R. Wilson, D. A. Christopher, and D. E. Goertz, "Ultrasound for the visualization and quantification of tumor microcirculation," *Cancer and Metastasis reviews*, vol. 19, no. 1, pp. 131–138, 2000.

[47] P. S. Epstein and M. S. Plesset, "On the stability of gas bubbles in liquid-gas solutions," *The Journal of Chemical Physics*, vol. 18, no. 11, pp. 1505–1509, 1950.

[48] A. Kabalnov, D. Klein, T. Pelura, E. Schutt, and J. Weers, "Dissolution of multicomponent microbubbles in the bloodstream: 1. theory," *Ultrasound in medicine & biology*, vol. 24, no. 5, pp. 739–749, 1998.

[49] T. Faez, M. Emmer, K. Kooiman, M. Versluis, A. F. van der Steen, and N. de Jong, "20 years of ultrasound contrast agent modeling," *IEEE transactions on ultrasonics, ferroelectrics, and frequency control*, vol. 60, no. 1, 2013.

[50] P. Marmottant, S. van der Meer, M. Emmer, M. Versluis, N. de Jong, S. Hilgenfeldt, and D. Lohse, "A model for large amplitude oscillations of coated bubbles accounting for buckling and rupture," *The Journal of the Acoustical Society of America*, vol. 118, no. 6, pp. 3499–3505, 2005.

[51] N. De Jong, M. Emmer, C. T. Chin, A. Bouakaz, F. Mastik, D. Lohse, and M. Versluis, ""compression-only" behavior of phospholipid-coated contrast bubbles," *Ultrasound in medicine & biology*, vol. 33, no. 4, pp. 653–656, 2007.

[52] S. Zhao, K. W. Ferrara, and P. A. Dayton, "Asymmetric oscillation of adherent targeted ultrasound contrast agents," *Applied physics letters*, vol. 87, no. 13, p. 134103, 2005.

[53] H. Vos, B. Dollet, J. Bosch, M. Versluis, and N. De Jong, "Nonspherical vibrations of microbubbles in contact with a wall—a pilot study at low mechanical index," *Ultrasound in medicine & biology*, vol. 34, no. 4, pp. 685–688, 2008.

[54] P. A. Dayton, K. E. Morgan, A. L. Klibanov, G. H. Brandenburger, and K. W. Ferrara, "Optical and acoustical observations of the effects of ultrasound on contrast agents," *IEEE transactions on ultrasonics, ferroelectrics, and frequency control*, vol. 46, no. 1, pp. 220–232, 1999.

[55] W. J. Croft, *Under the microscope: a brief history of microscopy*. World Scientific, 2006, vol. 5.

[56] Q. Wu, F. Merchant, and K. Castleman, *Microscope image processing*. Academic press, 2010.

[57] D. B. Murphy, *Fundamentals of light microscopy and electronic imaging*. John Wiley & Sons, 2002.

[58] C. A. DiMarzio, *Optics for engineers*. Crc Press, 2011.

[59] D. A. Boas, C. Pitris, and N. Ramanujam, *Handbook of biomedical optics*. CRC press, 2011.

[60] D. A. Agard, "Optical sectioning microscopy: cellular architecture in three dimensions," *Annual review of biophysics and bioengineering*, vol. 13, no. 1, pp. 191–219, 1984.

[61] D. Karadaglić and T. Wilson, "Image formation in structured illumination wide-field fluorescence microscopy," *Micron*, vol. 39, no. 7, pp. 808–818, 2008.

[62] R. W. Cole, T. Jinadasa, and C. M. Brown, "Measuring and interpreting point spread functions to determine confocal microscope resolution and ensure quality control," *Nature protocols*, vol. 6, no. 12, pp. 1929–1941, 2011.

[63] I. Young, R. Zagers, L. Van Vliet, J. Mullikin, F. Boddeke, and H. Netten, "Depth-of-focus in microscopy," in *8th Scandinavian Conference on Image Analysis, Tromso, Norway*, 1993.

[64] M. Sonka, V. Hlavac, and R. Boyle, *Image processing, analysis, and machine vision*. Cengage Learning, 2014.

[65] F. Träger, *Springer handbook of lasers and optics*. Springer Science & Business Media, 2012.

[66] P. N. Prasad, *Introduction to biophotonics*. John Wiley & Sons, 2004.

[67] B. Saleh, *Introduction to subsurface imaging*. Cambridge University Press, 2011.

[68] E. Hecht, "Optics, 4th," *International edition, Addison-Wesley, San Francisco*, vol. 3, 2002.

[69] M. Born and E. Wolf, *Principles of optics: electromagnetic theory of propagation, interference and diffraction of light*. CUP Archive, 2000.

[70] O. K. Ersoy, *Diffraction, fourier optics and imaging*. John Wiley & Sons, 2006, vol. 30.

[71] J. W. Goodman, *Introduction to Fourier Optics*. McGRAW-HILL, 1996.

[72] I. N. Bronstein, J. Hromkovic, B. Luderer, H.-R. Schwarz, J. Blath, A. Schied, S. Dempe, G. Wanka, S. Gottwald, E. Zeidler *et al.*, *Taschenbuch der mathematik*. Springer-Verlag, 2012, vol. 1.

[73] H. Purtle, *History of the Microscope*, 1974.

[74] I. T. Young, "Quantitative microscopy," *IEEE engineering in medicine and biology magazine*, vol. 15, no. 1, pp. 59–66, 1996.

[75] G. Sluder and D. E. Wolf, *Digital microscopy*. Academic Press, 2013, vol. 114.

[76] J. Toriwaki and H. Yoshida, *Fundamentals of three-dimensional digital image processing*. Springer Science & Business Media, 2009.

[77] J. Rittscher, R. Machiraju, and S. T. Wong, *Microscopic image analysis for life science applications*. Artech House, 2008.

[78] C. Solomon and T. Breckon, *Fundamentals of Digital Image Processing: A practical approach with examples in Matlab*. John Wiley & Sons, 2011.

[79] R. C. Gonzalez, R. E. Woods *et al.*, "Digital image processing," 2002.

[80] B. Jähne, "Digital image processing," *The Netherlands: Springer-Verlag*, 2005.

[81] A. Koschan and M. Abidi, *Digital color image processing*. John Wiley & Sons, 2008.

[82] C. Fernandez-Maloigne, *Advanced Color Image Processing and Analysis*. Springer Science & Business Media, 2012.

[83] R. M. Rangayyan, B. Acha, and C. Serrano, *Color image processing with biomedical applications*. SPIE Press Bellingham, 2011.

[84] J. Canny, "A computational approach to edge detection," *IEEE Transactions on pattern analysis and machine intelligence*, no. 6, pp. 679–698, 1986.

[85] F. Lehmann, "Turbo segmentation of textured images," *IEEE transactions on pattern analysis and machine intelligence*, vol. 33, no. 1, pp. 16–29, 2011.

[86] H. Gómez-Moreno, S. Maldonado-Bascón, and F. López-Ferreras, "Edge detection in noisy images using the support vector machines," in *International Work-Conference on Artificial Neural Networks*. Springer, 2001, pp. 685–692.

[87] H. G. Kaganami and Z. Beiji, "Region-based segmentation versus edge detection," in *Intelligent Information Hiding and Multimedia Signal Processing, 2009. IIH-MSP'09. Fifth International Conference on*. IEEE, 2009, pp. 1217–1221.

[88] Y. B. Chen and O. T. Chen, "Image segmentation method using thresholds automatically determined from picture contents," *EURASIP Journal on Image and Video Processing*, vol. 2009, no. 1, p. 1, 2009.

[89] S. Hojjatoleslami and J. Kittler, "Region growing: a new approach," *IEEE Transactions on Image processing*, vol. 7, no. 7, pp. 1079–1084, 1998.

[90] W. Y. Ma and B. Manjunath, "Edge flow: a framework of boundary detection and image segmentation," in *Computer Vision and Pattern Recognition, 1997. Proceedings., 1997 IEEE Computer Society Conference on*. IEEE, 1997, pp. 744–749.

[91] T. Y. Young, *Handbook of pattern recognition and image processing (vol. 2): computer vision*. Academic Press, Inc., 1994.

[92] A. K. Jain, *Fundamentals of digital image processing*. Prentice-Hall, Inc., 1989.

[93] J. B. Sibarita, "Deconvolution microscopy," *Microscopy Techniques*, pp. 1288–1291, 2005.

[94] D. Zill, W. S. Wright, and M. R. Cullen, *Advanced engineering mathematics*. Jones & Bartlett Learning, 2011.

APPENDIX A

Slices of Objects with Radius $(3, 4, 5\ \mu\mathrm{m})$

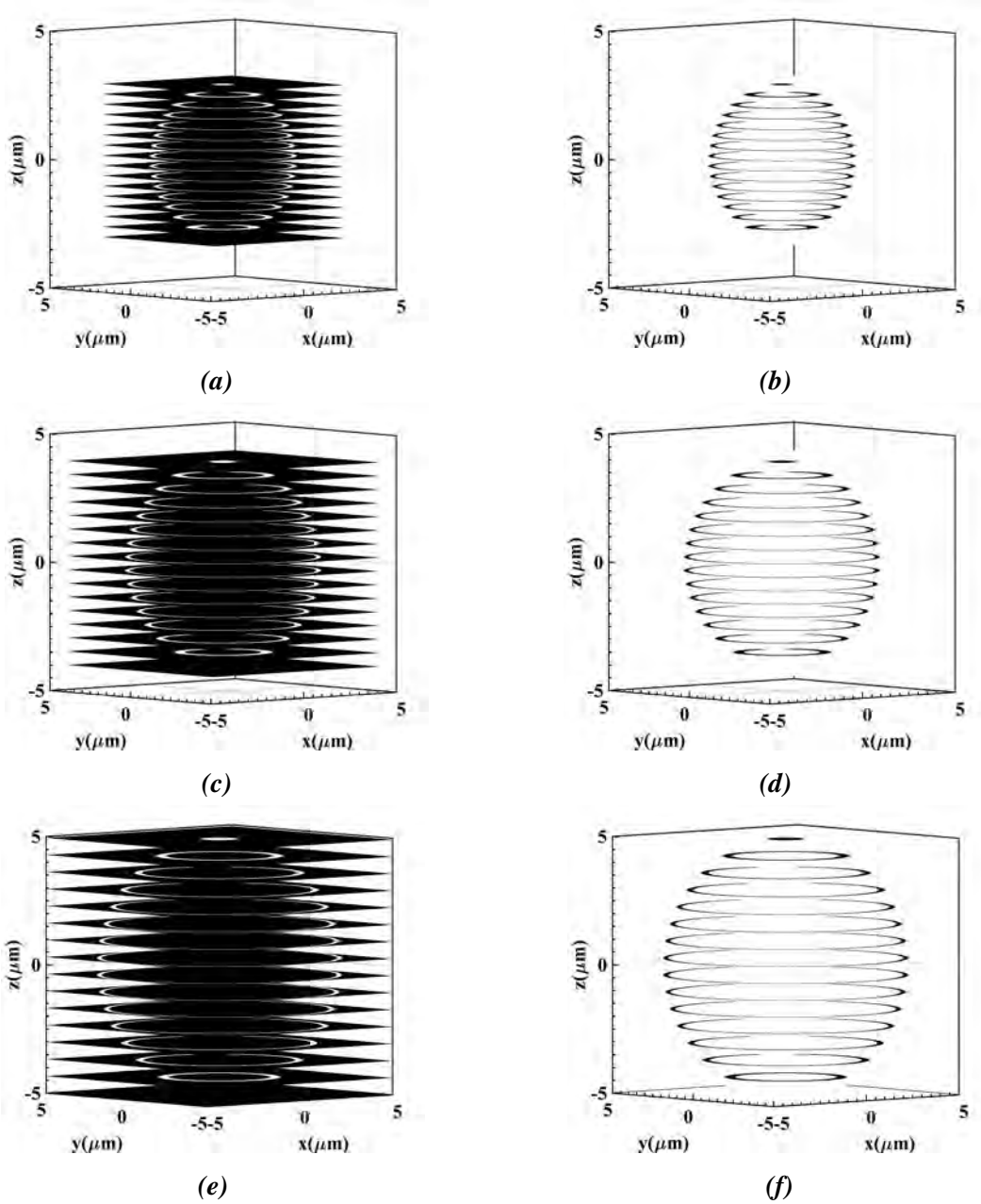

Figure A.1: *Slices of white ring objects (left column) and black ring objects (right column) with radius: (a, b)* $3\mu m,\ 3 * \Delta z$*, (c, d)* $4\mu m,\ 4 * \Delta z$*, and (e, f)* $5\mu m,\ 5 * \Delta z$*. Note: multiple of* Δz *is used for each object to visualize 16 slices without overlapping. However, for the actual size measurement* $\Delta z = 133nm$*.*

APPENDIX B

Bessel Functions

Bessel functions arise in solving differential equations for systems with cylindrical symmetry [94]. The Bessel functions $J_n(z)$ is linearly independent solutions to the differential equation

$$z^2\frac{d^2y}{dz^2}+z\frac{dy}{dz}+(z^2-n^2)y=0 \tag{B.1}$$

The Bessel function $J_n(z)$ is defined by the power series:

$$J_n(z)=\sum_{m=0}^{\infty}\frac{(-1)^m z^{n+2m}}{2^{n+2m}m!(n+m)!}\ ,\ n\geq 0. \tag{B.2}$$

$J_n(z)$ is called the Bessel function of the first kind. It coverages for all z. Hence, $J_n(z)$ is defined for all z. Fig. B.1 shows the first five real Bessel functions $J_0(z),...,J_4(z)$.

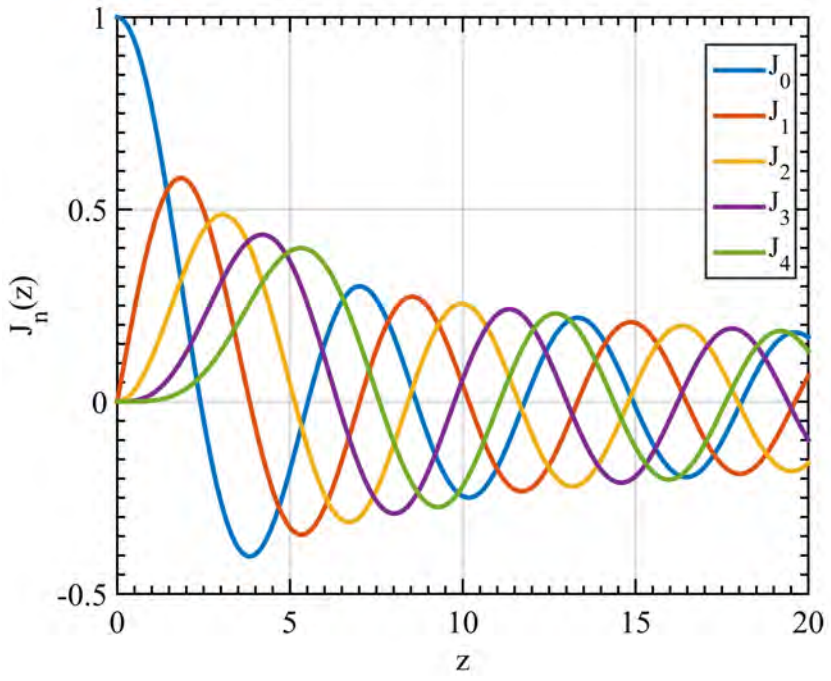

Figure B.1: *Real Bessel functions of the first kind.*

APPENDIX C

Test Grid for 2D Objects Measurement

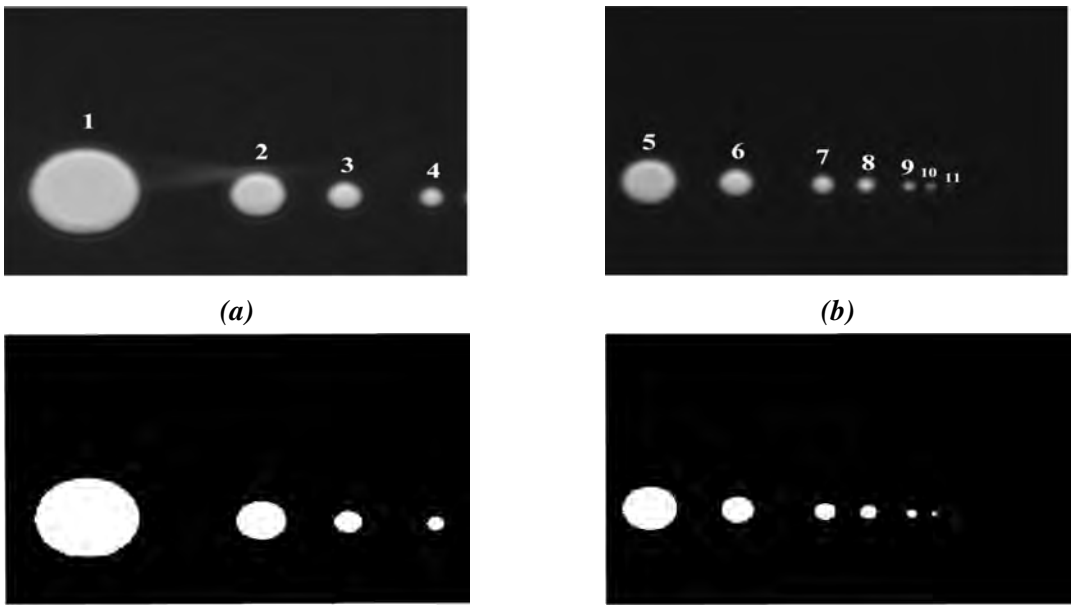

Figure C.1: *CCD images of 11 triacontakaidigons on a calibration grid (a, b) segmented with a $\theta = 1/2(u' + v')$ threshold, where u' is median intensity and v' is median background value (c, d) [2]].*

Table C.1: *Specified and measured diameters of Triacontakaidigons.*

Triacontakaidigon	**Specified diameter** (μm)	**Measured diameter** (μm)
1	10.0 ± 0.1	10.02
2	5.0 ± 0.1	5.03
3	3.0 ± 0.1	2.97
4	2.0 ± 0.1	1.96
5	5.0 ± 0.1	5.07
6	3.0 ± 0.1	3.02
7	2.0 ± 0.1	1.96
8	1.6 ± 0.1	1.55
9	1.0 ± 0.1	0.93
10	0.8 ± 0.1	0.58
11	0.4 ± 0.1	-

APPENDIX D

Objects Size Measured Below the Focus

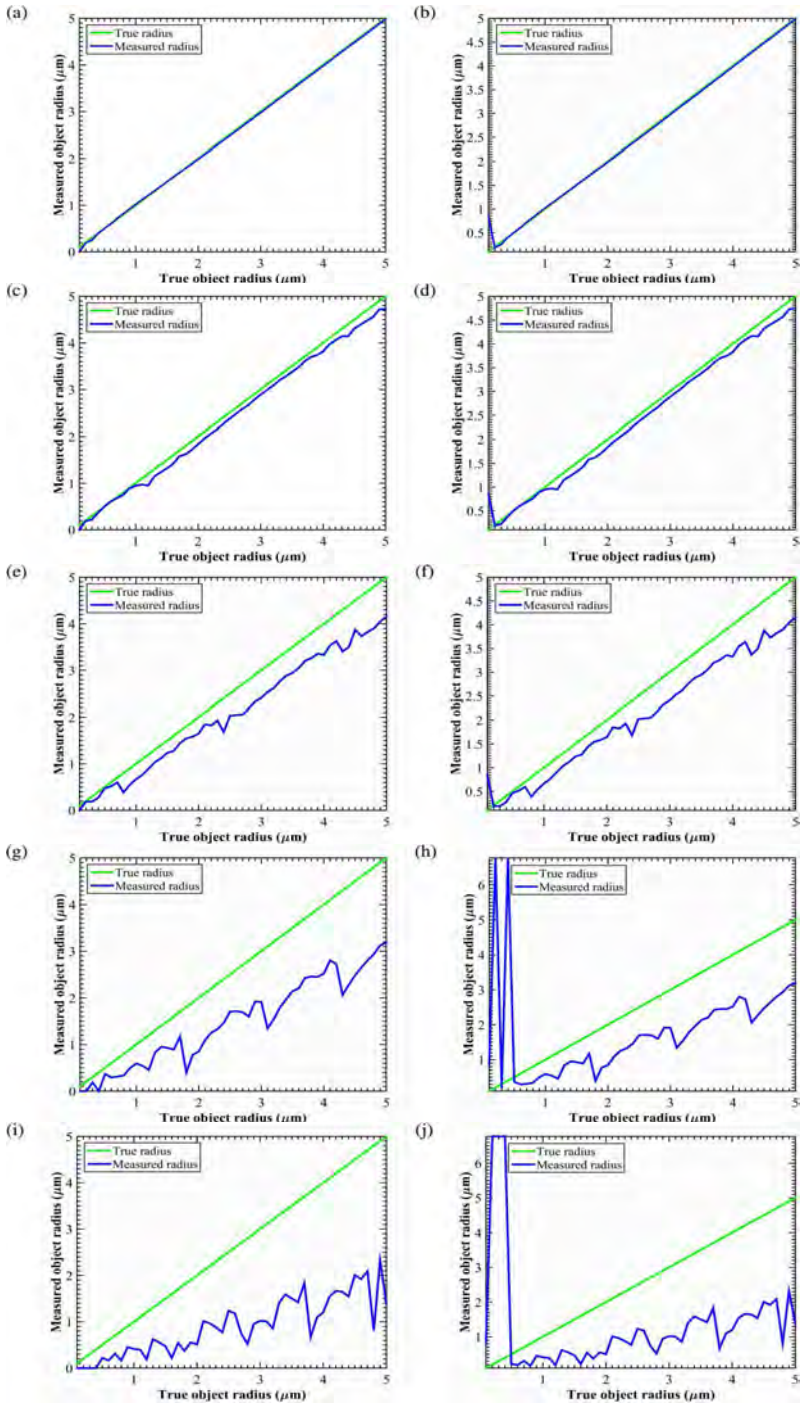

Figure D.1: *Measured objects diameter versus true objects diameter at different shift values below focus. White ring object (Left column) and Black ring object (Right column). Shift of focus is 25%, 50%, 75% and 90%, from top to bottom respectively.*

APPENDIX E

Measured percentage error below focus

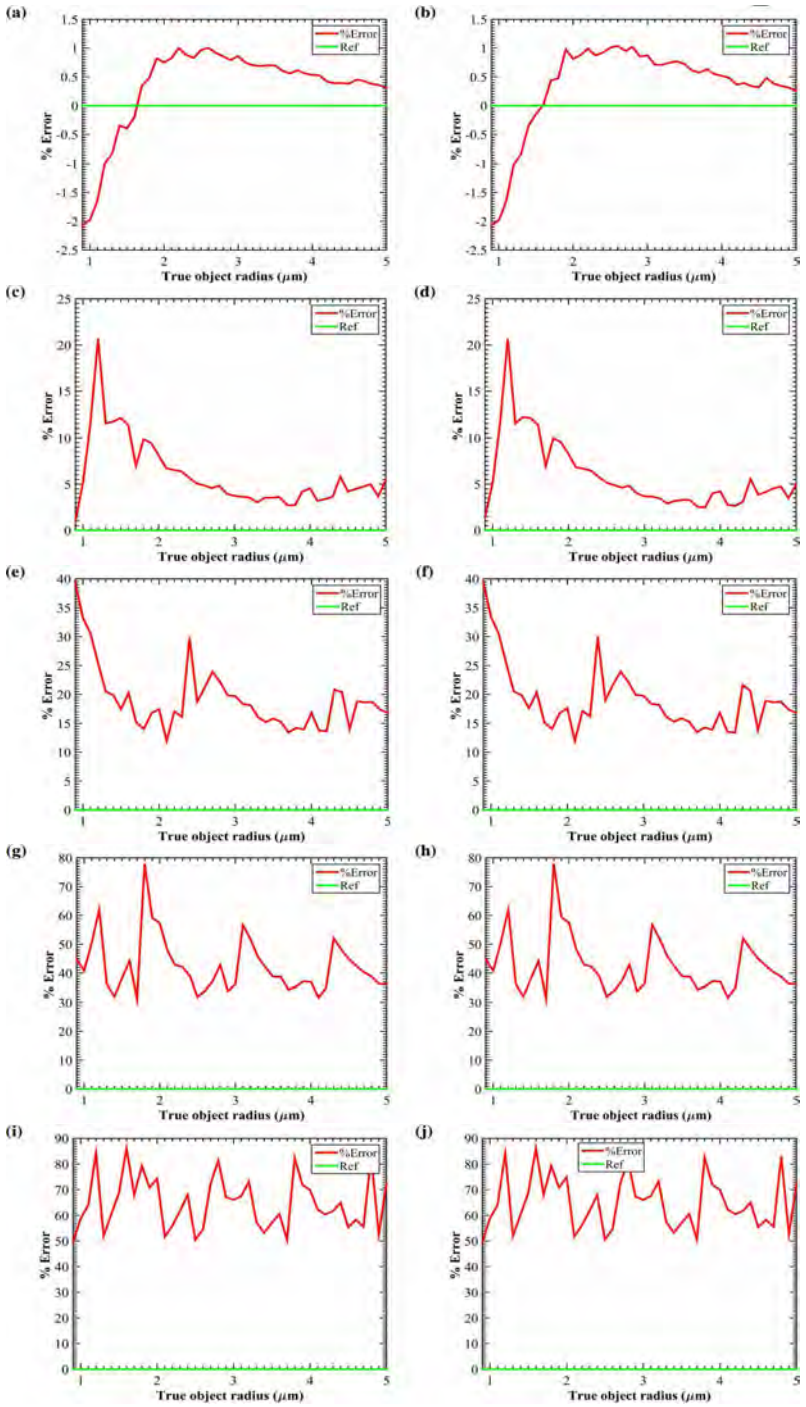

Figure E.1: *Object size measured percentage error at different shift values below focus. White ring object (Left column) and Black ring object (Right column). Shift of focus is 25%, 50%, 75% and 90%, from top to bottom respectively.*

Index